Cathodic Electrodeposition of Thin Ceramic Oxide Films

By

Hao Wang

A Thesis Submitted in Fulfillment of the Requirements for the Degree of Doctor of Philosophy of the University of London and the Diploma of Imperial College London

Imperial College London

April 2008

Acknowledgements

I would like to take this opportunity to thank all the people who have assisted me in many ways to the completion of this thesis. Without their support, this work today might still be unfinished.

First and foremost, I would like to thank my supervisors, Dr. Mary Ryan and Dr. Stephen Skinner for their guidance and assistance during the course of my studies at Imperial College. The completion of my PhD study is not possible without them, who have been extremely supportive and tremendously helpful throughout this period. Truly appreciate the encouragement and support which they have given me.

There are many people I would like to thank from Imperial College, University of Southampton and the SSRL who have assisted in experimental work, particularly Dr. Mahmoud Ardakani, Mr. Richard Chater, Mr. Richard Sweeney, Dr. Andrea Russell, Dr Will Branford and Dr. Bridget Ingham. I would also like to thank the members of Dr. Mary Ryan's and Dr. Stephen Skinner's research group for their experimental help.

I would like to acknowledge the award of an ORS scholarship (HW) and department founding that enabled this work to be fulfilled.

Finally, I am deeply indebted to my Mum, Dad and my husband, who have done everything wonderfully, and selflessly to support and encourage me throughout these years. Thank you very much for being in my life.

Abstract

Cathodic electrodeposition (CELD) is achieved via hydrolysis of metal ions by electrogenerated base to form metal oxide/hydroxide films on a cathodic substrate. Hydroxides and peroxides can then be converted to oxides by thermal treatment. In this study, TiO_2 thin films (both rutile and anatase phases) and cobalt-doped anatase films were successfully produced through this method. These materials have presented applications in electronic and magnetic devices, such as piezo-ceramics as well as in catalysis. The CELD technology and the characterization of these thin films are described in detail in this thesis.

The various parameters (deposition time, current density and annealing temperature *etc.*) that affect the characteristics of TiO_2 films deposited on Pt and Ti substrates have been explored. Focus ion beam imaging (FIB) and scanning electron microscopy (SEM) analysis show that the thickness of the film increases as the deposition time increases. Applying current density greater than 30 $mA \cdot cm^{-2}$ results in the film having a porous structure, however, little difference between films was observed when the current density was 20 $mA \cdot cm^{-2}$ or less. XRD data gave an indication that the as-deposited films were amorphous; after annealing at elevated temperatures (400°C ~ 1000°C) anatase and rutile phases were formed successfully.

Samples were thermally treated under three different atmospheres: air, argon and argon/hydrogen (10% hydrogen). Different characteristics were observed after annealing. SEM and atomic force microscopy (AFM) show that the particle size increased after annealing in argon and argon/hydrogen. Preferred orientation of the films annealed in different atmospheres was observed and further investigated using high temperature in-situ XRD.

$Ti_{1-x}Co_xO_{2-\delta}$ films were successfully prepared on Ti and Si substrates. When the annealing temperature was above 600 °C a $CoTiO_3$ phase was detected in the film, whilst maintaining the anneal temperature below 600 °C resulted in only anatase peaks ((101) and (200)) being observed. The films annealed at 400 °C show room-temperature ferromagnetism as determined by vibrating sample magnetometry, and the magnetization per unit volume was of the right order of magnitude (0.2-0.6μ_B/Co) for dilute ferromagnetic oxide thin films. X-ray absorption spectroscopy studies showed that the cobalt was present as Co^{2+} and the XRD data were consistent with cobalt substituted anatase lattice as the lattice parameter increased from 9.0080(2) to 9.4780 (3).

Content

Acknowledgements 2

Abstract 3

List of Figures 7

List of Tables 13

Chapter 1 Introduction 14

1.1 Ceramic Oxide Films 14

1.2 Fabrication 15

1.3 Aim of This Work 16

1.4 Thesis Organization 17

Chapter 2.0 Literature Review 19

2.1 Electroceramics 19

2.1.1 Ferro-, Piezo- and Pyro- Electric Materials 20

2.1.2 Ferromagnetic Materials 24

2.2 Preparation of Ceramic Oxide Films 30

2.2.1 Sputter Deposition 30

2.2.2 Sol-gel Deposition 33

2.2.3 Electrodeposition 35

Chapter 3.0 Experimental Procedure 44

3.1 Preparation of TiO_2 films 44

3.1.1 Cathodic Electrodeposition of TiO_2 Films 44

3.1.2 Solution Preparation 46

3.1.3 Substrate Preparation 47

3.1.4 Thermal treatment 48

3.2 Preparation of Co doped TiO_2 films 48

3.2.1 Solution Preparation 48

3.2.2 Sample Preparation 49

3.2.3 Cathodic Electrodeposition of Co-TiO_2 Films 49

3.2.4 Thermal Treatment 49

3.3 Analysis of the Deposited Films 50

3.3.1 X-ray Diffraction (XRD) & High Temperature X-ray Diffraction (HTXRD) 50

3.3.2 Scanning Electron Microscopy (SEM) & Field Emission Gun Scanning Electron Microscopy (FEGSEM) 54

3.3.3 Atomic Force Microscopy (AFM) 57

3.3.4 Focused Ion Beam (FIB) 59

3.3.6 X-Ray Absorption Spectroscopy (XAS) 63

Chapter 4.0 Results & Discussion -- TiO_2 Films 64

4.1 As-deposited TiO_2 films 64

4.1.1 Effect of Variation of Voltage and Time on Film Quality 64

4.2 Characterisation of Electrodeposits 68

4.2.1 Thermal Treatment 68

4.2.2 Film Surface Morphology & Grain size 75

4.2.3 Film Thickness 85

4.3 Influence of Electrodeposition Parameters on Film Quality 88

4.3.1 Current Density 88

4.3.2 Effect of Deposition Time 92

4.3.3 Variation of the Annealing Temperature 94

4.4 Effect of Annealing Atmosphere on Film Morphology 98

4.4.1 Impact on Film Surface Morphology 98

4.4.2 Effect on Film Orientation & Grain Size 107

4.4.3 Ti Control Test 114

Chapter 5.0 Results & Discussion -- Co doped TiO_2 Films 123

5.1 As-deposited cobalt doped TiO_2 films 123

5.1.1 Effect of Variation of Voltage and Time on Film Quality 123

5.2 Characterization of Electrodeposited Films 125

5.2.1 Thermal Treatment 125

5.2.2 Film Surface Morphology & Grain size 131

5.2.3 Film Thickness 139

5.3 Film Magnetic Properties *142*

5.4 Effect of Atmosphere on Annealing *144*

5.4 Summary *149*

Chapter 6 Conclusions & Future Work 151

6.1 Conclusions *151*

6.2 Future Work *153*

7.0 Appendix 155

7.1 Master Table for Sample Preparation Conditions *155*

7.2 Published Paper *158*

8.0 Reference 161

List of Figures

Figure 1 - Typical unit cell of ferroelectric materials; 'P' polarization, 'E' external field 20

Figure 2 - Three crystal structures of TiO_2; rutile, anatase, and brookite respectively 22

Figure 3 Schematic diagrams of ferromagnetism (a), and ferrimagnetism (b) 24

Figure 4 - Schematic illustrations of three types of semiconductors, A: a magnetic semiconductor, B: a diluted magnetic semiconductor and C: a nonmagnetic semiconductor. Blue circles are magnetic ions 25

Figure 5 - Magnetization (M) measured as a function of magnetic field strength (H) for a $Ti_{0.93}Co_{0.07}O_{2-\alpha}$ film deposited on $SrTiO_3$ (001) at room temperature (300K). 26

Figure 6 - Schematic graph of sputter deposition, after 32

Figure 7 - Flow diagram for preparation of sol-gel coatings, after 35

Figure 8 - Schematic representation of the experimental set up of the 3-electrode cell used in the electrolytic deposition of ceramic films. Counter electrode: Pt wire; working electrode: Pt or Ti foil; reference electrode: MSE. 45

Figure 9 - A schematic diagram for determining Bragg's law 51

Figure 10 - Schematic diagram of a Scanning Electron Microscope 55

Figure 11 - Schematic diagram showing the operation of an Atomic Force Microscope 58

Figure 12 - Schematic diagram of a typical FIB microscope, after 61

Figure 13 - Schematic illustration of the procedure used to generate ramp sections using FIB milling: D: the length from observation, x: real thickness of the film. 62

Figure 14 - Variation of electrode potential with deposition time for a TiO_2 film deposited on a Pt substrate. Deposition temperature is 0-2°C, H_2O_2 concentration of 0.01M, supplied current is 20 $mA \cdot cm^{-2}$. 65

Figure 15 - Cell voltage with deposition time for TiO_2 films deposited on Pt by Zhitomirsky et al, deposition temperature is 0-2°C, supplied current is 20 $mA \cdot cm^{-2}$, H_2O_2 concentration of 0.01M 65
Figure 16 XRD pattern of TiO_2 film deposited on Pt substrate before and after annealing. A: anatase phase; R: rutile phase; Pt: substrate and * is attributed to the peaks which formed because of the tungsten radiation. Black line indicates the as-deposited film; red line indicates annealed film. 69
Figure 17 - In-situ XRD patterns of a TiO_2 film deposited on a Pt substrate. Heating was from 100-1000 °C in 100 °C steps (■-anatase, O-rutile, Δ-platinum) 71
Figure 18 - XRD pattern of a TiO_2 film deposited on a Ti substrate before and after annealing. As-deposited film was annealed at 800°C for one hour. Both scan were did at room temperature. A: anatase phase; R: rutile phase; Ti: substrate. Black line indicates the as-deposited film; red line indicates annealed film 72
Figure 19 - In-situ XRD pattern of a TiO_2 film deposited on a Ti substrate 74
Figure 20 - SEM image of the as-deposited TiO_2 film on a Pt substrate before annealing. 75
Figure 21 - AFM images of film topography of TiO_2 films deposited on Pt substrate, (A) before thermal treatment A, (B) after heating at 800 °C for one hour, showing spherical morphology attributed to anatase and (C) after heating at 800 °C for one hour showing well-crystallized terrace-like morphology attributed to rutile phase 77
Figure 22 - SEM image of the as-deposited TiO_2 film on a Ti substrate before annealing. 78
Figure 23 - FEGSEM images of a TiO_2 film deposited on a Ti substrate after annealing at 800 °C in air for one hour. (a): spherical morphology, (b): terrace-like morphology. (c): mixed morphology 81
Figure 24 - FEGSEM images of cracks in the TiO_2 film deposited on a Ti substrate after annealing at 800 °C in air for one hour. 82
Figure 25 - EDS image of TiO_2 film deposited on Ti substrate after annealing. 84
Figure 26 - AFM image of a TiO_2 film deposited on a Ti substrate after annealing at 800 °C for one hour in air 84

Figure 27 - FIB image of a annealed TiO_2 film deposited on a Ti substrate. A 38° ramp has been created allowing the substrate, interface and film to be observed. 87
Figure 28 - SEM images of TiO_2/Ti films electrodeposited under different currents before heat treatment. (a): 30 $mA \cdot cm^{-2}$, (b): 20 $mA \cdot cm^{-2}$, (c): 10 $mA \cdot cm^{-2}$, (d): 5 $mA \cdot cm^{-2}$ respectively. 90
Figure 29 - XRD patterns of TiO_2/Ti samples deposited at different currents, after heat treatment at 800 °C for one hour. 91
Figure 30 - SEM images of TiO_2/Pt films deposited for (a) 15 mins, (b) 30 minutes, and (c) 45 minutes before heat treatment. The current density was 20 $mA \cdot cm^{-2}$ for all samples. 93
Figure 31 - XRD pattern of a TiO_2 film deposited on a Ti substrate annealed at 1000 °C and held for one hour. "R" indicates the rutile phase 95
Figure 32 - A schematic diagram for the determination of the X-ray penetration depth of the sample. 96
Figure 33 Constitutional diagram of titanium – oxygen system 97
Figure 34 - SEM images of TiO_2/Ti films annealed in different atmospheres at 800 °C for one hour. (a), (b): annealed in air; (c), (d): annealed in Ar; and (e), (f): annealed in mixed Ar/H_2 (10% H_2). 99
Figure 35 - AFM images of film topography of TiO_2 film deposited on Ti substrate, annealed at 800 °C for one hour in (a), Air, (b), Ar and (c), Ar/H_2 100
Figure 36 - FEGSEM images of the FIB ramps of TiO_2/Ti films annealed in different atmospheres. a) Film annealed in air; b) film annealed in Ar and c) film annealed in Ar/H_2. Four points on each film were analysed by EDS 104
Figure 37 - FEGSEM images of the porous microstructure of TiO_2/Ti films annealed in different atmospheres. (a) and (b), annealed in Air, (c) and (d), annealed in Ar, (e) and (f), annealed in Ar/H_2, ... 105
Figure 38 - (a) Comparison of XRD patterns of the three as-deposited samples, and (b), XRD patterns of TiO_2 films annealed in different atmospheres. Films were deposited at current density 20 $mA \cdot cm^{-2}$ for 45 minutes and then sintered at 800 °C for one hour. The thicknesses of the films are shown in Table 6. 108

Figure 39 - Intensity ratios of rutile (110) and rutile (101) annealed in air, Ar, and Ar/H_2. 110
Figure 40 - Pole figures of (a) TiO_2/Ti film annealed in air at 800 °C for one hour; (b) TiO_2/Ti film annealed in Ar/H_2 at 800 °C for one hour. 111
Figure 41 - SEM images of a Ti substrate annealed in different atmospheres at 800 °C for one hour. (a, b): annealed in air; (c, d): annealed in Ar; and (e, f): annealed in mixed Ar/H_2 (10% H_2). 115
Figure 42 - FEGSEM images comparing the surface topography between TiO_2/Ti film Ti substrate annealed in different atmospheres at 800 °C for one hour. (a) and (b), film and Ti substrate annealed in air, (c) and (d), film and Ti substrate annealed in Ar, and (e) and (f), film and Ti substrate annealed in Ar/H_2, respectively. 117
Figure 43 - FEGSEM images of the FIB ramps of Ti substrate oxidized films annealed in different atmospheres. (a) Ti substrate annealed in Air; (b) Ti substrate annealed in Ar and (c) Ti substrate annealed in Ar/H_2. Four points on each film were the EDS tested area. 118
Figure 44 - XRD comparison patterns of the oxidized films of Ti substrate annealed in different atmospheres 121
Figure 45 - Variation of electrode potential with deposition time for a cobalt doped TiO_2 film deposited on a Ti substrate; Co^{2+} concentration of 0.05%. Deposition temperature was 0-2 °C, supplied current was 20 $mA \cdot cm^{-2}$ 124
Figure 46 - The In-situ XRD pattern of Co-TiO_2 deposited on Ti substrate (cobalt content 10%). Sample was heated from room temperature to 600 °C and then cooled down to room temperature. Δ-anatase, o-rutile, □-$CoTiO_3$, •-Ti substrate, ж-Pt... 126
Figure 47 - In-situ XRD pattern of Co doped anatase deposited on titanium substrate annealed in Ar from 0 °C to 800 °C. Molar ratio of Ti: Co in the solution is 20:1, deposited at current density 20 $mA \cdot cm^{-2}$ for 45 minutes 128
Figure 48 - XRD comparison of Co-TiO_2 deposited on Ti substrate with current density 20 $mA \cdot cm^{-2}$ before and after annealing in air (black line: before heat treatment;

red line: after heat treatment) the annealed sample was held at 400 °C for 90 minutes 129
Figure 49 - XRD comparison pattern for doped (x = 0.05) and un-doped anatase film thermally treated at 400°C for 90 minutes. Black line: anatase film deposited on Ti substrate; red line: cobalt doped anatase film deposited on Ti Substrate. 130
Figure 50 - SEM image of the as-deposited Co doped film on Ti substrate before thermal treatment after air drying at room temperature 132
Figure 51 - SEM image of Co doped film on Si substrate before thermal treatment 133
Figure 52 - FEGSEM image of Co doped TiO_2 film after annealing at 400 °C in air 134
Figure 53 - FEGSEM image of Co-doped TiO_2 film deposition on Ti substrate after annealing at 400 °C in air (magnified image) 135
Figure 54 - AFM image of Co-doped TiO_2 film deposition on Ti substrate after annealing at 400 °C in air 135
Figure 55 - Normalized XANES spectra of cobalt doped anatase films, (a), energy range between 7500-8100 eV, (b), energy range between 7700-7780 eV, and (c), energy range between 7660-7800 eV 138
Figure 56 - FIB image of Co doped TiO_2 deposited on Ti substrate. Image was taken at 35°. 139
Figure 57 - FEGSEM image of Co doped TiO_2 deposited on Si substrate, cross section. 140
Figure 58 - FEGSEM images of Co-TiO_2 film deposited on Ti (a) film surface topography at low magnification; (b) the ramp made by FIB, the ramp is taken at 30 degree from surface; (c) the magnification of the ramp, white area: film, dark area: Ti substrate; (d) very high magnification, white area: film, dark area: Ti substrate. ... 141
Figure 59 - Room temperature in-plane magnetization vs. magnetic field for three $Co_{0.05}Ti_{0.95}O_2$ samples (denoted A, B and C) produced under nominally identical experimental conditions. The differences of the three samples are most likely attributed to film volume estimate since the XANES/XRD data are identical 143

Figure 60 - XRD comparison pattern of cobalt doped anatase annealed in different atmospheres. Red line is film annealed in air; blue line is film annealed in Air and green line is film annealed in mixed argon hydrogen (10% hydrogen). '■' indicates (101) anatase phase; '●' indicates (200) anatase phase, and '★' indicates Ti substrate. 145

Figure 61 - AFM images of cobalt doped anatase films deposited on Ti substrate.(a) film annealed in air; (b) film annealed in Ar; (c) film annealed in Ar/H_2 (10% hydrogen). 146

Figure 62 - FEGSEM images of cobalt doped anatase deposited on Ti substrate annealed in a) Air; b) Ar and c) Ar/H_2 (10% hydrogen). Samples are all annealed at 400 °C held for 90 minutes. 148

List of Tables

Table 1 - Particle sizes and XRD parameters of deposited TiO_2 film. 85

Table 2 – Parameters of samples deposited under different current densities 89

Table 3 - Atomic percentages of Ti and O at four points of each film (shown in Figure 35) tested by EDS. Films were deposited at current 20 $mA \cdot cm^{-2}$ for 45 minutes and annealed at 800 °C for one hour. 102

Table 4 - Plane spacing of Ti metal and rutile. 112

Table 5 - Calculated particle sizes for TiO_2 films annealed in different atmospheres 113

Table 6 - Thicknesses comparison of Ti oxidized film and deposited film 119

Table 7 - Lattice parameter for doped and un-doped anatase films 137

Table 8 - Ionic radii for Co^{2+}, Co^{3+} and Ti^{4+} 137

Table 9 - The scale of the particle size for cobalt doped anatase and TiO_2 films annealed in different atmospheres 144

Chapter 1 Introduction

1.1 Ceramic Oxide Films

Ceramic oxide films such as TiO_2, and $Pb(Zr,Ti)O_3$ (PZT) and are of considerable interest for electrochemical and electronic areas because of their interesting properties. They can be used, for example, as bimorphs in microphones, earphones, loudspeakers, and stereo pick-ups, as fuel solenoid ignition systems and cigarette lighters, sonar generators and ultrasonic cleaners, *etc*. For doped materials they can be used in magnetic devices.

TiO_2 is one of the most important ceramic oxide materials; as a raw material it supports industries worth billions of dollars annually in the USA. The common and important phases for TiO_2 are rutile and anatase which both have a tetragonal structure. Rutile is the most thermodynamically stable phase; anatase is less dense and less stable when compared with rutile. Anatase will transform to rutile when thermally treated above 800°C [1].

TiO_2 has many valuable properties. Due to its high refractive index and good insulating properties it can be used as protective layers for very large scale integrated (VLSI) circuits and stainless steels [2]. The high dielectric constant makes TiO_2 useful as the dielectric gate of metal-oxide-semiconductor field effect transistors (MOSFET) devices [3]. It can also be used to make dimensionally stable electrodes to react as a photo catalyst for degradation of pollutants and super hydrophilic materials [4].

Considering that TiO_2 belongs to the n-type semiconductor and the bandgap is wide, TiO_2 can theoretically be used as a matrix in diluted magnetic semiconductors (DMS)

to increase the Curie temperature above room temperature and make the ferromagnetism stable in DMS materials [5].

Recently, Matsumoto *et al.*[6], reported that cobalt-doped anatase thin films, produced by laser ablation in high vacuum, displayed room-temperature ferromagnetism (RTF). According to these authors, when the concentration of cobalt in the film is between 0 and 8 at %, the film shows ferromagnetic long-range ordering. The magnetic moment of saturated cobalt was reported to be 0.32 μ_B, and the film exhibited a positive magnetoresistance (MR) up to 60 % at 2 K in an 8 T field. The reason that Co-doped anatase films have RTF characteristics, however, is still unclear. Some researchers [7, 8] have suggested that the observed FM behaviour is caused by cobalt cations substituted into the anatase lattice which is similar to the local structure environment of Co in $CoTiO_3$. Others [9, 10] believed that clusters of Co metal in these films generated the observed RTF properties. More recently, a new theory suggesting that oxygen vacancies play an important role in room temperature ferromagnetic behaviour was reported by Liu *et al.* [11].

1.2 Fabrication

Synthesis of ceramic oxide films and diluted magnetic semiconductors (DMS) has been achieved by a variety of methods including the sol-gel method, sputtering, wet chemical, spray pyrolysis [12], and oxygen-plasma-assisted molecular-beam epitaxy (OPA-MBE) *etc.*

A more recently applied method which was used in this study is cathodic electrodeposition. Cathodic electrolytic deposition (CELD) has been defined as a process in which film deposition is achieved via the hydrolysis of a metal salt solution using an electrogenerated base such as OH^- in order to form oxides,

hydroxides or peroxides on a cathodic electrode. Hydroxides and peroxides are then converted to oxides by thermal treatment. This method has previously been used successfully to deposit ceramic oxide films such as TiO_2, ZrO_2 and $ZrTiO_4$ [13] by Zhitomirsky *et al.* Other researchers prepared CeO_2 powders [14], $Mo_xW_{1-x}O_3$ films [15] and $Cu_{2-x}Mn_xO$ films [16] using this method as well. The difference is these researchers deposit ceramic oxide on to the electrode directly; whereas, Zhitomirsky *et al.* deposit peroxocomplex on to the electrode and then use thermal treatment convert them to oxides. This is due to titanium salt immediately reacting with water to form precipitates without formation of TiO_2 [17], therefore peroxocomplex has to be used to resolve the problem. In this research, cobalt doped anatase films have been prepared by an electrochemical technique for the first time. In comparison with other methods the advantages of CELD are that: it is a low temperature synthesis technique, the procedure is simple and relatively inexpensive, the film can be controlled through varying the composition of the bath and finally, the coatings can be deposited on various substrate shapes. Considering the benefits of the CELD method, we report here on the successful growth of pure and cobalt doped anatase films on both titanium and silicon substrates using electrolytic deposition.

This method also has some drawbacks. For example, it is difficult to get crack free films because of the shrinkage during this drying process; the detailed mechanism of the deposition procedure is unknown and only certain types of substrate can be used depending on the conductivity.

1.3 Aim of This Work

The aim of this work was, first, produce TiO_2 film with good quality, which is continuous and crack-free using the cathodic electrolytic deposition method. Once formed, change the deposition parameters such as deposition time, current density

and annealing temperature to investigate the deposition parameters that influence film characteristics.

As it is known that the preparation methods and the post thermal treatment conditions strongly influence TiO_2 film properties, it is necessary to study the relationship between the post thermal treatment conditions and the TiO_2 film properties. In this research the as-deposited TiO_2 films are thermally treated in air, argon and argon/hydrogen (10% hydrogen) respectively to evaluate the influence of oxygen availability during thermal treatment for CELD produced TiO_2 films.

The second aim is to make co-deposited films with good quality by the CELD method, for example, to produce cobalt-doped anatase film, and to investigate its structural and magnetic characteristics.

1.4 Thesis Organization

In Chapter 2 the relevant literature is reviewed: the concept and the applications of electroceramics and diluted magnetic semiconductor are introduced first, especially some of the popular materials such as TiO_2, PZT and newly developed cobalt doped anatase *etc.* Two methods which are commonly used to produce these materials are also discussed in this chapter. The last subsection of this chapter elucidates the CELD method which was used in this study in detail.

Chapter 3 introduces the experimental procedures: deposition procedure, solution preparation, substrate preparation and the thermal treatment of the TiO_2 films are described. Moreover experimental techniques that were used to characterize the ceramic deposits are also discussed here.

The fundamental characteristics of cathodic electrodeposited TiO_2 film are examined in Chapter 4, followed by the study of the relationship between deposition parameters and film characteristics. The influence of thermal treatment on film properties is discussed in the last part.

In Chapter 5, successfully synthesised Co-doped TiO_2 anatase thin films were studied. Several technical instruments are used to investigate film characteristics, especially film RTF characteristics and cobalt oxidation status in the film.

The last chapter contains the summary and a conclusion of the work presented in this thesis, and future work is briefly discussed.

Chapter 2.0 Literature Review

2.1 Electroceramics

Electronic ceramics, more commonly known as electroceramics, are ceramic materials that are specially formulated for specific electrical, magnetic or optical device applications [18]. Three features are common to all ceramics and electroceramics: the first is that they all have ionic-covalent bonding; the second is that their thermal properties change in proportion with temperature change, and the third is that their microstructures comprise inorganic crystal compounds and/or amorphous glass in varying proportions. These properties can be changed for some materials by thermal treatment.

Thermal treatment is given to ceramic products for two reasons; first, to increase the kinetics of ceramic reactions, this means that raw materials which used to constitute ceramics usually decompose at high temperatures and form more stable compounds; and second, the properties related to the density of ceramics can be enhanced by sintering. Before sintering there is a large percentage of porosity and only weak bonding between neighboring particles. However, after thermal treatment porosity is almost eliminated and more stable bonds are developed. Different types of thermal processing produce different ceramic microstructures, and consequently allow the formation of different sorts of electroceramics. On the other hand, thermal treatment can also result in the formation of different phases of ceramics, depending on the chemical composition.

Electroceramics have different applications, including: (1) ceramic conductors; (2) dielectrics and insulators; (3) piezoelectric ceramics; (4) pyroelectric materials; (5) electro-optic ceramics; and (6) magnetic ceramics.

While all these applications play a significant role in modern technology, this thesis will focus mainly on piezo-ceramics and magnetic materials and their newly identified production technologies.

2.1.1 Ferro-, Piezo- and Pyro- Electric Materials

A selected group of ceramic materials can be polarized in order to render them active through some convenient and reliable means, for example, piezoceramics, pyroelectric ceramics and ferroelectric ceramics [19].

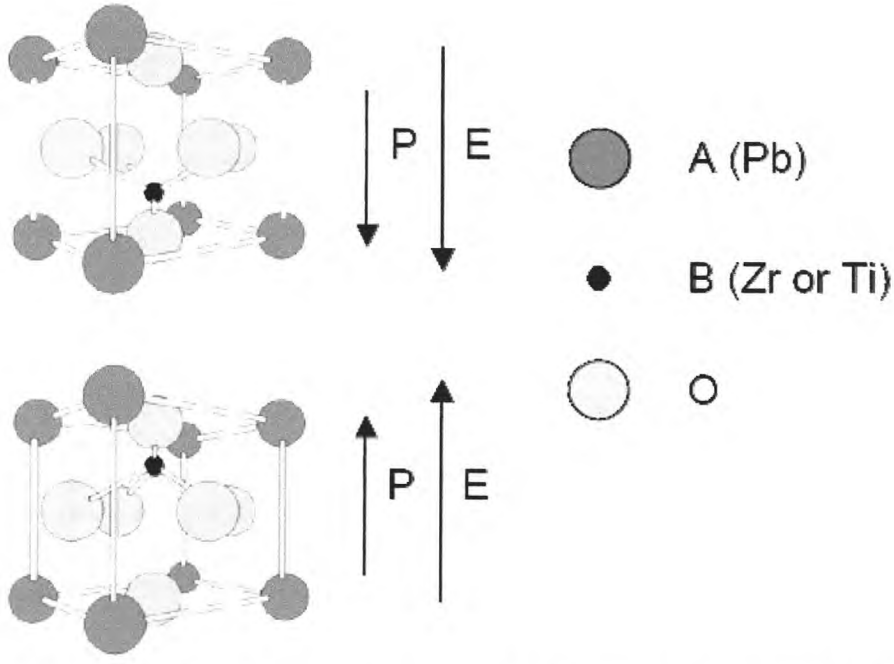


Figure 1 - Typical unit cell of ferroelectric materials; 'P' polarization, 'E' external field [20].

A ferroelectric material is a material that exhibits, below some range of temperature (the Curie temperature), a spontaneous electric polarization in the absence of an electric field [21]. Figure 1 shows the typical ferroelectric material unit cell (ABO_3,

A and B: atom, O oxygen). It can be seen that the direction of the polarization (P) moves when an external field is applied. This is due to the deformation of the BO_6 octahedron in order to accommodate the electrical stress caused by the external field.

Pyroelectric materials characteristically develop an electric polarization if their temperature is changed. It should be mentioned that all ferroelectric materials are pyroelectric. A piezoelectric material is one which develops an electric polarization on applying mechanical stress. Conversely, a mechanical distortion can also be obtained when a piezoelectric material is subjected to an electric field. Pyroelectric materials all have the piezoelectric property, and ferroelectric materials are inherently piezoelectric [22].

Due to their specific characteristics piezoceramics and ferroelectric ceramics have been used for many years as transducers for converting mechanical to electrical energy, and vice versa. This kind of material can be employed in a range of areas, for example, used as bimorphs in microphones, earphones, loudspeakers, and stereo pick-ups; used in fuel solenoid ignition systems and cigarette lighters, sonar generators and ultrasonic cleaners. Transformers, filters and oscillators employ piezoelectric ceramics as well [23]. The most common materials used in these applications are lead zirconium titanate (PZT) ceramics, quartz, *etc* [24, 25].

TiO_2 Films

Traditionally TiO_2 is one of the most common ceramic materials. TiO_2 has three different common crystal phases; these are rutile, anatase, and brookite [26] as shown in Figure 2. Rutile has a tetragonal crystal structure in which the Ti-O octahedra share four edges, for anatase it has a tetragonal crystal structure as well, with the main difference being that the octahedra share four corners instead. Brookite has an orthorhombic structure. At present only anatase, rutile and amorphous films have been observed in TiO_2 thin films. Among them rutile is the most stable phase,

both anatase and rutile are very common for commercial use in powders and in films. Anatase transforms to the rutile phase when thermally treated at temperatures above 800 °C [1, 27, 28]. The transition is however, not reversible.

The total energy of periodic TiO_2 slabs was calculated by Ramamoorthy and Vanderbilt [29] using a self-consistent ab initio method. The result shows that (110) plane of rutile has the lowest surface energy, whereas, the (001) plane of rutile has the highest. Scanning tunneling microscopy (STM) and non-contact atomic force microscopy (AFM) were employed on three low-index rutile surfaces ((110), (001), and (100)) and the results were consistent with the calculations with (110) being the most stable surface [2]. For the anatase phase, the surface which was calculated to have the lowest surface energy was (101) [2].

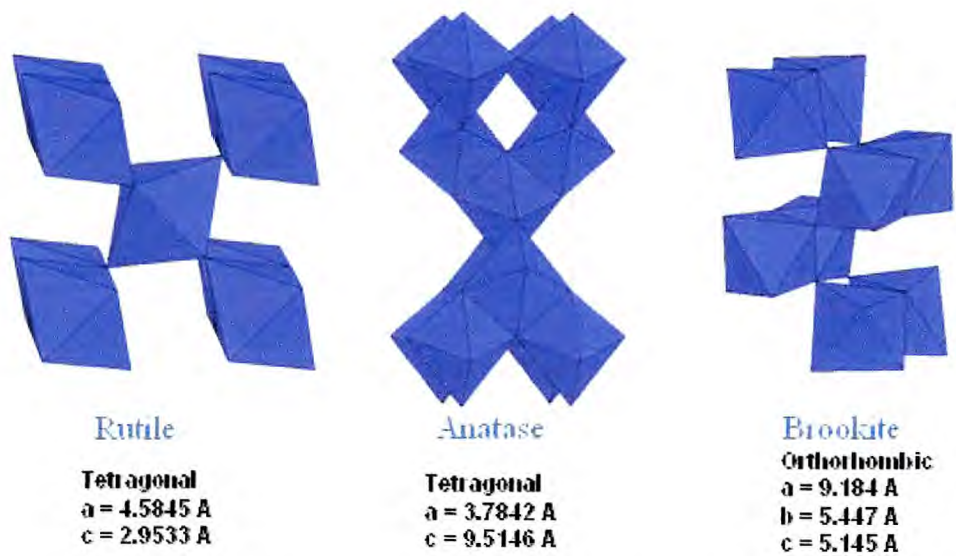


Figure 2 - Three crystal structures of TiO_2; rutile, anatase, and brookite respectively [30].

In recent years, titanium dioxide powders or thin films have attracted attention due to their wide applications in so many areas. Fujishima and Honda [31] reported in 1972 water photolysis on illuminated TiO_2 electrodes and since then, the photoelectric and photochemical properties of TiO_2 have been exploited through use as a photocatalyst. Recently it has been used for photo-assisted organic molecules degradation [32, 33].

Titania tends to lose oxygen and become sub-stoichiometric even when the reducing atmosphere is mild; therefore, the conductivity of the semiconducting metal oxides may change as the oxygen content changes in the atmosphere. TiO_2 can moreover be used as an oxygen gas sensor, for example, employed in car engines to control the mixture of the air/fuel [34, 35]. Tons of TiO_2 pigments are produced world-wide every year [36], for use in almost all sorts of paint because of its high refractive index [2]. It can also be used in cosmetic products and food additives [37, 38]. The high dielectric constant makes TiO_2 suitable to be used as the dielectric gate of metal-oxide-semiconductor field effect transistors (MOSFET) devices [3], and is considered to replace SiO_2 [39]. Nanocrystalline TiO_2 films are employed in electrochromic devices [40] which can control light reflection in mirrors or light transmission in windows. Pure and doped TiO_2 nanocrystalline films are also important in dye-sensitised solar cells [41, 42] .

Dumitriu, et al. [43] found that TiO_2 films with different structures varied in optical and photo catalytic properties and the films consisting of anatase and rutile phases with an appropriate ratio have the best photo catalytic activity. It should be mentioned that the different proportion of film microstructure (anatase or rutile) would influence the photo-catalytic activity; therefore, in order to obtain films with the desired phase composition optimizing the process of preparation is essential. It should be noted that the key factors that influence the microstructure of the final TiO_2 films are the substrate and anneal temperatures [40]. Meng *et al* [44] and Wang *et al* [45] who deposited TiO_2 films by sputtering reported that when the temperature of the substrate increase from room temperature to 500 °C the orientation of the TiO_2 film changes in the order of preferred orientation, random orientation and preferred orientation. The first preferred orientation is a different orientation to the third one. Moreover, the properties of the films, such as refractive index and optical bandgap change as substrate temperature varies. However, how the nature of the substrate influences the TiO_2 film is still not clear.

2.1.2 Ferromagnetic Materials

Originally, 'ferromagnet' meant materials that exhibit spontaneous magnetization in the absence of an external magnetic field [21]. However, recently when there is more than one magnetic ion per primitive cell the different classes of spontaneous magnetization have been identified. The new definition of 'ferromagnet' is that most of the magnetic ions in it have a positive contribution to the net magnetization (Figure 3, a), in order to distinguish it from 'ferrimagnet' in which some of the magnetic ions have a negative contribution to the net magnetization (Figure 3, b). Therefore, ferro- and ferrimagnets have very different magnetic ordering. Permanent magnets are either ferromagnetic or ferrimagnetic. It should be remembered that, as with ferroelectric materials, for both ferromagnets and ferrimagnets when temperature is above a certain temperature (the Curie temperature), the characteristic magnetic properties disappear [46].



a. b.

Figure 3 Schematic diagrams of magnetic ordering on cation sites for (a) ferromagnetic and (b) ferrimagnetic material.

Ferromagnetic materials have been widely used for mass storage of information (hard disks, magnetic tapes, and magnetooptical disks, *etc*) (Figure 4, a) as a result of spin polarization of electron in these materials. Conventional electronics use only the charge of the electron; however, both the spin and charge of the electron may be manipulated independently offering a further degree of freedom to enhance existing microelectronic device performance. [47]. However, as the semiconductors used in circuits and high-frequency devices (normally Si or GaAs) do not contain magnetic ions (as shown in Figure 4 c) it is difficult to make this idea become operable.

Recently, dilute magnetic semiconductors (DMS) - also known as semi-magnetic semi-conductors [48] - have been produced and stimulated considerable interest [48-50]. In general, DMS refers to the nonmagnetic semiconductors, whose lattice is partly substituted by magnetic ions to make them magnetic (Figure 4 b). Considering that the common magnetic ions are Mn, Fe and Co in which the valence is between II-VI, the studies of DMS are mainly concentrated on II-VI semiconductors.

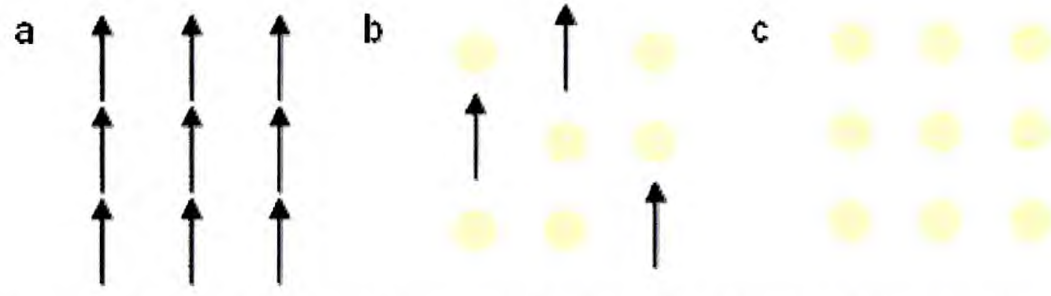


Figure 4 - Schematic illustrations of three types of semiconductors, a: a magnetic semiconductor, b: a dilute magnetic semiconductor and c: a nonmagnetic semiconductor. Blue circles are magnetic ions [49].

In the past decades, Mn doped ZnSe [51], GaAs [52] and InAs [53] DMS have successfully been produced. However, the major drawback for these semiconductors is that they cannot be used as room-temperature ferromagnets in practical applications such as spintronics because they have low Curie temperatures [54, 55]. Later on Dietl *et al* [5] used the Zener model to theoretically predict that the Curie temperature can be increased above room temperature if it is a p-type semiconductor – based DMS (The p-type semiconductor is used instead of semiconductors in which holes are the predominant charge carriers responsible for electrical conduction. In general, the acceptor impurity atoms can induce the excess holes [21]), and if a DMS is based on a wide bandgap semiconductor the ferromagnetism should be stable.

These theoretical calculations precipitated a large amount of research why oxide-based DMS were the milestone of oxide-diluted magnetic semiconductors.

Cobalt doped TiO_2 films

Recently, Matsumoto *et al.*[6], used a combinatorial screening approach to study a huge range of the solid solubility transition metals in TiO_2 found only cobalt doped anatase (the bandgap energy, E_g = 3.2eV) thin films, produced by laser ablation in high vacuum display room-temperature ferromagnetism (RTF) as shown in Figure 5. According to these authors, when the concentration of cobalt in the film is between 0 and 8 at %, the film shows ferromagnetic long-range ordering. The magnetic moment of saturated cobalt was reported to be 0.32 μ_B, and the film exhibited a positive magnetoresistance (giant magnetoresistance (MR) is one of the representative features of DMS materials) up to 60 % at 2 K in an 8 T field.

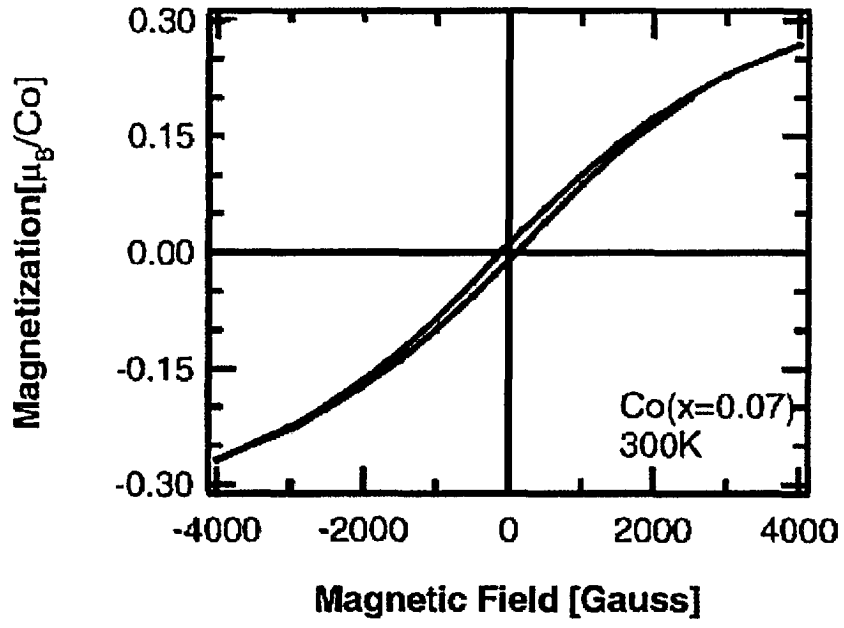


Figure 5 - Magnetization (M) measured as a function of magnetic field strength (H) for a $Ti_{0.93}Co_{0.07}O_{2-\delta}$ film deposited on $SrTiO_3$ (001) at room temperature (300K) [6].

Following this report, synthesis of cobalt doped thin films has been achieved by a variety of methods including spray pyrolysis [12], sol-gel [56], solid state reaction [57], spin-on technique [58], oxygen-plasma-assisted molecular-beam epitaxy (OPA-MBE) [7], and reactive co-sputtering [10] and the RTF properties of these films were confirmed. However, various values of the saturation magnetic moment per Co atom were observed, ranging from $0.32\mu_B$ to $1.7\mu_B$ [6, 10, 59].

The reason that Co-doped anatase films have RTF characteristics and various saturation magnetic-moment-per Co atom values, however, is still unclear. Some researchers [7, 60, 61] have suggested that the observed FM behaviour is caused by cobalt cations substituted into the anatase lattice, the carrier-induced interaction between the cobalt atoms is the reason for film ferromagnetism [62]. The structure of Co in anatase is octahedral and asymmetric. It is the same as Co substituted in to the Fe_3O_4 lattice to form $CoFe_2O_4$, as it is suggested that this environment enhances the magnetic properties of Co^{2+} in the Fe_3O_4 lattice [63]. It may also enhance the magnetic properties of Co^{2+} in anatase. Samples were judged by X-ray absorption and normal-emission X-ray photoemission spectroscopy shows only +2 Co state and according to the data measured by VSM and super conducting quantum interference device (SQUID) Co^{2+} is in low spin state as its magnetic moment value is close to the low spin (S=1/2) state of Co^{2+}. Moreover, cobalt is well distributed in the film with no aggregation observed in TEM and SEM images [7, 60].

Chambers *et al.* [7, 64] used synchrotron radiation to measure Cobalt K-shell X-ray absorption near-edge structure (XANES) and extended X-ray absorption fine structure (EXAFS) of the film. The first one is used to identify oxidation states and fractional d-electron density of the atoms in materials, while the second provides the local structure of the atoms and detects the distance, amount and the species of the atoms. They agreed that in the films Co is in the +2 oxidation state, no Co metal was observed and they found that the local structure of Co strongly resembles that of Co in $CoTiO_3$ (distorted octahedral cage) rather than that of Co in CoO (undistorted

octahedral cage). Moreover, the spherically-averaged effective coordination number of cobalt, N, is calculated: N = 5.45±0.3. This result is expected since if Co (II) is substituted for Ti (IV) in the lattice, in order to maintain charge neutrality one oxygen vacancy must be created for each Co (II).

Others [9, 10, 65] believed that since the solubility of Co is low during the deposition process, the Co in the films is not only substituted into the film but also the remainder forms clustered Co metal. The cluster size (about 20-60 nm) was also suggested in the film by magnetic circular dichroism (MCD), FEG-SEM, and time-of-flight secondary ion mass spectroscopy (TOF-SIMIS). Considering that the magnetic moment is very large (1.18-1.55μ_B per Co atom or even higher), it is thought clusters of Co metal in these films generated the observed RTF properties.

More recently, a new theory suggesting that oxygen vacancies play an important role for film room temperature ferromagnetic behaviour was reported by Liu *et al*[11] as it is observed that the magnetic moment strongly increased after films were annealed in vacuum and when annealed in air again, the magnetic moment decreased. Moreover, only when films were annealed in vacuum were the oxygen vacancies observed to form. This suggestion is supported by other authors [62, 66, 67] who reported that when Co^{2+} substitutes for Ti^{4+}, an oxygen vacancy forms near the Co site to compensate the balance of the charge, and a pyramidal structure is formed by the remaining five oxygen anions. The crystal field is reduced in this structure and the spin state of Co^{2+} is enhanced. The ferromagnetism arises because of exchange interactions between Co^{2+} cations via Co–O–Co; it is thought that oxygen vacancies near Co^{2+} sites are essential to this kind of exchange interaction. The strong interaction between Co^{2+} cations and oxygen vacancies increases the local magnetic moment. The reason for this is still controversial. In general, it suggests that the growth process, not only the growth conditions, for example, deposit temperature, anneal temperature and applied oxygen pressure, but also the growth technique have significant influence on the film properties, especially for the TiO_2 films [61]. After

Matsumoto *et al.*, other ferromagnetic materials which have room-temperature ferromagnetism for DMS are reported by other researchers gradually, such as Co doped ZnO [68], Ti doped α-Fe_2O_3 [69] and Mn doped SnO_2 [70].

Cobalt Doped ZnO Materials

In addition to TiO_2, other compounds can also be used as a matrix. Considering that ZnO is a II-VI compound semiconductor with wide bandgap energy (about 3.35eV) and even though the nature of it is n-type semiconductor it can change to a p-type semiconductor by co-doping. It is widely studied by researchers for producing oxide-diluted magnetic semiconductors [71]. ZnO crystallizes in the hexagonal structure, the lattice parameters are a =3.25Å and c = 5.12 Å [72].

Cobalt doped ZnO films were successfully produced through pulsed laser deposition (PLD) and laser molecular beam epitaxy (MBE) *etc.* However, the solubility of the cobalt dopant they observed are not the same [71], the range is from 10% up to 50%. The reason for these various values may be that the different deposition technique makes Co distribution inside the ZnO wurtzite structure different. It should be mentioned that when cobalt substitutes in the film it does not change the wurtzite structure of ZnO and the changes of the c-axis lattice constant follows Vegard's law [73].

According to different growth methods the resulting magnetic properties for the Co doped ZnO films are different. For example, some of the authors that used the PLD technique reported that FM was observed above room temperature, whereas others who used the MBE method found no evidence of FM for these films [71]. Again these differences chould be attributed to the growth method and the growth conditions. Prellier *et al* [74] reported that even though the hysteresis of the magnetization is very small the film is ferromagnetic at around 300K. They suggested that this ferromagnetic effect has no relationship with the cobalt clusters

since the transition from the ferromagnetic state to the paramagnetic state can be observed clearly. The saturation magnetic moment per Co atom was $0.7\mu_B$ for a $Zn_{0.92}Co_{0.08}O_{2-\alpha}$ film which is considered very small when compared to $1.7\mu_B$/Co of metallic Co; it is suggested that the state of the Co in the film could be Co^{2+}.

Kim *et al* [75] reported that as the cobalt content varies three types of magnetoresistance (MR) behavior were observed at low temperature (<20K). When x = 0.02 the only negative MR was shown; x = 0.15 only positive MR was shown and x = 0.10 negative MR and positive MR were observed close to H_{max} and at weak H respectively. When the temperature was above 50K all the samples exhibit a weak negative MR.

Cobalt is not the only dopant that has been used in DMS systems. Others such as Mn, Fe and V can also be utilized, as long as it is a 3d transition element. Even though additional work is needed to study the reason for the magnetism in oxide-diluted magnetic semiconductors, this type of DMS system still has a bright future.

2.2 Preparation of Ceramic Oxide Films

There are several routes to prepare ceramics oxide films, such as the sol-gel method [76, 77], chemical vapor deposition [78], sputter deposition [79], pulse laser deposition [80], and electrodeposition [17, 81]. Among them there are three very common routes which will be discussed here: sputtering, sol-gel and electrodeposition.

2.2.1 Sputter Deposition

In reactive sputter deposition atoms and small molecules are ejected from a target surface and travel through the "discharge" together with a reactive gas to the substrate (Figure 2.5). The kinetic processes at the surface of the target, in the gas phase, and at the substrate control the chemical reactions which can determine phase formation of the film. Since the film growth procedure is not under equilibrium conditions, reactive sputter deposition is suitable for technologically controlled growth of non-equilibrium structures, for example, ceramic phases which have high melting points grown near room temperature, nanoscale layered ceramics, metastable ceramic phases as well as ceramic-metal structures [82].

A schematic of reactive sputter deposition is shown in Figure 6. This geometry is named 'planar diode'; the source of coating material known as 'target' and the substrate are put on the cathode, and the anode respectively in a vacuum chamber. The pressure of the chamber is in the range of 10^{-7} torr with a continuous flow of a reactive gas, for example, oxygen being used to backfill the evacuated chamber in order to provide ion bombardment which is necessary for sputtering. The pressure of the sputtering gas is in the range of 10^{-3} -10^{-2} torr [83].

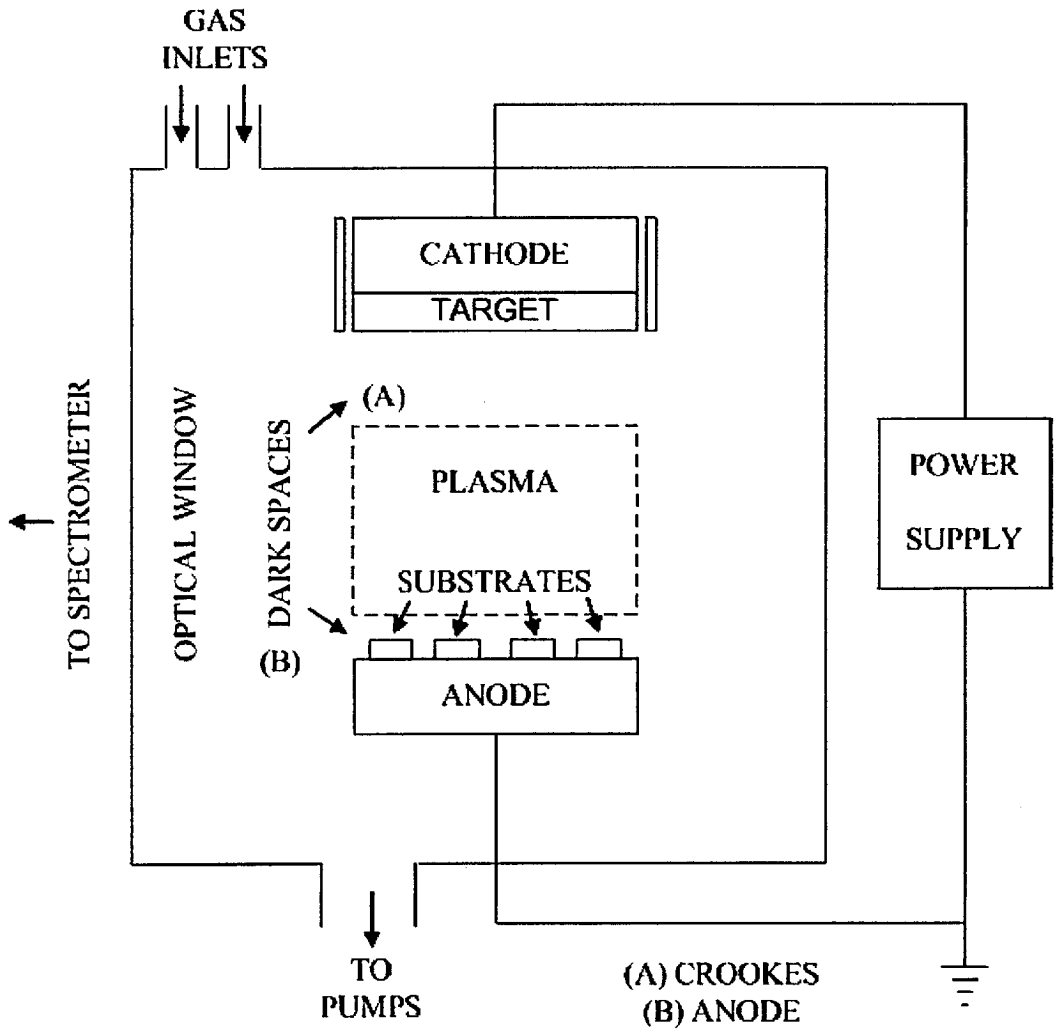


Figure 6 - Schematic graph of sputter deposition, after [82].

The deposition process includes three steps: first, atomic, molecular, or ionic species must be produced on the cathode as needed; second, transport these species to the anode (substrate) through a medium and third, growth on the substrate via chemical or electrochemical reaction [84].

The cathode receives a large negative voltage (on the order of one kilovolt) to initiate positive-ion bombardment on the target surface. A self-sustained glow discharge is formed by the sputtering gas. For an electrical conductor target direct current (dc) excitation can be used, however, for nonconducting targets or if it is reactive sputter deposition radio frequency excitation must be used.

When the high negative potential transport from the target surface to the interface of Crookes dark space/plasma the potential decreases to ground (Figure 5 (A)) and then increases to a positive value in the plasma. In the anode dark space the potential changes again. Because of the strong negative cathode field, the charged particles in the Crookes dark space (also known as 'cathode dark space') go through a beam-like motion. Therefore, when positive gas ions from the plasma enter the Crookes dark space, the kinetic energy is obtained by accelerating in the negative cathode field, and then hitting the target surface, after this; through the momentum transfer during a collision cascade or knock-on process target atoms and small molecules are ejected.

The ejected atomic, molecular, or ionic species are then transported to the substrate and condense on the substrate surface. This is how the film is deposited on the substrate [85-87]. The formation of the film contains two steps; nucleation and growth [84].

It is believed that sputtering is a very effective means for large area TiO_2 coating because it provides a high uniformity of film thickness and quality. However, the deposition rate of sputtering TiO_2 film is slow [88].

2.2.2 Sol-gel Deposition

Sol-gel deposition starts with a colloidal suspension, in which 'sol' means ceramic particles are dispersed in a liquid or polymerizable metallorganic precursor, and then aggregated to form a solid called 'gel'. Following this stage, thermal treatment at high temperature is employed to convert the coating to dense (or porous) oxide ceramics [89]. Sol-gel synthesis can be used to produce electrochromic layers on windows [90], dielectric coatings [91] and ferroelectric thin films for electronic devices [92].

Figure 7 shows the flow diagram for preparation of coatings by sol-gel methods. As can be seen from the diagram, there are mainly three steps to prepare the sol-gel coatings: coating solution preparation, deposition and drying and thermal treatment. As mentioned previously, the coating solution is made of colloidal or metallorganic ceramic precursors which are most commonly metal alkoxides, $M(OR)_n$, where, M is a metal, n is the valence of the metal, (OR) is an alkoxy group, for example, R is ethyl, (C_2H_5), or methyl, (CH_3). The prepared solution is then deposited onto a substrate; the layer is liquid, after the solvent evaporation the coating becomes solid. The processes of drying, pyrolysis of residual organics, densification and crystallization all occur during thermal treatment, and the inorganic ceramic oxide formed [89].

The drawbacks of sol-gel deposition are, it is difficult to produce thick coatings without cracks (normally less than 1μm), during thermal treatment some metastable crystalline phase may form, and the viscosity of the solution is easy to change with aging and exposure to atmospheric moisture.

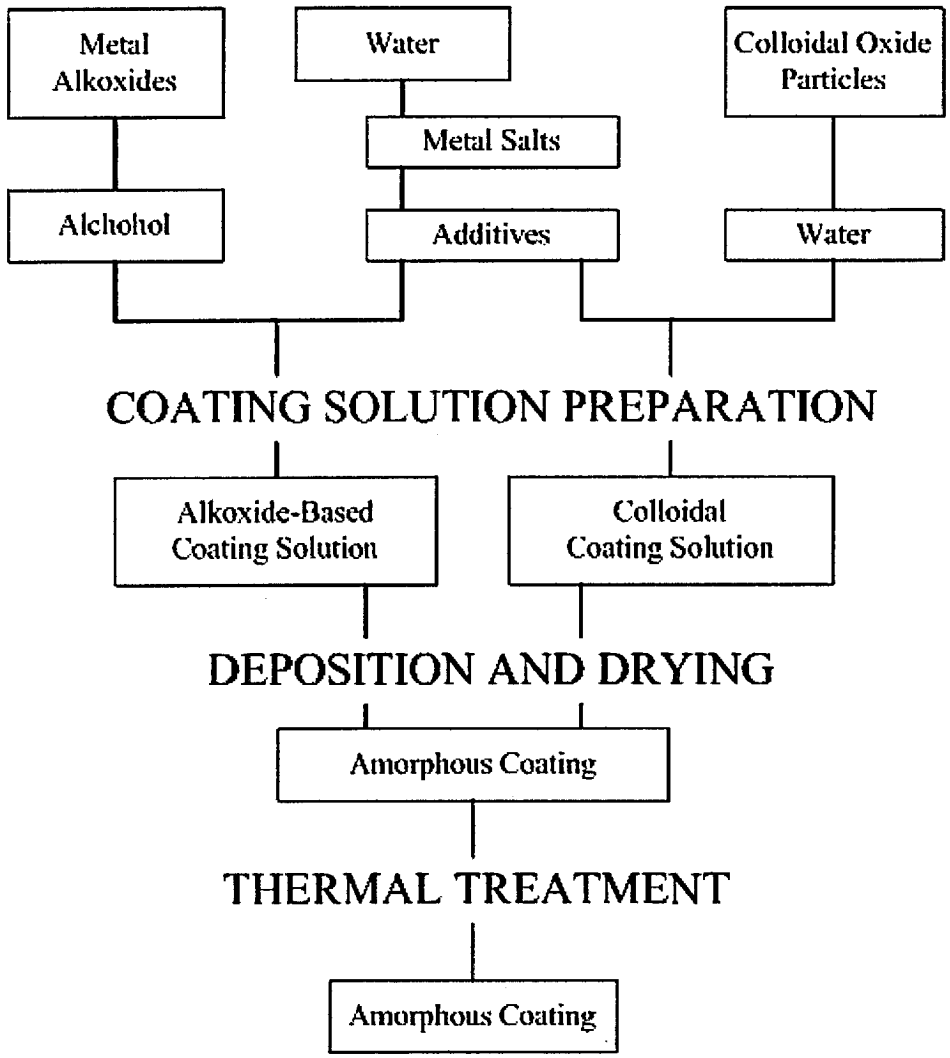


Figure 7 - Flow diagram for preparation of sol-gel coatings, after [89].

2.2.3 Electrodeposition

Electrodeposition is a type of deposition that is driven by an electric field in order to form certain sorts of films or powders. During recent years the electrodeposition method has commonly been used to prepare electroceramic powders and films [13, 14, 93-96]. Switzer *et al.* [95] reported that there are mainly two categories for electrosynthesis, the first one is redox change, in which a metal ion or complex is oxidized at the electrode surface. It is based on a change of the metal oxidation state.

This is done anodically for AgO films [96], Fe_3O_4 films [97], and ceramic superlattices [98] *etc.* The second category is the electrogenerated base method that uses a cathodic process to generate hydroxide at an electrode surface causing supersaturation followed by precipitation of the ceramic material; examples are CeO_2 [99] films, ZnO [100] films and PbO films [101]. The particle size can be controlled by the applied current and bath temperature [99]. Switzer et al. successfully electrodeposited epitaxial films on single crystal substrates [102, 103]. These authors suggested that these epitaxial films have thermodynamically controlled orientations as they are determined by the film free energy of formation on the single crystal surface, which is bonds that form between atoms in the substrate and the film control the orientation of the film [104]. Amblard *et al.* [105] studied the texture of thick Ni films on polycrystalline substrates. They suggested that a competitive growth mechanism following grain coalescence induced film texture. In this study we concentrate on films produced by cathodic electrodeposition.

Zhitomirsky *et al.* divided cathodic electrodeposition technique to two parts, one whereby a charged suspension of particles are dispersed into a solution and move to the electrode. This is known as electrophoretic deposition (EPD). The other by means of which metal ions in solution fabricate colloidal particles in an electric field in order to form a thin film is called electrolytic deposition (ELD) [106]. Both these techniques result in accumulation of ceramic particles or formation of oxide films on the relevant electrode [18].

Electrophoretic Deposition

Compared with ELD, electrophoretic deposition tends to form thick films and uses organic liquids as a suspension medium [107]. No chemical reactions occur in the solution, charged particles move to the cathodic electrode because of the attraction of the oppositely charged ions. EPD provides important advantages in the deposition of complex compounds and ceramic laminates.

Cathodic Electrodeposition

Zhitomirsky [93] modified cathodic electrodeposition as a process which is achieved via the hydrolysis of a metal salt solution using an electrogenerated base such as OH^- in order to form oxides, hydroxides or peroxides on the cathodic electrode. Hydroxides and peroxides can then be converted to oxides by thermal treatment.

Compared with some other methods such as chemical vapor deposition, sputtering and sol-gel deposition, cathodic electrodeposition provides several interesting advantages [108]: (1) the whole process takes place at low temperature and only demands atmospheric pressures, (2) due to this requirement for only simple apparatus it is a cost-effective method and (3) it is easy to control the film thickness and weight via adjustment of such parameters as, for example, deposition time, current density and cell voltage.

Electrogeneration of base

Typically, when an electric current is passed through a metal salt solution, the metal is deposited at the cathode [109]. This principle is widely used by plating technologists to obtain metal coatings. However, according to the deposition potential, choice of anions and the pH of the solutions, various other reactions take place at the cathode as well. They include:

(1) Reactions which consume H^+ ions such as

(a) $2H^+ + 2e^- \rightarrow H_2$ 2.1

(b) $NO_3^- + 2H^+ + 2e^- \rightarrow NO_2^- + H_2O$ 2.2

(c) $NO_3^- + 10H^+ + 8e^- \rightarrow NH_4^+ + 3H_2O$ 2.3

(2) Electrolysis of water

(d) $2H_2O + 2e^- \rightarrow H_2 + 2OH^-$ 2.4

(3) Anion (for example, nitrate) reduction reactions

(f) $NO_3^- + H_2O + 2e^- \rightarrow NO_2^- + 2OH^-$ 2.5

(g) $NO_3^- + 7H_2O + 8e^- \rightarrow NH_4^+ + 10OH^-$ 2.6

The pH of the electrolyte is increased near the electrode for all these reduction reactions. Therefore, these reactions effectively compete with the metal ion reduction reaction. In this case, the amount of OH^- ion in solution is one of the most important conditions for electrodeposition. The OH^- in this solution is called an electrogenerated base.

In recent years more and more interest has focused on employing EPD and ELD techniques to fabricate advanced materials, such as electrodes and films for solid oxide fuel cells, fiber-reinforced and graded ceramic composites, and nanostructured materials as well as a variety of advanced films and coatings for electronic, biomedical, optical, catalytic and electrochemical applications [110]. ELD is especially used in the preparation of nanostructured films for various applications and to provide the basic conditions for the design of novel materials and devices. Important areas for future development include electrode materials, ferroelectric and magnetic films, hybrid films, photonic crystals and materials for capacitors.

Despite the fact that ELD has many significant advantages, it does have some problems [111, 112], several of which are now discussed, together with suggestions on how to resolve them.

The first problem encountered when ELD is used to form titania films is that water and nitrates cannot be used. This is because titanium nitrate is not a stable compound and moreover, other Ti^{4+} salts such as $TiCl_4$ are hydrolyzed immediately in water to form a titanium hydroxide precipitate.

However, as mentioned previously, water and nitrate are important cathodic reactants for OH^- generation and researchers have therefore looked in detail at this obstacle. This problem has been solved by Zhitomirsky through using the peroxocomplex of titanium ($[Ti(O_2)(OH)_{n-2}]^{(4-n)+}$) instead of titanium ions [113]. The titanium peroxocomplex is more stable under certain conditions in aqueous solutions. Therefore, water can be used as a solvent and as the source of OH^- groups, which is necessary for the deposition process. The way to fabricate this complex is by adding a small quantity of hydrogen peroxide into the solution. The whole reaction is shown below [114]:

1) Solution preparation, considering the stabilization of Ti cation species, titanium peroxo complex is used as precursor, the reactions are:

$$TiCl_4 \rightarrow Ti^{4+} + 4Cl^- \qquad 2.7$$

$$Ti^{4+} + H_2O_2 + (n-2)H_2O \rightarrow \left[Ti(O_2)(OH)_{(n-2)}\right]^{(4-n)+} + nH^+ \qquad 2.8$$

2) Cathodic electrodeposition of oxyhydroxide, titanium peroxocomplex combines with OH^- and H_2O to form hydrated titanium peroxide film in electrochemical cell,

$$\left[Ti(O_2)(OH)_{(n-2)}\right]^{(4-n)+} + nOH^- + kH_2O \rightarrow TiO_3 \cdot (H_2O)_x \qquad 2.9$$

3) Thermal treatment, the as-deposited film is heated to dehydration and decomposition.

$$2TiO_3 \cdot (H_2O)_x \rightarrow 2TiO_2 + 2xH_2O + O_{2(g)} \qquad 2.10$$

In summary, titanium tetrachloride is dissociated in methanol at low temperature and reacts with hydrogen peroxide and water to form the peroxocomplex, after this the complex is hydrolyzed by the electrogenerated OH^- formation of the titanium peroxide on the cathodic electrode. The final step is to heat the as-deposited film in the furnace which then converts the hydroxyl complex to titanium dioxide.

Complex oxide compounds such as $ZrTiO_4$ and PZT were obtained via the peroxoprecursor method as well [108]. In addition, the research literature also confirmed that the use of the peroxoprecursor approach would allow production of stoichiometric deposits. Since for individual components the deposition rates are different, however, by using peroxoprecursor approach hydrolysis reactions result in the formation of complex preoxospecies and then form complex oxides after thermal treatment. $ZrTiO_4$ and PZT films were obtained after thermal treatment of the precursors at relatively low temperatures, compared with the temperatures of formation of these materials via wet chemical methods. However, in order to have a better understanding of the mechanism of deposition using peroxoprecursors much more investigation is needed.

A number of researchers [93, 94] confirmed the advantages of adding H_2O_2 into the aqueous solution. They reported that it can not only form titanium oxide films on the

substrate but can also make the films more continuous and uniform with significantly less cracking.

A major problem which all 'wet' chemistry methods of productions has is that it is difficult to get thick films without cracks. When the thickness of the film is below 0.3μm no cracks can be detected. In most circumstances cracks will appear when the thickness of a film is more than 1μm, probably because of the non-uniform contraction of the wet coating and drying shrinkage, the roughness of the substrate surface also may initiate cracking [94, 101]. In general, films produced by physical deposition methods, for example, pulsed laser deposition when thickness is on the order of 0.5 μm also exhibit cracking [115].

The evaporation rate of H_2O from the gel surface, R^eH_2O, is faster than the diffusion rate of H_2O from the gel bulk to the surface layer, R^dH_2O. If $R^eH_2O > R^dH_2O$, stress will build up on the gel surface due to the shrinkage of the surface which contains less H_2O than the bulk gel layer. Therefore the greater the deposition time or deposition thickness the less R^dH_2O will cause large stresses and resulting increase in the width of the crack. To date, there is little literature on the effect of the heat treatment on the cracking of the films.

If electrodeposition is employed for depositing ceramic films, how to provide the desired strength of film adhesion is one of the most important things that should be taken into account. There are several factors that influence the adhesion of the film [107, 116]:

1. Certain amounts of additives, such as hydrogen peroxide and N, N-Dimethyl –Formamide (DMF), improve the film adhesion.

2. Low current density, for example, 5 $mA \cdot cm^{-2}$, prevents the spallation of the films.

3. Increasing the deposition duration (more than 15mins) will also improve adhesion; however, this will make films become thicker.

4. If materials with high electrical conductivity and inert to hydrogen bonds were used as a substrate, this will exhibit poor film adhesion. This means for example that platinum, which is well known as an inert material, is difficult to use as a substrate. Active substrates are generally considered better at improving adhesion of films compared with inert substrates. However, ceramic films deposited on platinum substrates have a wide range of applications. Therefore if this problem could be solved, certain kinds of new devices could be fabricated.

5. Some times, even through the bonding is strong the interfacial morphology may lead to easy fracture.

6. Stress gradients, no matter whether they are from intrinsic or applied stress, may result in adhesive failure though chemical bonding is high.

The mechanism of electrodeposition can be viewed as the hydrolysis of solutions by an electrogenerated base, with the formation of colloidal particles of the peroxoprecursor near the cathode and their subsequent electrophoretic motion toward the cathode, resulting in the formation of the deposit. However, this mechanism has not been clearly understood by researchers [93]. Zhitomirsky et al. [117] suggested that a local pH increase influences the mechanism of the deposition, this is because increasing pH results in precipitation of a peroxo-titanium hydrate.

One important recent suggestion is that the formation of a ceramic deposit during ELD is caused by flocculation introduced by the electrolyte[113]. In attempts to fundamentally understand the exact mechanism of deposition, the classic Derjaguin, Landau, Verwey and Overbeek (DLVO) theory of colloidal stability has been applied [112, 118].

Therese and Kamath [109] have summarized the positive features of electrochemical synthesis, in order to distinguish it from other kinds of synthetic methods.

1. Electrochemical synthesis can form products that are impossible to obtain by chemical synthesis due to the fact that it has a very high potential gradient (about $10^5 Vcm^{-1}$) at the electrode.
2. The coatings can be deposited on various substrate shapes.
3. It is a low temperature technique.
4. Kinetic control and thermal dynamic control can be exercised by controlling current density and cell potential respectively.
5. Varying the bath composition can control the composition of a film.
6. The procedure of experiments is simple and apparatus is cheap.
7. Can be deposited (usually) from aqueous solutions.

However, there are also disadvantages, such as it is difficult to get crack free films because of the shrinkage during drying process, and deposits can only be fabricated on conducting substrates.

Despite the fact that electrodeposition has some disadvantages, it is gaining increasing interest as a ceramic processing technique for a variety of technical applications [103, 116].

Chapter 3.0 Experimental Procedure

3.1 Preparation of TiO_2 films

In this section, the experimental procedures, deposition procedure, solution preparation, substrate preparation and the thermal treatment of the TiO_2 films are described. The experimental set up for the cathodic electrodeposition of TiO_2 films is introduced in order to understand the requirements for each solution and substrate and the essential steps in the synthesis procedure. Moreover experimental techniques that can be used to characterize the ceramic deposits are also discussed here.

3.1.1 Cathodic Electrodeposition of TiO_2 Films

To enable the electrodeposition of the film, a conventional three-electrode cell was used, Figure 8. A mercury sulfate electrode (MSE) was used as the reference electrode (0.68 vs. NHE); Pt wire was used as the counter electrode, with the Pt, Ti or Si substrate being the working electrode. The prepared solution discussed in section 3.1.2 was used as the electrolyte. The electrochemical cell was immersed in a large glass beaker that contained iced water to keep the temperature of the solution below 2°C during the experiment.

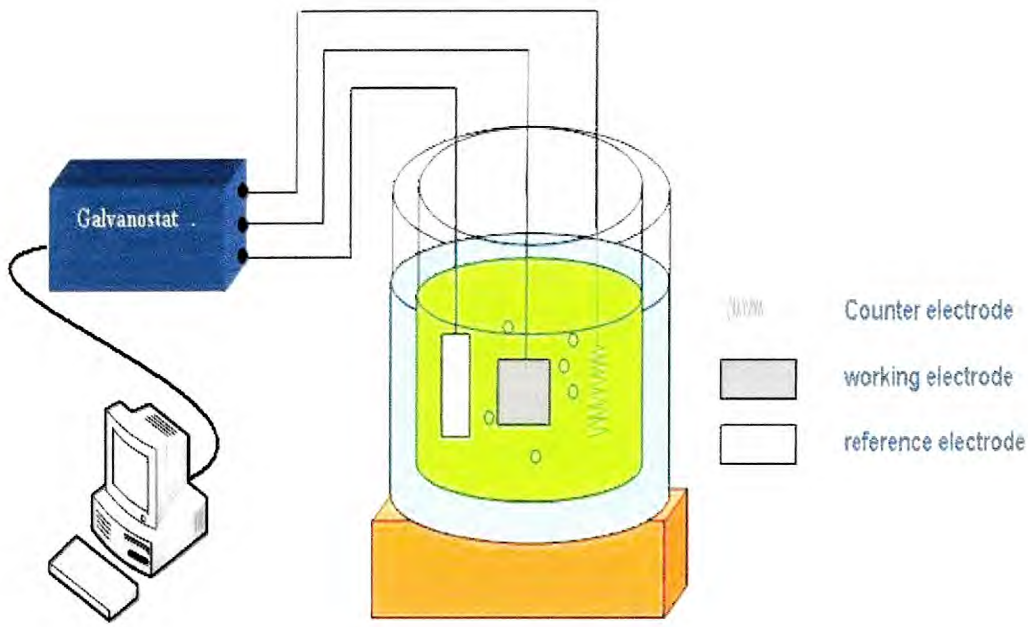


Figure 8 - Schematic representation of the experimental set up of the 3-electrode cell used in the electrolytic deposition of ceramic films. Counter electrode: Pt wire; working electrode: Pt or Ti foil; reference electrode: MSE.

The procedure developed by Zhitomirsky [17] was followed for the electrolytic deposition of TiO_2 films. Since $TiCl_4$ is very unstable at room temperature, the temperature of the whole electrodeposition procedure was controlled to between 1and 2°C; NaCl was used in the iced water to maintain the temperature. A constant current was applied by an ACM GillAC galvanostatic instrument (model: Auto AC DSP) linked to a windows based computer to record data and control the galvanostat.

However, due to the voltages (up to 13 V) of the experiment being beyond this instrument's upper limit (8 V), a small voltage meter (model: Auto-range digital mutimeter 22-163) was used and data recorded manually. The duration of the experiment was varied from 15 to 45 mins. Since all of the substrates were cut to

1cm x 1cm pieces and only one side is covered by deposition therefore, the average deposit area of each specimen was approximately about $1cm^2$ estimated visually.

After the experiment the sample was removed from the solution and washed gently with distilled water in order to remove Cl impurities. Each sample was then dried in air for half an hour and stored in a desiccator, before further analysis of the film was performed.

3.1.2 Solution Preparation

Before electrodeposition can be undertaken a precursor solution has to be prepared; in this case, following the lead of Zhitomirsky [17], the precursor solution consists of titanium tetrachloride ($TiCl_4$, purity>99%, BDH GPR™), methyl alcohol (Purity>99.5%, BDH AnalaR) and H_2O_2 27.5wt% (Aldrich Chemical Co. Ltd.) The total amount of the solution prepared was 1 litre.

Methanol, 720 ml, was measured in volumetric glassware and transferred to a 1L volumetric flask, to which 0.56 ml of $TiCl_4$ was dropped through a 1ml volumetric pipette (This stabilizes the Ti^{4+} in solution, since Ti^{4+} salts such as $TiCl_4$ are hydrolyzed immediately in water). After this, the solution was well mixed by turning the volumetric flask upside down several times. At this stage significant white gas evolution was observed, which is due to a small amount of $TiCl_4$ reacting with water in the air. Once the solution is well mixed the white gas disappears.

To this solution, 1.114 ml of H_2O_2 is dropped into the volumetric flask using a 2 ml volumetric pipette. The colour of the solution suddenly changed from colourless to light red, which suggests the tetravalent titanium peroxocomplex is formed [119]. Finally, 240 ml of de-ionized water was added to the volumetric flask in order to

provide a volumetric ratio of methanol/water = 3/1. The last step is to add the prepared well mixed methanol-water solution (3:1) to the volumetric flask, to make the total amount of the solution 1 liter. The reaction for solution preparation is shown in equations 2.7 and 2.8. $TiCl_4$ react with H_2O_2 and H_2O form titanium peroxocomplex solution. The solution was left to age for two or three days for complete reaction. The whole procedure of cathodic electrodeposition is described in Chapter 2.2.3.

$$TiCl_4 \rightarrow Ti^{4+} + 4Cl^- \qquad 2.7$$

$$Ti^{4+} + H_2O_2 + (n-2)H_2O \rightarrow [Ti(O_2)(OH)_{n-2}]^{(4-n)+} + nH^+ \qquad 2.8$$

3.1.3 Substrate Preparation

Platinum foil (purity 99.99%, 0.125 × 25 × 25 mm, weight 1.676 g)) was obtained from Advent Research Materials Ltd to be used as the substrate on to which the ceramic film would be deposited. The platinum foil was divided in to individual pieces (10 mm x 10 mm) using scissors. A second substrate, titanium, (purity 99.99% obtained from Advent Research Materials Ltd), was also cut into small pieces (10mm x 10mm) using scissors.

Prior to deposition each of the substrates were polished using a polishing machine (model: BuehlenrMetaserv universal-polisher) with both 3μm and 1μm diamond media in order to obtain a smooth surface.

After polishing, the substrates were washed in methanol and deionized water respectively, to remove dust. The final step in the substrate preparation was cleaning

in an ultrasonic bath using acetone to degrease the sample and finally a rinse in de-ionized water.

3.1.4 Thermal treatment

There are three atmospheres that were used during crystallisation of the as-deposited film: air, Ar, and Ar/H_2 (10% of hydrogen). For the as-deposited samples, an Elite Thermal Systems Ltd furnace (model: BRF15/5-2416CG) was used at temperatures of between 400 °C and 1000 °C with a heating rate of 10 °C per min used for a period of 60 mins. For the as-deposited samples annealed in Ar and Ar/H_2, a tube furnace with atmosphere control was used. Before heating the alumina furnace tube was purged with either Ar or Ar/H_2 for half an hour to ensure the pO_2 of the environment was constant.

3.2 Preparation of Co doped TiO_2 films

3.2.1 Solution Preparation

To prepare cobalt doped TiO_2 films a measured amount of $CoCl_2 \cdot 6H_2O$ (H&W Ltd.) was added to the previously prepared precursor solution (Section 3.1.2) and stirred. The amount of $CoCl_2$ added corresponded to the required stoichiometry of the Co doped TiO_2. Two ratios of Ti: Co were evaluated, 10:1 and 20:1 in molar ratio respectively.

3.2.2 Sample Preparation

Two substrates were used in the preparation of these films. As previously described (section 3.1.3) Ti was used and prepared by carefully polishing and cleaning.

To provide a suitable substrate for electrical/magnetic measurements a Si substrate was used. A Si wafer (Compart Technology Ltd.) was cut into small pieces (approximately 2 x 1cm) using a diamond pen. Each piece was then dipped in dilute HF (2.6 ml 48.5% HF, 20 ml de-ionized water) for 15 s to remove silicon oxide, and then cleaned in acetone in an ultra-sonic bath for 10 mins. Finally the substrates were rinsed with de-ionized water.

3.2.3 Cathodic Electrodeposition of Co-TiO_2 Films

The conditions for depositing the cobalt doped films were identical to those described previously for the preparation of TiO_2 films (section 3.1.1).

3.2.4 Thermal Treatment

There were also three atmospheres used to control the as-deposited cobalt doped TiO_2 film: air, Ar, and Ar/H_2 (10% hydrogen). An Elite Thermal Systems Ltd furnace (model: BRF15/5-2416CG) was used at temperatures of between 400 °C and 800 °C, with a heating rate of 10 °C per min used for a period of 90 mins to make sure the Co doped TiO_2 films were fully crystallized. For the as-deposited samples annealed in Ar and Ar/H_2 (10% of hydrogen), a tube furnace with atmosphere control was used. Before heating the alumina furnace tube was purged with either Ar or Ar/H_2 for half an hour to ensure the pO_2 of the environment was constant.

3.3 Analysis of the Deposited Films

There are many experimental techniques that can be used to characterize the ceramic deposits. These are essential in the investigation of both chemical and physical properties and the structure of the deposits. In this research, some of the most suitable techniques have been used.

3.3.1 X-ray Diffraction (XRD) & High Temperature X-ray Diffraction (HTXRD)

3.3.1.1 X-ray Diffraction (XRD)

The X-ray diffraction technique (XRD) is a common tool for the characterization of crystalline materials and the determination of their crystal structures [120].

The principle of XRD is as follows (Figure 9): X-rays interact with electrons in matter. When a beam of X-rays impinges on a material it is scattered in various directions by the electron clouds of the atoms. If the wavelength of the X-rays is comparable to the separation distance between the atoms, then interference can occur. For an ordered array of scattering centers (such as atoms or ions in a crystalline solid), this interference gives rise to interference maxima and minima. The wavelengths of X-rays used in X-ray diffraction experiments therefore lie between 0.6 and 1.9 Å, typical atomic interplanar spacings.

When the X-rays hit the surface of the crystals and are diffracted, the atoms or ions act as secondary point sources and scatter the X-rays. The most common approach in treating diffraction by crystals is by applying Bragg's law (equation 3.3). Bragg's law regards crystals as built-up of layers or planes such that each acts as a

semi-transparent mirror. Some of the X-rays are reflected off a plane with the angle of reflection equal to the angle of incidence, but the rest are transmitted through one plane and then reflected by the next plane.

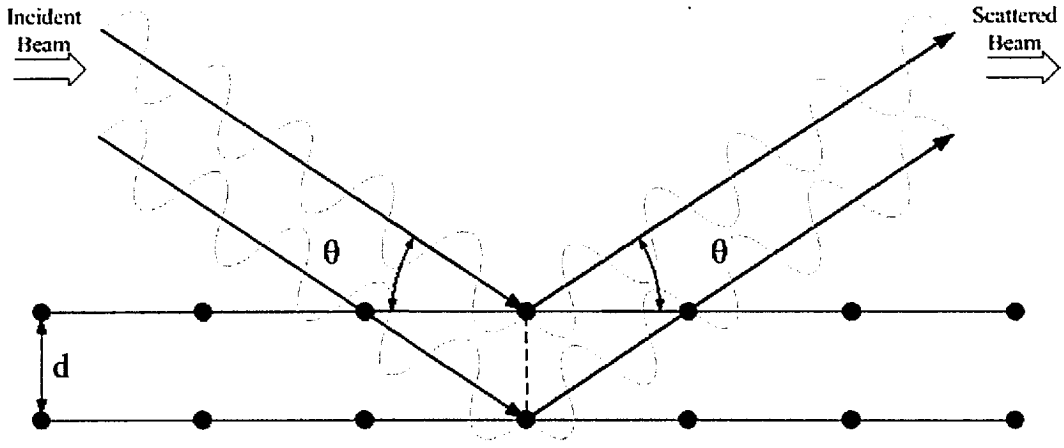


Figure 9 - A schematic diagram for determining Bragg's law

$$2d\sin\theta = n\lambda \qquad 3.3$$

Here *d* refers to the perpendicular distance between pairs of adjacent planes, which is also referred to as the d-spacing; θ, relates to the Bragg angle which is the angle of incidence; and λ is the X-ray wavelength; finally, n, is the diffraction order.

As the interplanar spacing d is observed from Bragg's law, lattice parameters of cubic, tetragonal and hexagonal systems *etc.* can be calculated. For example, lattice parameters of TiO_2, tetragonal, were calculated using the listed spacing equation [121]:

$$\text{(Tetragonal)}\, d_{hkl} = \frac{a}{\sqrt{h^2 + k^2 + l^2(a^2/c^2)}} \qquad 3.4$$

Where d_{hkl} is the interplanar spacing, h, k and l are different planes and a and c indicate the lattice parameters.

When x-rays encounter any form of material, not all of them are transmitted, they are partly absorbed. Röntgen established that the fractional decrease in the intensity I of an x-ray beam as it passes through any substance is proportional to the distance traversed, x, (also called penetration depth) [121]. The differential form is:

$$-\frac{dI}{I} = \mu dx \qquad 3.5$$

Where the constant μ is the linear absorption coefficient, it is dependent on the material properties, its density and the wavelength of the x-rays. The integration of equation 3.5 is:

$$I_x = I_0 e^{-\mu x} \qquad 3.6$$

I_0 is original intensity, I_x is intensity remaining, and the linear absorption coefficient, μ, is proportional to the density, ρ, which means that the quantity μ/ρ is a constant of the material, referred to as the mass absorption coefficient. Therefore, the equation can be written as:

$$I_x = I_0 e^{-(\frac{\mu}{\rho})\rho x} \qquad 3.7$$

According to equation 3.7, the x-ray penetration depth can be calculated.

Scherrer's formula below (3.8) is used to calculate the size of very small crystals.

$$t = \frac{0.9\lambda}{B \cdot Cos\theta} \qquad 3.8$$

Where t is particle size, λ is the wavelength of Cu K_α; B is FWHM (full width at half maximum) of the broadened diffraction line on the 2θ scale (radians).

For polycrystalline films, if most of the grains in the film are grown randomly this means the film has no preferred orientation; on the contrary, if most of the grains are oriented along a certain direction this indicates that the film has *preferred orientation* also known as texture. Texture is seen in almost all engineered materials, and it can have a great influence on material properties. X-ray diffraction also can provide a texture scan to determine whether the film has preferred orientation or not. Instead of doing one-dimensional scans, a texture scan is a two-dimensional scan in which the surface of a hemisphere in reciprocal space is scanned for the reflections (hkl) off the substrate surface. In this research, a Philips X'Pert Pro-Materials Research Diffractometer with Cu K_α radiation was used to determine film orientation.

3.3.1.1 High temperature X-ray diffraction (HTXRD)

As mentioned before (Chapter 2, section 2.3) in all ceramics and electroceramics their thermal properties change in proportion with temperature changes. However, high temperature X-ray diffraction (HTXRD, also known as in-situ XRD) has the ability to perform the characterization measurement at elevated temperatures. Compared with conventional XRD, the advantages of high temperature XRD are: it is able to reveal the elementary formation processes of film surfaces and to elucidate the relation between temperature and time during the phase transformation. Therefore, high temperature XRD is very useful in understanding the structural and phase stability of crystalline materials.

In this research, the HTXRD instrument used was a Philips X'Pert MPD with Bühler HDK2.4 high temperature chamber X-ray diffractometer. Samples can be heated both in static air and in flowing gas. For samples annealed in flowing gas the gas was purged for at least one hour to evacuate the air in the chamber prior to any measurement. A platinum strip was used to heat the sample, and also to act as the sample holder. Since the sample is heated from the back through the platinum strip, the true temperature of the sample is not exactly the anneal temperature, normally the difference is about 20 °C, and the difference increases as the heating temperature increases. The heating range is from room temperature up to 1200 °C depending on the anneal atmosphere and temperature control instrument. The heating rate is usually 60 °C/min.

The software equipped with this instrument can program the experimental process as needed. For example, some of the samples were heated from room temperature to 800 °C at a rate of 60 °C/min. the program was set as: after temperature increase every 100 °C, hold for an hour and scan once until temperature reaches 800 °C, then cool the samples again to room temperature and scan again. The duration of the scan time can also be set as the experiment demands.

3.3.2 Scanning Electron Microscopy (SEM) & Field Emission Gun Scanning Electron Microscopy (FEGSEM)

In this study, a JEOL T200 scanning electron microscope (SEM) equipped with an energy dispersive x-ray detector (EDS), a JEOL high voltage 5610 scanning electron microscope (SEM) and a LEO 1525 field emission gun scanning electron microscope (FEGSEM) equipped with energy dispersive x-ray detector (EDS) were used for surface topography and compositional analysis.

3.3.2.1 Scanning Electron Microscopy (SEM)

Normally, an SEM is comprised of: an electron gun, electron lens, spray aperture, scan coils, magnification control, scan generator and display CRT. The principle of the SEM (Figure 10) is that it uses the electron beam which is generated by thermionic emission from a metal filament through applying a voltage (in the kV range) to construct images at a high resolution magnification. The sample surface is scanned line by line by the electron beam which is focused to a spot (~ 10 nm in diameter). For each position x and y, the detector signal intensity, I, is recorded and displayed as an image I (x, y). Since the amount of emitted secondary electrons varies due to the material properties of the illuminated spot area, the intensity of the detector changes as well. Therefore, different materials have different brightness in the scan image. Compared with other instruments used in the characterization of these films one of the advantages of SEM is that sample thickness and sample preparation are less important [120].

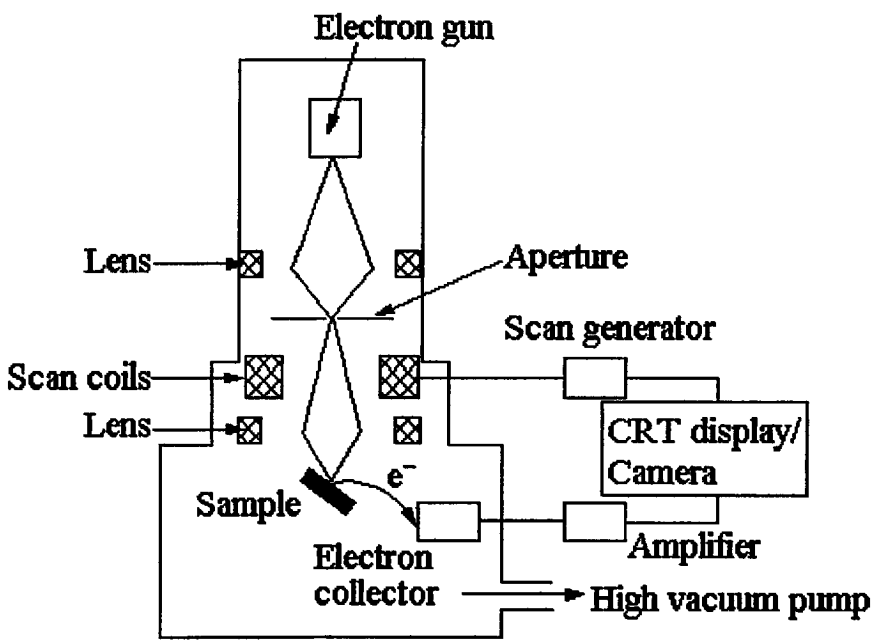


Figure 10 - Schematic diagram of a Scanning Electron Microscope [122].

Tungsten is usually used as the filament, which produces a high-intensity focused electron beam. This electron beam is then focused through a series of electromagnetic lenses, which make the electrons spiral down the column on to the sample. A sample is placed on a stage in a vacuum chamber positioned under the electron column and the path of the electron beam. SEM should be carried out under a high vacuum, normally at 10^{-6} Torr or lower. This specimen should be conductive, otherwise the electron beam would charge up the surface; for non-conducting specimens, gold or graphite should be coated on the sample surface, to avoid surface charge build-up and degradation the image definition.

3.3.2.2 Field Emission Gun Scanning Electron Microscopy (FEGSEM)

Another type of SEM technique is Field Emission Gun Scanning Electron Microscopy (FEGSEM). It can be used for imaging the sample surface topography at the nano-meter scale. The original SEM has relatively low resolution of topography. The reason that the resolution of SEM usually lower than 2 nm is because of the escape depth of the secondary electrons from a solid surface [123].

However, FEGSEM instruments are equipped with an objective lens having a short focal length and an electron gun that provides narrower probing beams and higher electron energies which means that resolutions down to 0.5 nm are possible. Considering that the ceramic oxide films in this work are all made of nano-scale particles, the use of FEGSEM becomes necessary. In this research, all the images were taken from multiple samples in multiple areas to confirm the consistency of the measurement.

3.3.2.3 X-ray Energy Dispersive Spectroscopy (EDS)

X-ray energy dispersive spectroscopy (EDS) is an analytical tool predominantly used for identifying and quantifying elemental compositions in materials [124]. Oxford

Instruments Energy Dispersive X-ray detection (EDS) in both T200 scanning electron microscope (SEM) and LEO 1525 field emission gun scanning electron microscope (FEGSEM) is used for determining the elements that are contained in a specimen. Normally, the EDS system used with SEM can detect all elements (from atomic number 4 to atomic number 92) in concentrations from 0.1% upwards.

When the incident electron beam impacts the sample surface in some cases the electrons which orbit around the atoms nuclei displace. The atom changes to an exited state due to this interaction and in order to move back to the stable state, the electrons from the outer shell therefore need to fill inner shell vacancies. The energy released during this process results either in Auger electrons that produce back scattered (BS) radiation, or by emitting X-rays. The emitted X-ray is then detected by an X-ray spectrometer and produces characteristic lines. As each line corresponds to a particular elemental material, the elements in the sample can therefore be identified [125].

It is quite useful for the researcher to confirm whether the desired sample has been produced or not. Before each sample analysis session, a standard Co is analysed in order to calibrate the computer software. Samples were analysed in several areas to ensure the consistency of the measurement.

3.3.3 Atomic Force Microscopy (AFM)

The atomic force microscope (Figure 11) is a scanned-proximity probe microscope. The scanning probe is made of a small tip which has a cone shape with elliptical cross section and the angle of the cone is 40° -50° in one direction and 50°-60° in the other. The height of the tip is ~ 10-15μm. It is used for measuring a local property such as height, optical adsorption, or magnetism. The advantage of this instrument is

that it can give images with very high resolution and also can be used on many sorts of materials, for example, metals, metal oxides and polymers. In this study an Agilent 4500 AFM is used for sample analysis.

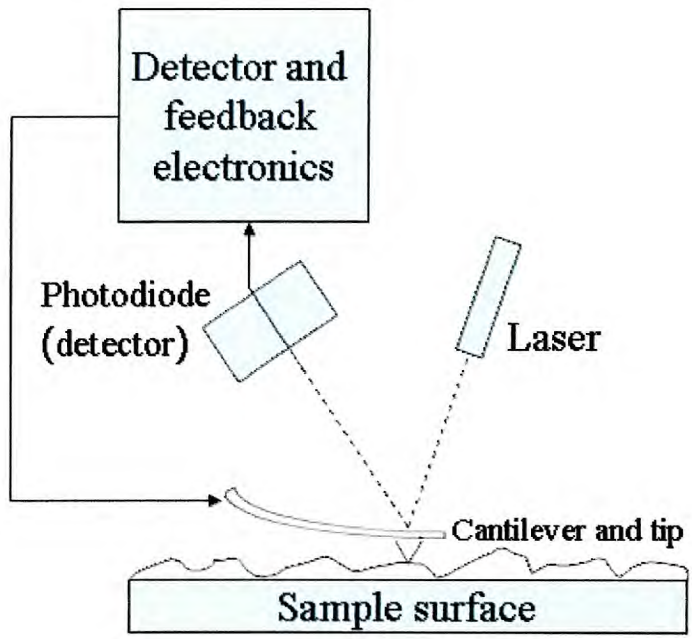


Figure 11 - Schematic diagram showing the operation of an Atomic Force Microscope

The AFM has two modes; one is the contact mode, which means that during the measurement the instrument lightly touches the sample by the tip, which is at the end of the cantilever; the other mode is the non-contact mode, which means the tip does not touch the sample. In our research, the contact mode has been used to analyze samples. It should be mentioned that the tip is very fragile and therefore, care should be taken when adjusting the tip close to the sample surface manually. And scanning should be observed at minimal possible force as determined by the tip-sample force curve.

The principle of AFM is as follows [126]: the tip is moved close to the sample surface, when the tip contacts with the sample it can measure the attractive forces (van der Waals forces) whereas, when the tip is lifted above the surface the repulsive

forces (Coulomb force) is measured. The force information is shown from the force curve.

It should be mentioned that if the distance between tip and sample surface reaches a few nanometres, van der Waals forces are strong enough to move AFM cantilevers. Therefore, when the interaction between tip and film surface occurs, there is oscillating in the cantilever which can cause deflection of the cantilever. In order to keep the deflection constant the vertical position of the tip has to be adjusted, which is achieved by applying a voltage to the vertical direction of the scanner. If the voltages applied to the scanner are divided into horizontal (x, y) and vertical (z) directions, and the corresponding deflections in these directions are measured for the whole sample surface, the AFM software can manage to determine the height of the tip (z) for the relevant surface point (x, y). This is how the topography of the sample is measured [127].

3.3.4 Focused Ion Beam (FIB)

Focused ion beam microscopy was invented in the mid 1980s and since then it has been widely used for not only sample preparation but also in semiconductor manufacturing. It has the capability of milling, imaging and depositing materials. The primary gallium focused ion beam used in FIB systems can be operated at low beam currents (as low as 1 pA) for high resolution imaging or at high beam currents (as high as 20 nA or 30 nA) to mill material from a defined area. Usually the FIB accelerating voltages are in the range of 5-50 eV. FIB instruments can either be single beam instruments or incorporated with other analytical instruments, such as secondary ion mass spectrometry (named FIB/SIMS dual platform instrument). The instrument used in this research is FIB-TEM 200 equipped with SIMS detector which is not be used in this research.

A schematic diagram of a typical FIB microscope is shown in Figure 12. As can be seen from the diagram, the basic FIB instrument consists of a vacuum system and a chamber, a liquid metal ion source (LMIS) in a column, detectors, gas delivery system, a stage for mounting samples and a computer to run the program and monitor [128].

Both ion column and sample chamber are required to be at high vacuum (on the order of $1x10^{-8}$ Torr for the column and $1x10^{-6}$ Torr for the chamber) in order to evacuate the contamination of the column and the chamber and to obviate the electrical discharges due to the high voltage in the column. The liquid metal ion source (LMIS) makes small probe sputtering possible; it can provide an ion source as narrow as ~5 nm in diameter. Gallium is commonly used as the metallic element for LMIS. After Ga^+ ions are obtained from the LMIS, they are accelerated and sent down to the ion column by a potential. The beam is first sent through a condenser lens to form the probe and then sent though objective lenses to focus the ion beam at the sample surface. It should be mentioned that compared with other instruments the FIB has a relatively large working distance (~ 2cm or less); this allows the user to observe the varied topography without worrying about field changes.

When the charged gallium ion beam scans the sample surface sputtered material, secondary ions and secondary electrons are all generated. Among them secondary electrons and the secondary positive ions are collected by an electron multiplier detector to form the FIB image. It should be noted that a small beam current is used for the FIB imaging process because the sample is subject to destructive sputtering during FIB image formation. The sputtering rate will vary as the texture of the sputtered material various.

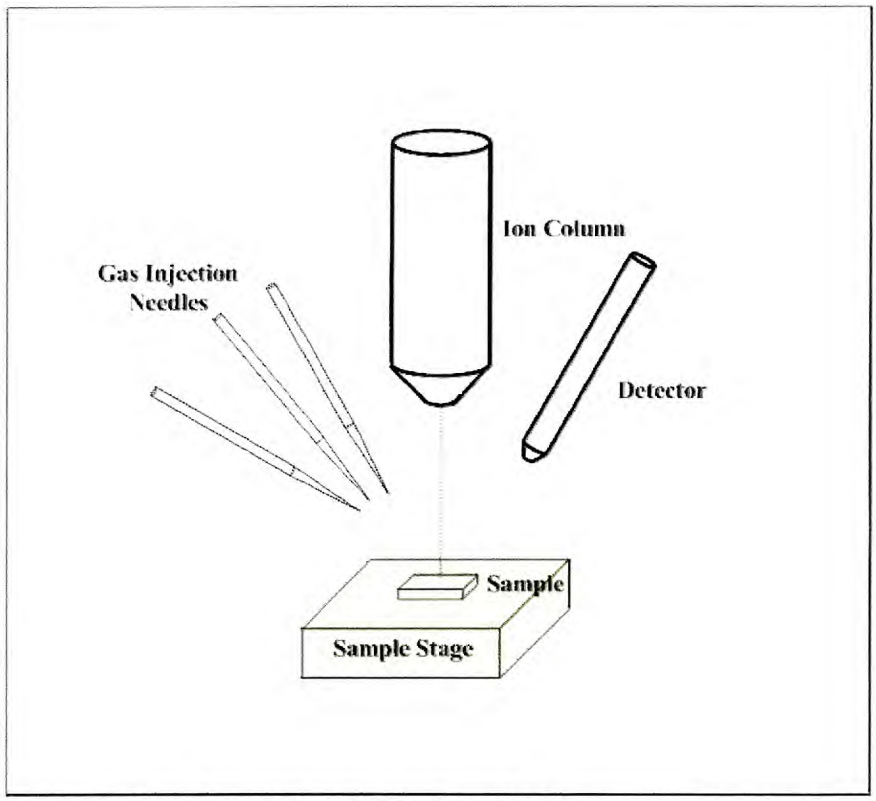


Figure 12 - Schematic diagram of a typical FIB microscope, after [128]

Milling is a significant advantage of the FIB instrument; it provides valuable microstructure information beneath the sample surface. The way of milling is performed by physical sputtering of the target. When the beam hits the sample surface the momentum transferred from the incident ions to the target results in a series of elastic collisions. Some of the surface atoms receive the kinetic energy which is strong enough to overcome the surface binding energy (SBE) and thus are able to be ejected. As the applied current increases the amount of ejected atoms increases thus milling proceeds.

In this research, milling is used to create a 'ramp' on the film surface to investigate microstructural information from beneath the sample surface, the reason for making a ramp is because it is easier to observe the situation from sample surface to the bottom of the film, and since the ramp efficiently 'stretches' the thickness observed, it is easier to perform the SIMS analysis and also for SEM observation of the film interface as well.

Figure 13 shows a brief introduction of how to make a ramp. For normal samples, the ion beam is perpendicular to the sample surface (Figure 13 a), the direction of the beam is impossible to change; therefore, the sample was rotated to have a certain angle θ with the beam (for example, θ = 10°), the beam then starts to mill the sample until it reaches the metal substrate, this step usually takes several hours, depending on what type of material is being milled and the size of the ramp. As shown in Figure 13 b, the sample is returned to the horizontal position, the white rectangular area is the created ramp, the dotted line indicates the sample interface, which is the boundary area between the film and the substrate, from the top of the rectangular area is the 'stretched' film area; from the dotted line until the bottom of the rectangular area is the substrate area. Figure 13 c and d illustrates how the observed length 'D' of the film is related to the actual length 'x' of the film: x = D tan θ, where θ is the rotated angle (Figure 13 d).

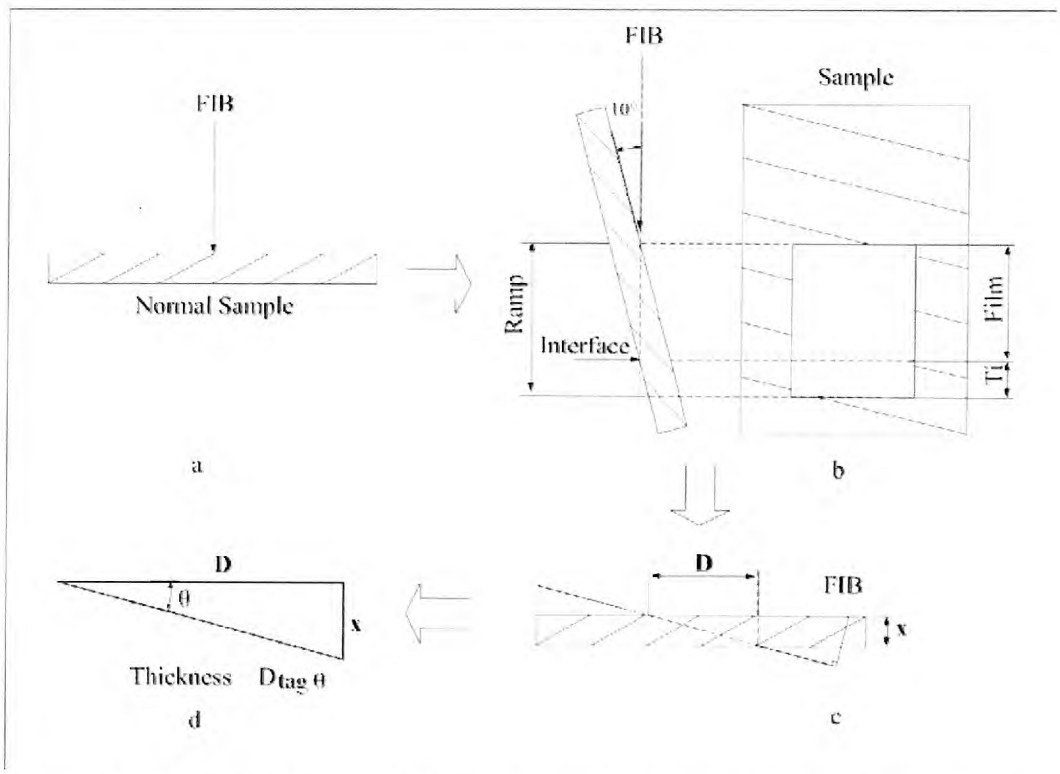


Figure 13 - Schematic illustration of the procedure used to generate ramp sections using FIB milling: D: the length from observation, x: real thickness of the film.

3.3.6 X-Ray Absorption Spectroscopy (XAS)

The X-ray absorption spectroscopy spectrum can be divided into two basic regions [129]: the near edge region, named X-ray absorption near edge structure (XANES) and the other is named extended X-ray absorption fine structure (EXAFS). The first one is used to identify oxidation states and fractional d-electron density of the atoms in materials, while the second provides the local co-ordination of the atoms and is sensitive to distance, amount and the variety of the atoms.

When the X-ray hits the sample, the sample begins to absorb the X-ray, as soon as the energy of the X-ray reaches the absorption edge of the atoms in the sample, the electron of the atom begins to absorb the photon of the X-ray and is excited. The energy of this absorption is dependent on the atom and its oxidation state, this is the XANES region.

There are two modes of XAS spectroscopy used very commonly [130]. The first one is transmission, where the X-ray beam intensity is measured both before and after the sample using ion chambers. The second one is fluorescence, where the intensity of the X-ray beam is measured before the sample and the intensity of fluorescence signal emitted from the sample is measured using a solid state detector.

In this study the experiments were conducted at Stanford Synchrotron Radiation Laboratory (SSRL) at the beamline 10-2 with the grazing incidence stage on transmission mode. A Ge 13-element detector was used. Co foil, Co^{3+} ($LiCoO_2$) and Co^{2+} ($Co(OH_2)$) standards were run at the same line to calibrate the edge position.

Chapter 4.0 Results & Discussion -- TiO_2 Films

Electrodeposition experiments were performed from stock solutions ($TiCl_4$ mixed with H_2O_2 and methanol-water) and cathodic deposits were obtained on both the Pt substrate and the Ti substrate. The colour of the as-deposited films is light green which indicates formation of peroxo bonds [131]. In order to study the deposition of TiO_2, the voltage was measured during the experiment and different characterization techniques such as SEM, FEGSEM, AFM, and XRD were used to analyze the films both before and after thermal treatment. Samples were also annealed in different atmospheres to investigate the influence of the anneal environment on film characteristics.

4.1 As-deposited TiO_2 films

4.1.1 Effect of Variation of Voltage and Time on Film Quality

4.1.1.1 Film deposited on Pt substrate

Measuring the electrode potential during the experiment provides information about the deposition process in terms of voltage with time. Figure 14 shows the measured potential of a TiO_2 film deposited on a Pt substrate. From this Figure it appears that the voltage changed during the electrodeposition. In general the voltage of the experiment is between 5 to 10 volts. In the first few minutes the voltage increased rapidly, however, after that the rate of change decreased, reaching a plateau after 33 mins until the deposition was terminated.

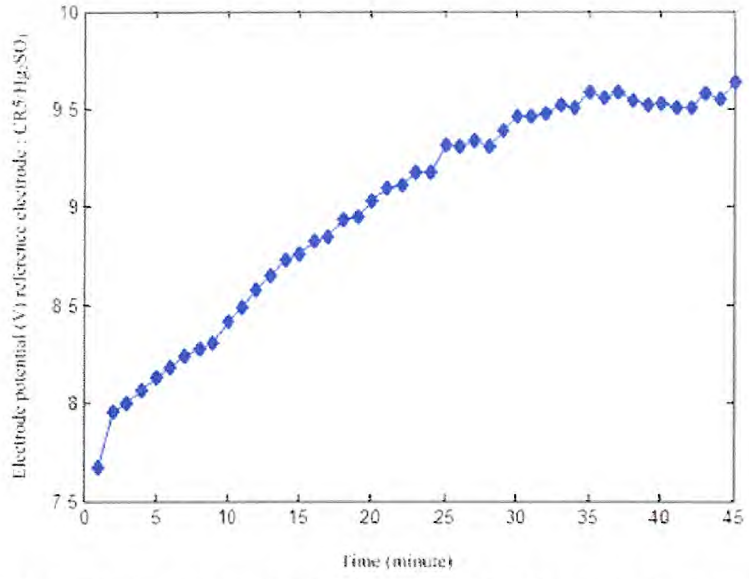


Figure 14 - Variation of electrode potential with deposition time for a TiO_2 film deposited on a Pt substrate. Deposition temperature is 0-2°C, H_2O_2 concentration of 0.01M, applied current is 20mA·cm^{-2}.

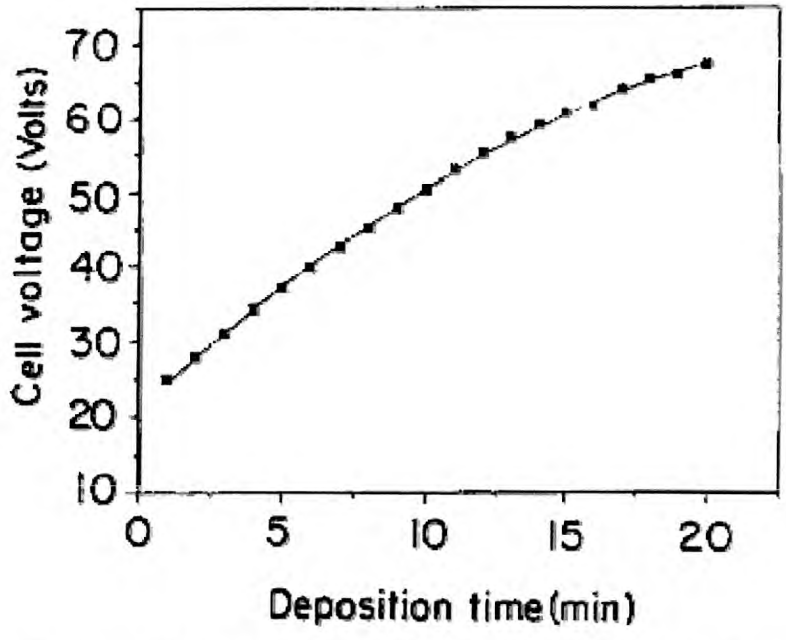


Figure 15 - Cell voltage with deposition time for TiO_2 films deposited on Pt by Zhitomirsky et al, deposition temperature is 0-2°C, supplied current is 20mA·cm^{-2}, H_2O_2 concentration of 0.01M [17]

For the galvanostatic regime the potential U is determined by equation 4.1[101]:

$$U=U_0+iR_{sol}+iR_d \qquad 4.1$$

Where U_0 is initial (open circuit) potential, it is almost constant for selected solutions and electrodes, the initial potential here is 0.5 ± 0.1V, and it is observed by measuring the cell potential before applying current density; R_{sol} is the resistivity of the solution and R_d is the resistivity of the deposit. Current density is 20 $mA{\cdot}cm^{-2}$. After current is applied on the electrodes, the conductive Ti substrate starts to generate OH^- all over the surface, therefore OH^- can react with the titanium peroxocomplex to form oxy-hydroxy-Ti films easily (shown in equation 2.9). At the beginning of the experiment, due to the zero deposit resistivity the voltage is relatively low and the deposition rate is high。

$$\left[Ti(O_2)(OH)_{n-2}\right]^{(4-n)+} + m(OH)^- + kH_2O \rightarrow TiO_3(H_2O)_x \qquad 2.9$$

According to titanium-H_2O Pourbaix Diagram [132], thermodynamically peroxide $TiO_3(H_2O)_x$ can be stably formed when the voltage is between 1.2 to 2.2 V (NHE) when the pH value >0.5. Considering that the film thickness increases during the deposition process the deposit resistance increases as well, therefore, as can be seen from the equation 4.1, the cell potential increases with the deposition time. This is the reason that the voltage increased rapidly for the first few minutes. As the deposition continues, the film continues to grow forming an insulating layer which makes the deposit resistance much higher than the beginning and result high voltage. Moreover, when the film grows to the certain thickness it prevents OH^- generation and the cell voltage tends to plateau after about 33 minutes. This implies that films form up to a limiting thickness. From the process described above, it can be determined that the electric field in the electrolytic deposition makes the formation of uniform films possible. The reason for this is: because of the deposit resistivity for

the thick area of the film the current and the deposition rate is low, therefore, film grows slowly, whereas, for the thin area of the film the current and the deposition rate is high, film grows fast.

This result is different from the result reported by Zhitomirsky (Figure15, (a) corresponds to this research) [17]. According to this author the cell voltage increases from 25 volts to 65 volts.

The deposition duration is also different. Zhitomirsky reported that the thickness of the film deposited on Pt substrate is greater than 0.3 microns after a deposition of 15 mins. In the current work, after a deposition time of 15 mins little film formation was observed. According to equation 4.1, potential U is dependent on the applied current and the resistivities of solution and deposit. Since the potential is different, this means the resistivities or thicknesses are different. Therefore, in order to increase the film thickness, the deposition time was increased to 45 mins. One possibility for this difference is that the concentration of hydrogen peroxide is greater than the reference concentration (0.01 M) H_2O_2 which could suppress hydrolysis of the titanium ion as Zhitomirsky *et al.* reported [17].

4.1.1.2 Film deposited on Ti substrate

For the film deposited on the Ti substrate the range of the voltage is from 7.5 volts to 11.5 volts. The value of the maximum voltage is slightly higher than for films deposited on a Pt substrate but comparable. This may due to the different cathodic efficiency and the different adhesions between substrate and film.

4.2 Characterisation of Electrodeposits

4.2.1 Thermal Treatment

As described in chapter 3, the as-deposited film is composed of a peroxocomplex (TiO_3 $(H_2O)_x$) and therefore, it needs to be annealed to decompose at elevated temperatures and form a TiO_2 film.

Most of the samples were heated in air to 800 °C with the heating rate of 10 °C/min and held at this temperature for one hour. The program for the thermal treatment is: heat sample from room temperature to 800 °C at a rate of 10 °C/min and hold for one hour, then cool the sample down from 800 °C to room temperature at the same rate. However, on cooling the rate is not exactly following the programmed rate, as at lower temperatures the cooling is limited by the surrounding environment. But this does not influence the quality of the film. Some of the samples were annealed to 1000 °C to avoid the anatase phase and leave only the rutile phase.

Some of the samples were also annealed in different atmospheres (Argon or Argon/Hydrogen (10% hydrogen)) to study the annealing environment influence on the film characteristics. For these samples because the air in the furnace needs to be evacuated, argon or argon/hydrogen gases were used to purge the furnace for half an hour before annealing.

4.2.1.1 Film deposited on Pt substrate

Figure 16 shows the XRD comparison pattern of a TiO_2 film deposited on Pt substrate before and after heat treatment; the scan range is between 10 and 90

degrees 2 theta. It can be seen that before annealing only peaks attributed to the Pt substrate were observed and in the AFM image shown later in Figure 21 (a) there is no evidence for a crystalline phase which indicates that the as-deposited film is amorphous. Moreover, the thickness of the as-deposited film is 0.77 $\pm$ 0.18 μm which decreases after thermal treatment because of dehydration (0.33 $\pm$ 0.16 μm). Therefore, thickness is not limiting the observation of Bragg peaks. This result agrees with Zhitomirsky *et al.* who also reported that the as-deposited film is amorphous [17]. However, after heating to 800 °C in air for one hour the situation has changed. Peaks corresponding to both anatase and rutile phases were observed, which means that the film has crystallised. The peaks attributed to the anatase phase have higher intensities than the peaks attributed to the rutile phase.

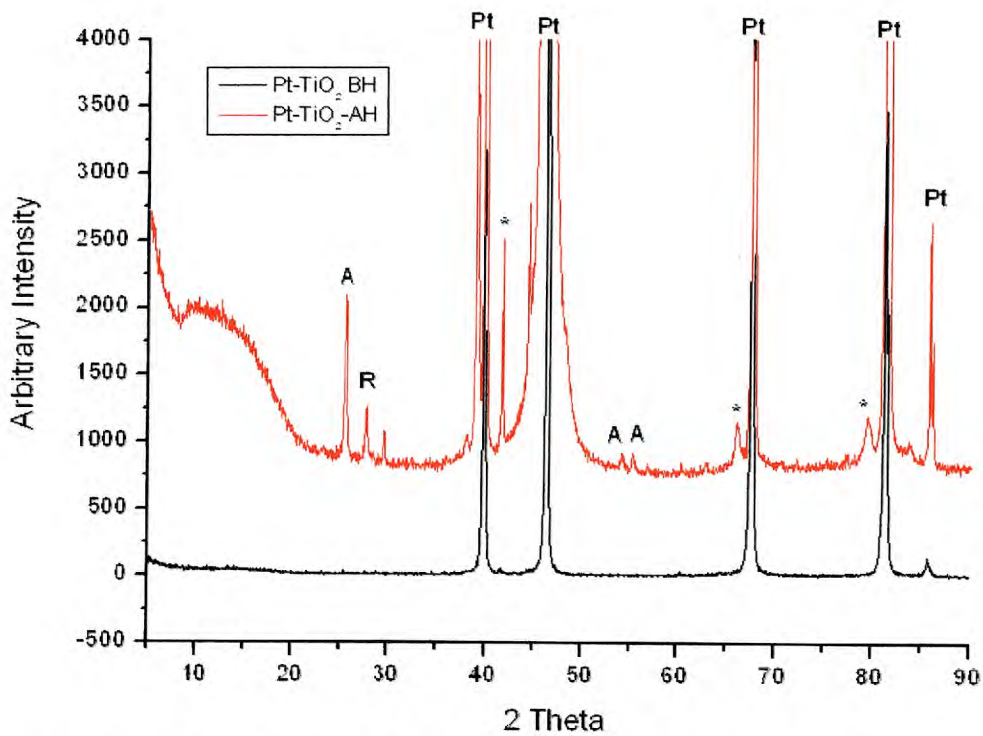


Figure 16 XRD pattern of TiO_2 film deposited on Pt substrate before and after annealing. A: anatase phase; R: rutile phase; Pt: substrate and * is attributed to the peaks which formed because of the tungsten radiation. Black line indicates the as-deposited film; red line indicates annealed film.

It is known that TiO_2 undergoes a phase transformation from the anatase structure to the rutile structure as a function of temperature and in order to further investigate this

process in the deposited thin films, in-situ HTXRD experiments were carried out.

Figure 17 shows the in-situ HTXRD pattern of a TiO_2 film deposited on a Pt substrate and annealed from 100 °C to 1000 °C (since it was not known at which temperature the film will crystallize 100 °C to 1000 °C was chosen to include all the possibilities of crystallization temperature). The scan range is from 24 degrees to 36 degrees 2θ and the heating rate is 60 °C/min. A pattern was recorded every one hundred degrees over this temperature range. Prior to measurement the film was allowed to thermally equilibrate for half an hour. It shows that the as-deposited films were amorphous; when the temperature increased to 400 °C the weak peaks attributable to the anatase phase started to appear indicating crystallization of this polymorph. On further increasing the temperature it appeared that the transition for these electrodeposited films from the anatase phase to the rutile phase begins at ~800 °C, corresponding with the rutile phase. Above this temperature the intensity of the rutile phase increases, whereas the intensity of the anatase decreases indicating a graded transformation of the anatase to rutile polymorph. At 1000 °C the X-ray diffraction pattern shows only rutile peaks. This observation agrees with the literature data for anatase to rutile transformation [133]. As only a short equilibration period was used prior to each scan crystallization of the anatase phase at 400 °C is limited, and hence the intensity of the anatase peak is very low, and considerably broadened. The peak shift to lower values of 2θ during the experiment is due to the thermal expansion of the film, as the d-spacing of lattice increased, and therefore the peak position moves to the left. After cooling the peaks were observed to shift back to higher values of 2θ consistent with the room temperature lattice parameter of the anatase phase.

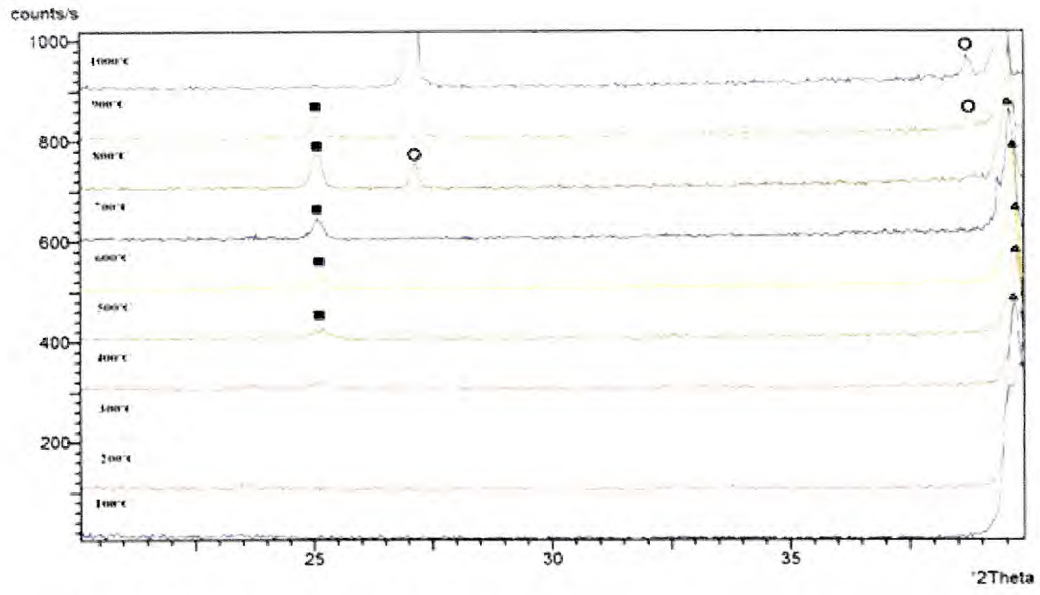


Figure 17 - In-situ XRD patterns of a TiO_2 film deposited on a Pt substrate. Heating was from 100-1000 °C in 100 °C steps (■-anatase, O-rutile, Δ-platinum)

4.2.1.2 Film deposited on Ti substrate

The XRD pattern of the TiO_2 film deposited on a Ti substrate is shown in Figure 18. The scan range is between 20 to 68 degrees 2 theta. As observed with the Pt substrate, the sample deposited on Ti was observed to be amorphous prior to heating. Again, after annealing both anatase and rutile structures were observed. However, the peaks of rutile are more intense than the peaks of anatase and there are more rutile peaks than anatase peaks. This is due to the oxidation of the Ti substrate at 800 °C which forms a stable rutile structure.

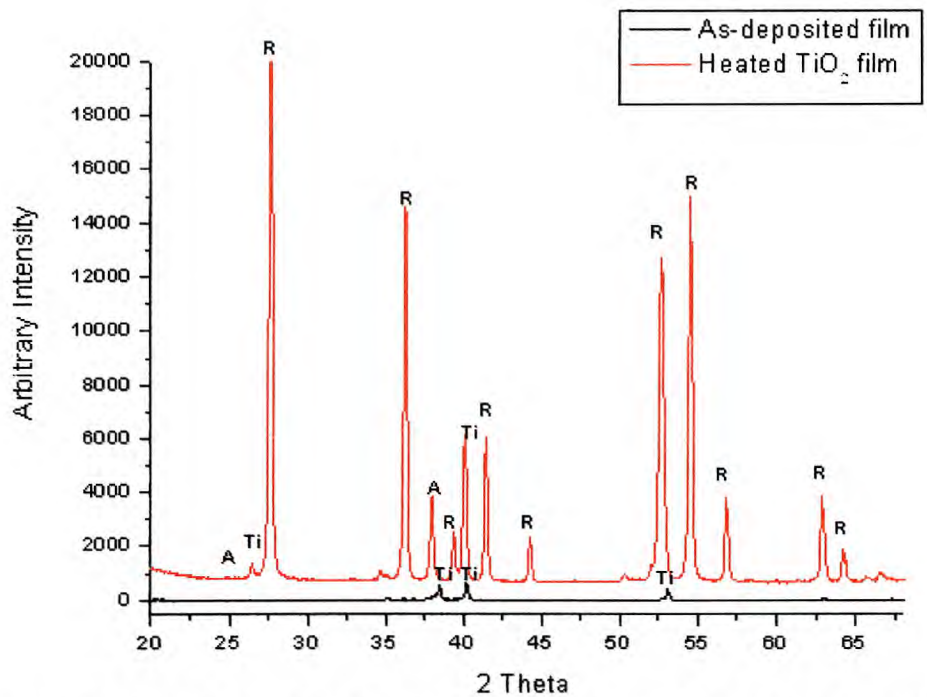


Figure 18 - XRD pattern of a TiO_2 film deposited on a Ti substrate before (black line) and after (red line) annealing. As-deposited film was annealed at 800°C for one hour. Both scans were collected at room temperature. A: anatase phase; R: rutile phase; Ti: substrate.

Compared with the sample deposited on a Pt substrate the sample deposited on the Ti substrate is of better quality; this can be deduced from the following points. First, both before and after annealing the Pt substrate has the highest intensity peeks, with the intensity of both anatase and rutile phases being very weak. For the sample deposited on Ti, after annealing the peaks attributable to the substrate can hardly be seen; the intensity of the rutile phase is very high and secondly the sharp rutile peaks indicate that the film is well crystallized. Third, the arbitrary intensity order of the sample deposited on a Pt substrate and the sample deposited on the Ti substrate are different as well, 10^3 and 10^4 respectively. The reason for this maybe due to the Ti substrate oxidizing when the temperature was above 750 °C influencing the film decomposition characterization during thermal treatment.

Figure 19 shows the in-situ HTXRD patterns of a TiO_2 film deposited on the Ti substrate and annealed from room temperature to 800 °C (as it is known from Figure 17 that at 800 °C film transforms from the anatase phase to the rutile phase, therefore,

all the following samples were annealed to 800 °C). The scan range is from 24 to 37 degrees 2θ and the heating rate is 60 °C/min. The scan program is: scan at room temperature – heat to 400 °C and scan directly – hold at 400 °C for one hour and scan again – heat to 800 °C and scan once – hold at 800 °C for one hour and scan again – cool down to room temperature scan again. Considering the peak shift from 800 °C to room temperature is distinct and this will influence the observation of the entire in-situ XRD pattern, the pattern of the sample after cooling to room temperature is not shown here.

When the temperature reached 400 °C the peak corresponding to the anatase phase appeared and after holding at this temperature for one hour the peak became sharper and narrower which means that the crystallite size is increasing. It could also indicate that there is significant growth in the particle size over this period of time. At this stage peaks attributed to the Ti substrate can still be seen. When the temperature was increased to 800 °C these peaks became weaker and the high intensity rutile peaks appeared. Meanwhile, the intensity of the anatase peak did not decrease much as expected. This information indicates that the Ti substrate was oxidised at high temperature and formed stable rutile phase along with the deposit. After holding at 800 °C for one hour peaks attributed to both anatase and rutile became sharper and the peaks attributed to Ti can hardly be seen. The intensity ratio of rutile and anatase was increased from 2.5 when temperature was 800 °C, to 3.4 when temperature returned to room temperature, this indicates that the film began to transform from the anatase phase to rutile phase.

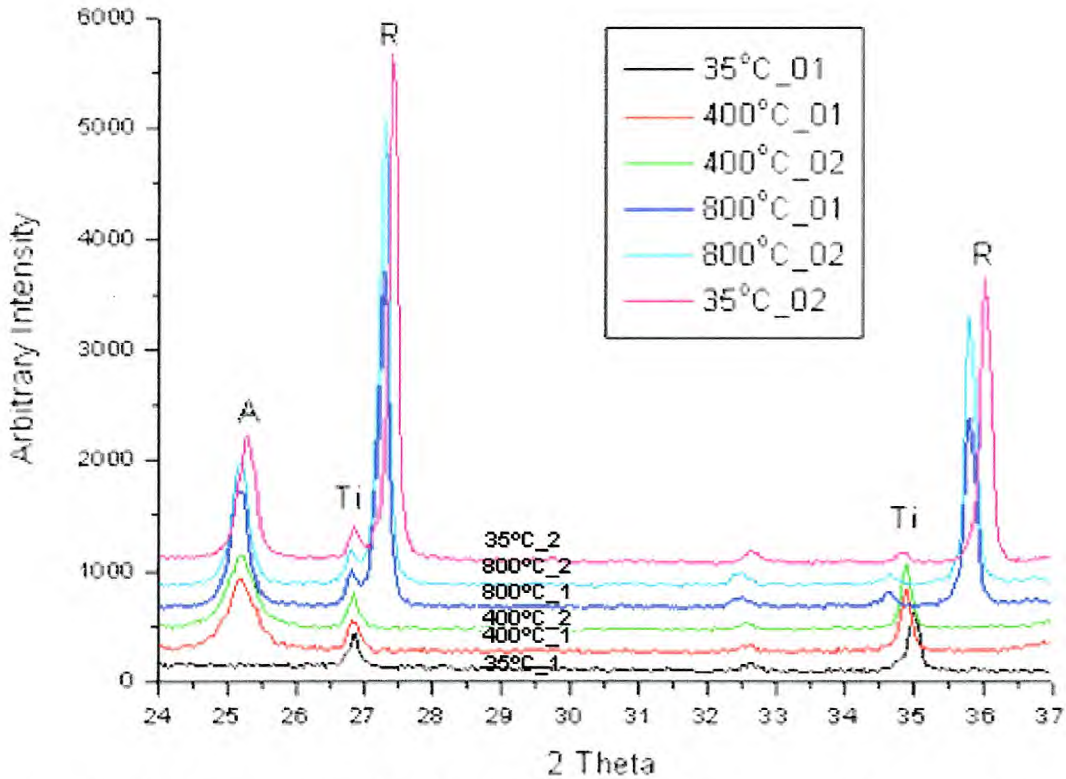


Figure 19 - In-situ XRD pattern of a TiO_2 film deposited on a Ti substrate. 35°C_1 scanned at room temperature; 400 °C_1: scanned first time when temperature was increased to 400 °C; °C_2 scanned second time after temperature was held at 400 °C for one hour; 400 °C_1: scanned first time when temperature increased to 800 °C; °C_2 scanned second time after temperature was held at 800 °C for one hour; 35 °C_2: scanned after temperature was decreased from 800 °C to room temperature

4.2.2 Film Surface Morphology & Grain size

4.2.2.1 Film deposited on Pt substrate

Figure 20 is the SEM surface image of an as-deposited TiO_2 film deposited on a Pt substrate before thermal treatment. After drying in air for approximately 30 minutes the sample surface undergoes a dehydration process forming cracks in the film as shown. Scratches on the substrate caused by the polishing process can easily be seen, indicating that the film is very thin. In general, the film surface is flat and uniform.

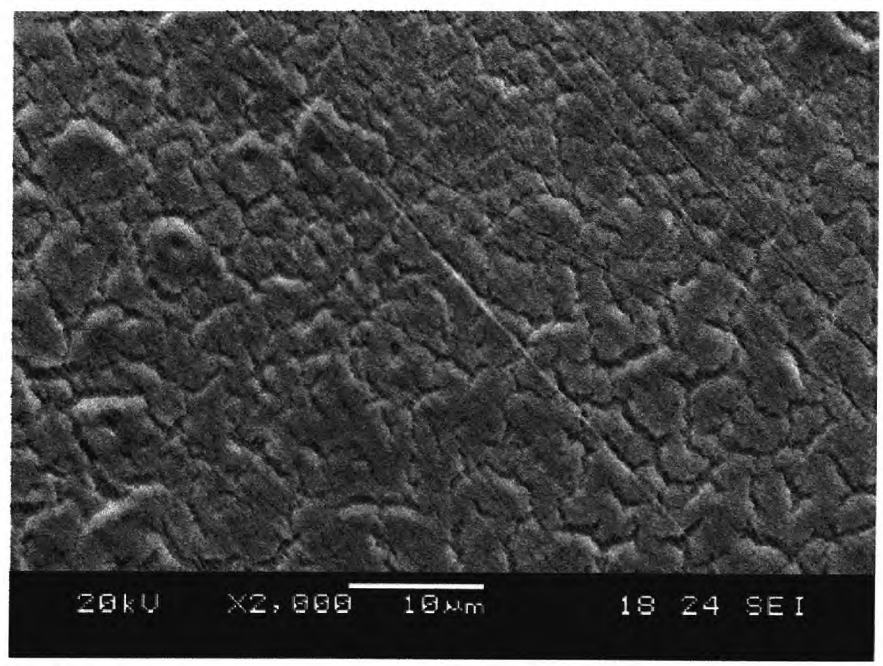
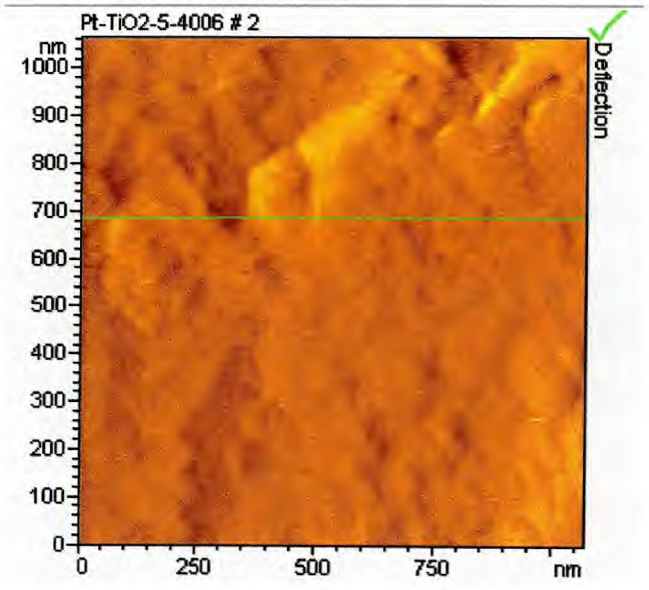


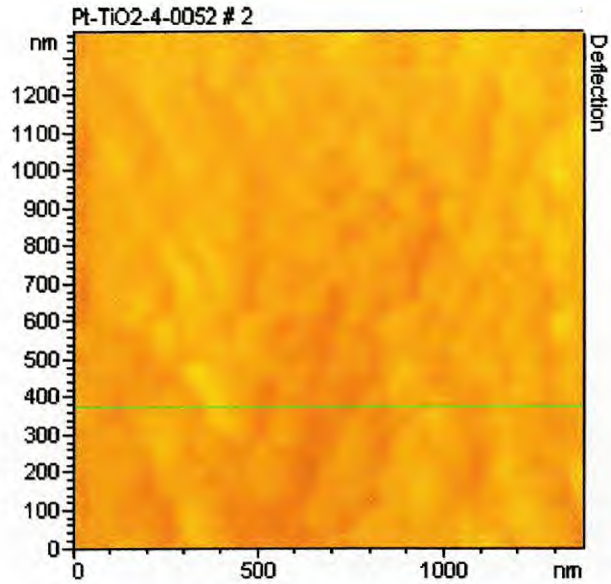
Figure 20 - SEM image of the as-deposited TiO_2 film on a Pt substrate before annealing.

The as-deposited samples were annealed to 800 °C and held at this temperature for one hour. After thermal treatment film changes to thousands of small fragments due to the shrinkage and the poor quality, FEGSEM was fail to take clear image of magnified fragment surface even after gold coated since surface charges a lot, therefore, AFM was used to investigate film topography. Images show the film topography difference from the amorphous to crystalline state and from the anatase

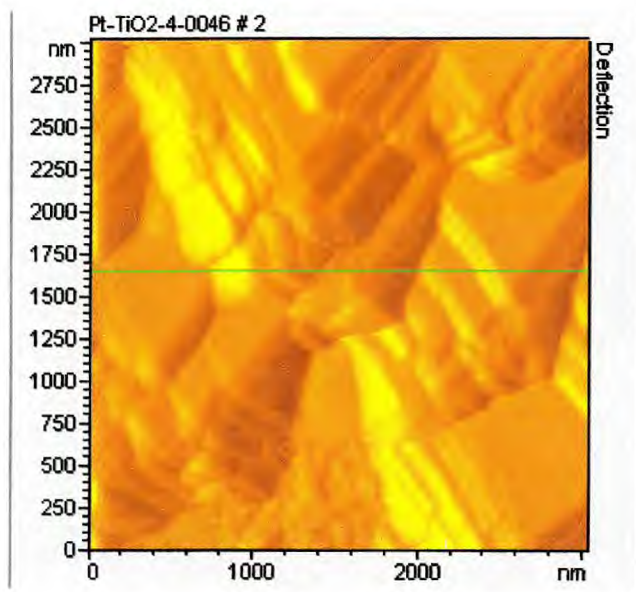
to rutile structure (shown in Figure 21). For films deposited on Pt substrate, the surface of the as-deposited sample is 'fluffy', uneven and no particles were observed (Figure 21 (a)), this is confirmed that the as-deposited film is amorphous. After thermal treatment at 800 °C for one hour the situation has changed with some areas of the film constituted by many small nano-scaled particles as shown in Figure 21 (b), indicating the anatase structure has formed, in good agreement with the results of Hassan *et al.*[134]. In some areas of the film, the same flat terrace-like structure as observed in the FEGSEM images was observed indicating rutile structure formation, Figure 21 (c).



a. Amorphous



b. Anatase structure



c. Rutile structure

Figure 21 - AFM images of film topography of TiO_2 films deposited on Pt substrate, (A) before thermal treatment, (B) after heating at 800 °C for one hour, showing spherical morphology attributed to anatase and (C) after heating at 800 °C for one hour showing well-crystallized terrace-like morphology attributed to rutile phase

4.2.2.2 Film deposited on Ti substrate

An SEM image of an as-deposited film deposited on a Ti substrate is shown in Figure 22. The deposition time for the films deposited on both the Pt and Ti substrates are the same (45 minutes), however, no Ti substrate scratches were observed from Figure 22 as in Figure 20, suggests that film is thick enough to cover the substrate without showing scratches. Cracks can still be seen but not all over the surface. The color difference of the image indicates that the film surface is not flat.

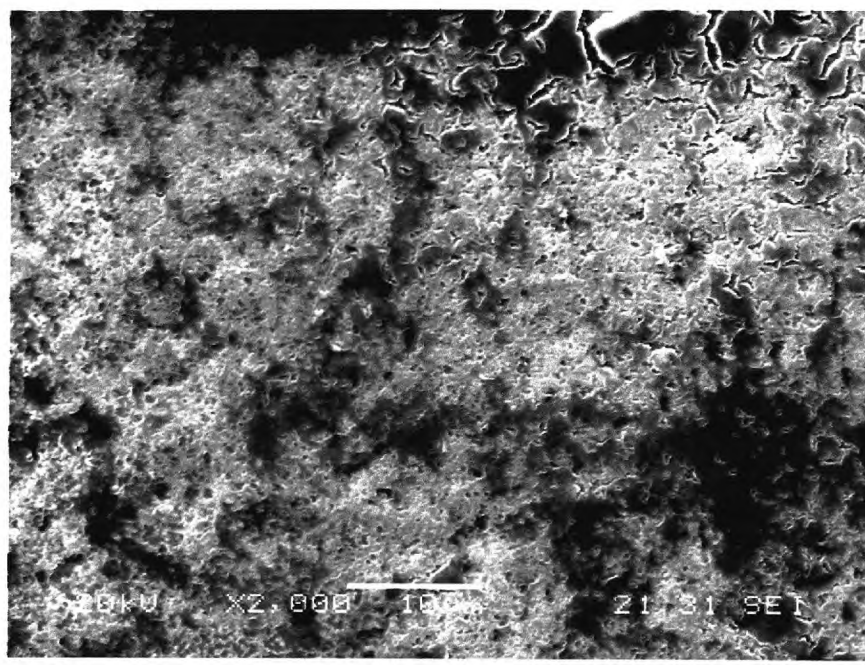


Figure 22 - SEM image of the as-deposited TiO_2 film on a Ti substrate before annealing.

Several methods were used to minimize the film cracking. For example, considering that the cracks may be due to the slow spontaneous drying process in air, samples were dried by blowing nitrogen gas over the film immediately after removal from the solution; thermal expansion of the Ti substrate during the temperature change between 0 °C in the solution and room temperature was also taken in to account. In order to avoid cracking as a result of thermal expansion mismatch between the substrate and the film the as-deposited sample was placed in 0 °C deionized water immediately and was not removal until the temperature of the water had gradually

increased to room temperature. These precautions did not affect the level of cracking observed. Therefore, the reason for the film cracking is not due to the substrate used but is a feature of the deposit itself. The problem of film cracking has not been resolved.

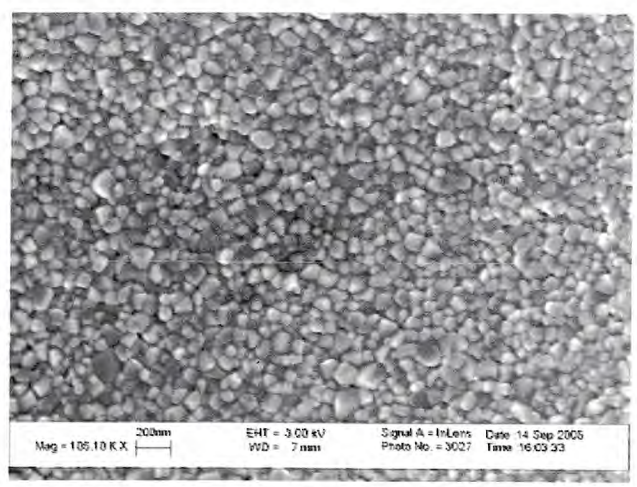
The as-deposited samples were annealed to 800 °C and held at this temperature for one hour. At low magnification (<5,000) there is no obvious film topography change after thermal treatment; however, as mentioned before, the film is crystalline after annealing. The quality of the film is improved; therefore, FEGSEM was used to observe the film surface at the nano scale to investigate the film crystallization process.

Figure 23 shows FEGSEM images of a TiO_2 film deposited on a Ti substrate after annealing at 800 °C in air for one hour. It can be seen that the result is the same as film deposited on Pt substrate (AFM images, Figure 21 b, c) which can help distinguish which part is deposited film and which part is oxidized substrate. Film actually has two morphologies in different areas. The uniform spherical-shape particles as shown in Figure 23 (a), the size is approximately between 36 ± 18 nm, the same shape also shown in Figure 21 b. And the terrace-like structure as shown in Figure 22 (b), the size of it is approximately 80 ± 31 nm, the same shape shown in Figure 21c.

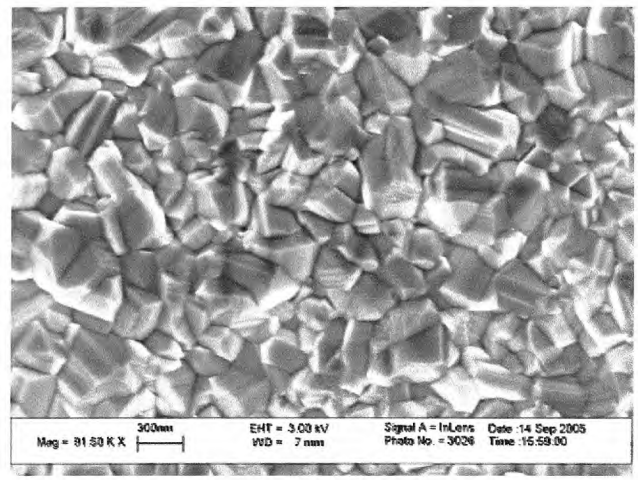
For samples annealed at 1000 °C for one hour, no spherical particles were observed which indicates that the spherical structure is instead the anatase phase; Kim *et. al* and Kholmanov *et. al* also confirmed this structure [76, 135]; whereas the terrace-like structure is the rutile structure. The rutile structure observed is the same as that observed by Leyens *et. al* [136]. This result is in line with the XRD result that the peaks corresponding to the rutile phase are of greater intensity than the peaks corresponding to the anatase phase. In general the spherical particle sizes are uniform; if the temperature increases the spherical particles will grow and transform to the

terrace-like rutile structure. The terrace-like structured film looks compact when compared with the spherical particle structured film.

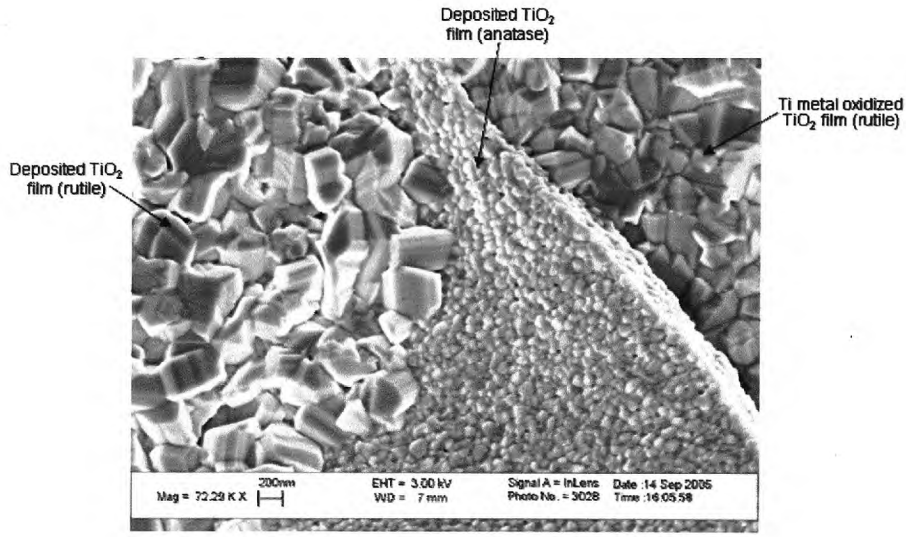
After annealing most of the film consists of the terrace-like structures rather than spherical particles, whilst there are some areas where both structures are present as shown in Figure 23 (c). The middle area is deposited TiO_2 with anatase phase, with the film thickness of approximately 200 nm, some part of the film is detached from the substrate; the right corner of the image is the oxidized Ti substrate. As it can be seen that it is under the detached TiO_2 film of anatase phase, since Ti metal oxidize when temperature above 800 °C, only rutile phase can be observed for oxidized Ti. For the left part of the image it looks like the terrace-like structure is growing on the spherical structure indicating film transferring from spherical particles to terrace-like structure. Therefore, the left corner is deposited TiO_2 film. Therefore, for the film that adheres well on the substrate the morphology of the film is growing influenced by the oxidized Ti substrate, whereas, for the film that detached from the substrate the morphology of the film because of the shrinkage is not influenced by the oxidized Ti substrate.



a.



b.



c.

Figure 23 - FEGSEM images of a TiO_2 film deposited on a Ti substrate after annealing at 800 °C in air for one hour. (a): spherical morphology, (b): terrace-like morphology. (c): mixed morphology

In general, even though the TiO_2 films are deposited on different substrates, the topographies of the film surface are the same; in both cases anatase and rutile phases are observed after annealing at 800 °C for one hour.

Figure 24 shows the image of two small film fragments highlighting a crack in the film. The deposited film is of the anatase structure, whereas, Ti metal thermally grown TiO_2 is of the rutile structure. It is clear from this image that the Ti substrate is effectively 'growing up' to fill the gap between the two fragments, meaning that

during thermal treatment at 800 °C the oxidation of the Ti substrate occurs mainly by diffusion of Ti rather than oxygen through the growing oxide layer. This observation agrees with references [137, 138]. At the edge of the fragment the film is relatively thin, therefore, the thermally oxidized Ti metal 'growing over' the deposited film. It should be remembered that the thickness of the thermally grown TiO_2 depends on the annealing temperature, the annealing time and the oxygen content. Kofstad *et al.* [139] estimated that the diffusion coefficient of oxygen, D, in the alpha-Ti (normally titanium has alpha phase, when the temperature above 882.5 °C it will transfer to beta phase [140]) can be calculated using the equation below:

$$D = 50 \exp(-2{,}412{,}000/(RT)) \qquad 4.2$$

Where 2,412,000 J/mol is the activation energy for the diffusion of oxygen in alpha-Ti; 'R' is gas constant, 8.314 J· $mole^{-1}$ · deg K^{-1}; 'T' is temperature, K. Therefore, at the annealing temperature of 800 °C the diffusion coefficient of oxygen is 9.695 x 10^{-11} cm^2s^{-1}. After annealed at 800 °C for one hour the calculated thickness of the oxide layer is 5.908 μm. Since the deposited film is on top of the Ti substrate therefore, the thickness of the oxide layer will be thinner than calculated data.

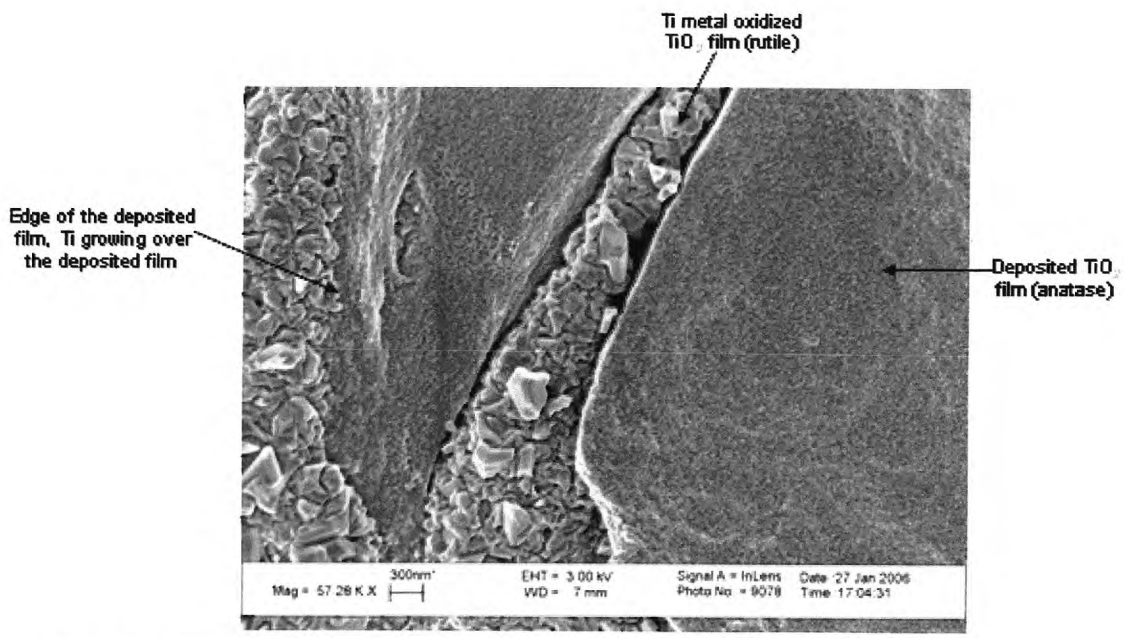


Figure 24 - FEGSEM images of cracks in the TiO_2 film deposited on a Ti substrate after annealing at 800 °C in air for one hour.

The reason for using Ti as a substrate, even though it will oxidize to form TiO_2 itself during high temperature annealing is because the deposit quality (such as adhesion, cracks) was poor when Pt was used as a substrate maybe due to the weak bonding capability between the film and substrate. Considering that the native thin TiO_2 layer on Ti can first reduce the lattice mismatch, which probably improves film properties, and second, the thin TiO_2 layer can be used as 'seed layer' for nucleation. Park *et al.* [141] also used ZnO thin layer as buffer layer to produce ZnO films. The results shows that films deposited on a Ti substrate do have better quality and its oxidation behavior can be controlled by careful change of annealing atmosphere and temperature.

4.2.2.3 EDS Analysis

Energy dispersive X-ray analysis was used to determine the elemental content of the films. Several points on the sample surface were taken to measure the elemental content in order to get the average data. An EDS spectrum of a TiO_2 sample deposited on a Ti substrate is shown in Figure 25. From this data it is clear that, the film is pure with only Ti and O observed; the atomic percentage for Ti and O on average is 33.32% and 66.64% respectively. This corresponds well with the nominal stoichiometry of the film. The maximum penetration depth of the EDS instrument is up to 2 μm depending on the materials, therefore, the EDS data of the film deposited on Ti substrate is not influenced by the substrate, as the film thickness is > 2μm. For samples deposited on the Pt substrate the atomic percentages were the same.

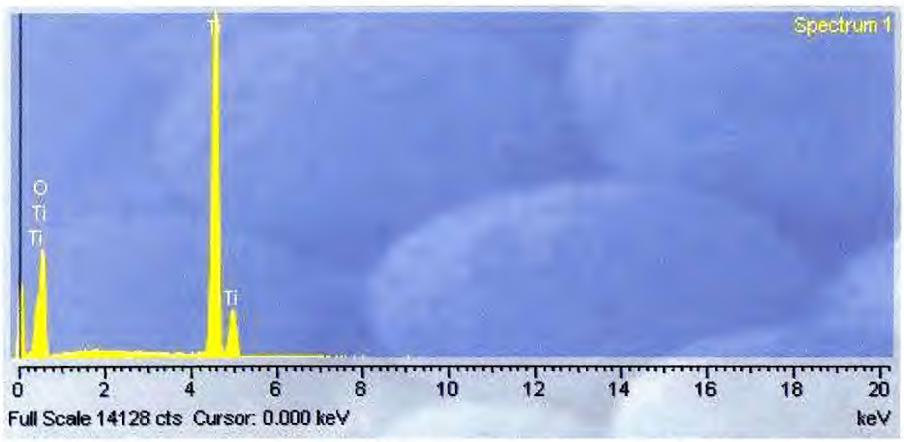


Figure 25 - EDS image of TiO_2 film deposited on Ti substrate after annealing.

4.2.2.4 Particle Size

From the AFM image (Figure 26) of the annealed film it is clear that the same rutile structure as was observed with the FEGSEM is also observed. From this image and Figure 23 (b) the particle size of the rutile particles in the film can be estimated to be between 50 nm to 120 nm; the anatase particle size is between 30 nm to 60 nm (Figure 23 (a)).

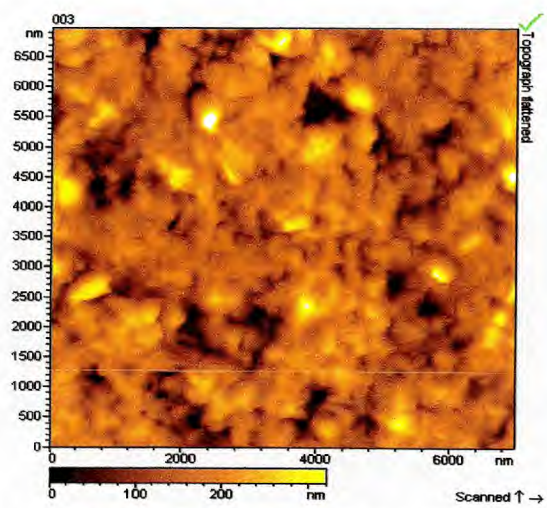


Figure 26 - AFM image of a TiO_2 film deposited on a Ti substrate after annealing at 800 °C for one hour in air

In order to confirm these particle sizes, the Scherrer equation [121] was used to calculate the grain size from the XRD data (equation 3.8).

$$t = \frac{0.9\lambda}{B \cdot Cos\theta} \qquad 3.8$$

Where t is particle size, λ is the wavelength of Cu K_α; B is FWHM (full width at half maximum) of the broadened diffraction line on the 2θ scale (radians) which can be observed from the XRD data. Note: B is corrected for instrumental broadening, B_{inst}, using equation 4.3 [121] where B_{exp} is the experimentally measured FWHM, B_{inst} is the FWHM due to the instrument. The result of this calculation is listed in Table 1 and shows good agreement with the FEGSEM and AFM data.

$$B^2 = B_{exp}^2 - B_{inst}^2 \qquad 4.3$$

Table 1 - Particle sizes and XRD parameters of deposited TiO_2 film.

	2θ	d ([Å])	FWHM	t (nm)	AFM/SEM(nm)
Anatase (101)	25.27	3.527	0.281 ± 0.008	34 ± 1	36 ± 18
Rutile (110)	27.38	3.258	0.158 ± 0.004	115 ± 12	80 ± 31
Rutile (101)	36.02	2.495	0.169 ± 0.002	89 ± 4	

4.2.3 Film Thickness

In order to measure the thickness of the films and to gain insight into the film growth mechanism, focused ion beam (FIB) milling was used to create a 38° ramp on the film surface. As mentioned in chapter 3.3.4, the reason for making a ramp is because it is easier to observe the sample from the surface to the bottom of the film, and since the ramp efficiently 'stretches' the thickness observed, it is easier for SEM observation of the film interface.

The size of the ramp is about 3 μm x 4μm and the beam was sputtered from the surface to the Ti metal substrate. A layer of gold was deposited on the film to increase the conductivity of the sample. As shown in Figure 27, it is clear that the sample has three layers; from the top of the image to bottom there is the dark layer which is Ti metal, a middle layer which is the interface (titanium oxide layer which is caused by substrate oxidation with a thickness of about 0.55±0.04 μm) and the 2.71±0.09μm deposited thick film layer. It should be mentioned that as the ramp is taken at 38° the actual thickness of the film shown here is obtained by multiplying the measured thickness by tan 38° (explained in chapter 3.3.4, FIB section). Micro porosity was found at both the top and bottom of the thick TiO_2 film layer. The porosity in the bottom is due to Ti and oxygen transfer during high temperature annealing and the porosity in the top is due to film surface dehydration. The centre of the deposited film is relatively compact.

For the samples deposited on a Pt substrate, since the film quality is poor and films are composed of thousands of fragments, it is difficult to create a ramp, and therefore, no measurement was performed for these samples. However, from some of the SEM images of these samples an estimate of the film thickness can be made and for these films a range of < 1μm was determined.

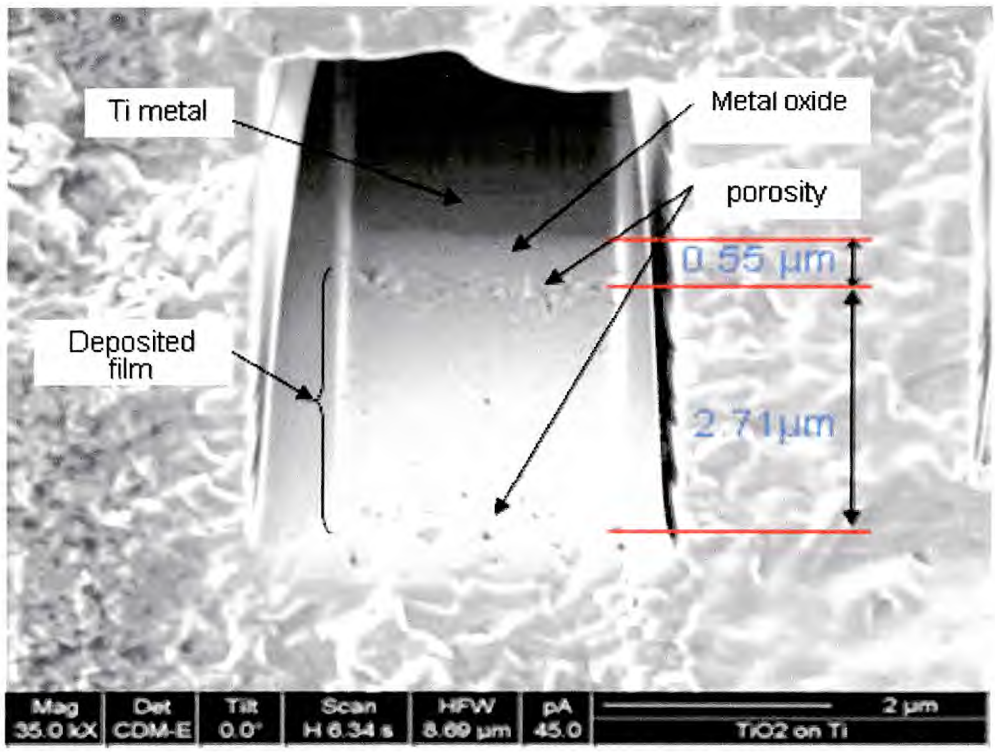


Figure 27 - FIB image of a annealed TiO_2 film deposited on a Ti substrate. A 38° ramp has been created allowing the substrate, interface and film to be observed.

4.3 Influence of Electrodeposition Parameters on Film Quality

As mentioned in chapter 2 one of the advantages of cathodic electrodeposition is that it is relatively easy to control the film thickness and weight via adjustment of these parameters, such as, deposition time and current density *etc.* In this chapter, parameters as well as annealing temperature are investigated to determine the impact of the electrodeposition parameters on the film characteristics.

4.3.1 Current Density

Initially the applied current density for deposition was 20 $mA \cdot cm^{-2}$. In this section the applied current was varied with samples being deposited at 30 $mA \cdot cm^{-2}$, 20 $mA \cdot cm^{-2}$, 10 $mA \cdot cm^{-2}$ and 5 $mA \cdot cm^{-2}$ respectively. All other parameters were maintained the same. Table 2 lists the start and end potential of the samples deposited under different currents. It can be seen that the initial potential of the four samples are different. This is because at the very beginning, the R_d in equation 4.1 is zero, the cathodic substrate is conductive and the whole surface is covered by OH^-, therefore, the deposition rate at this stage is very high, which induces an insulating layer to form quickly, also R_d increases rapidly [101]. The situation described above takes place within seconds, therefore, it is difficult to record precisely the initial potential. The end potentials for these samples are very similar, due to no further OH^- being provided so the film growth tends to saturate.

Table 2 - Parameters of samples deposited under different current densities

Current density ($mA \cdot cm^{-2}$)	Start Potential (V)	End potential (V)	Deposition Time (minutes)	Film thickness (μm)
-30	6.44	10.79	45	2.79±0.38
-20	5.36	11.03	45	2.93±0.29
-10	3.84	11.01	45	1.27±0.25
-5	2.90	10.96	45	1.45±0.16

Figure 28 shows the SEM images of TiO_2 films electrodeposited on a Ti substrate under different applied currents. In Figure 28 (a) it is clear that, the sample deposited under high current has pores all over the surface. This is due to that at the higher current there is more rapid nucleation of the film so it is easier to get more fragments, whereas, the lower current will allow slower growth and therefore better crystals. From Figure 28 (c) and (d), it is clear that films deposited at low currents are more uniform; however, the problem of cracking is still serious due to shrinkage during drying process. In general, compare with Figure 28 (a), (c) and (d), Figure 28 (b) is more uniform has less cracks and less porosity, this indicate that current of 20 $mA \cdot cm^{-2}$ is suitable for deposit TiO_2 films. Film thicknesses were measured (Table 2), for film deposited at 30 $mA \cdot cm^{-2}$ due to the porous surface the thickness is different in different area; film deposited at 20 $mA \cdot cm^{-2}$ is thicker than films deposited at 10 and 5 $mA \cdot cm^{-2}$. The data also confirmed that film deposited at low current has uniform thickness.

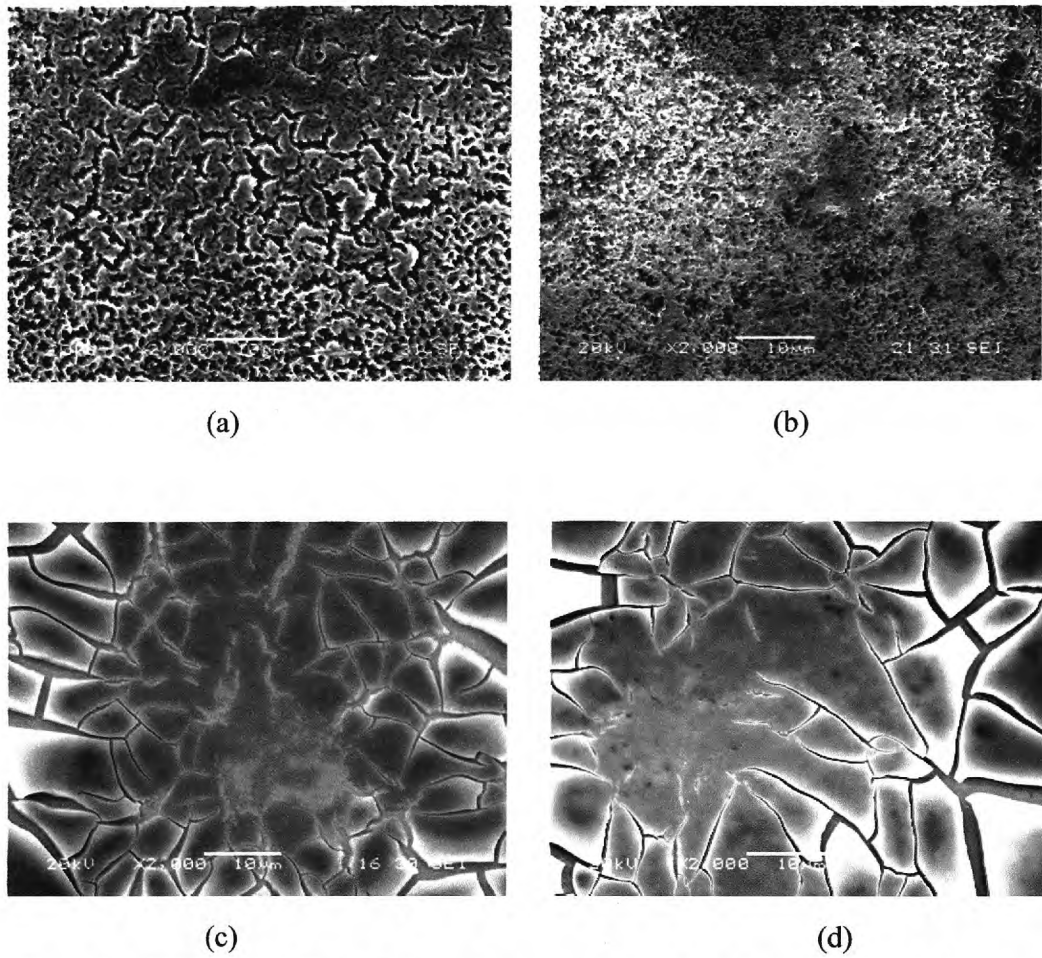


Figure 28 - SEM images of TiO_2/Ti films electrodeposited under different currents before heat treatment. (a): 30 mA·cm^{-2}, (b): 20 mA·cm^{-2}, (c): 10 mA·cm^{-2}, (d): 5 mA·cm^{-2} respectively.

The XRD patterns of post annealed TiO_2 films deposited on Ti substrate at different current densities (30 mA·cm^{-2}, 20 mA·cm^{-2}, 10 mA·cm^{-2}, and 5 mA·cm^{-2} respectively) are shown in Figure 29. As can be seen from the Figure, the XRD patterns of samples deposited at 20, 10 and 5 mA·cm^{-2} are similar, however, the global intensities are decreased in this order. Both anatase and rutile phases were observed, since the Ti substrate was oxidized during thermal treatment and forms rutile directly, the intensity of rutile is higher than the intensity of anatase. The peaks attributed to the Ti substrate can still be observed, this means Ti was not completely oxidized.

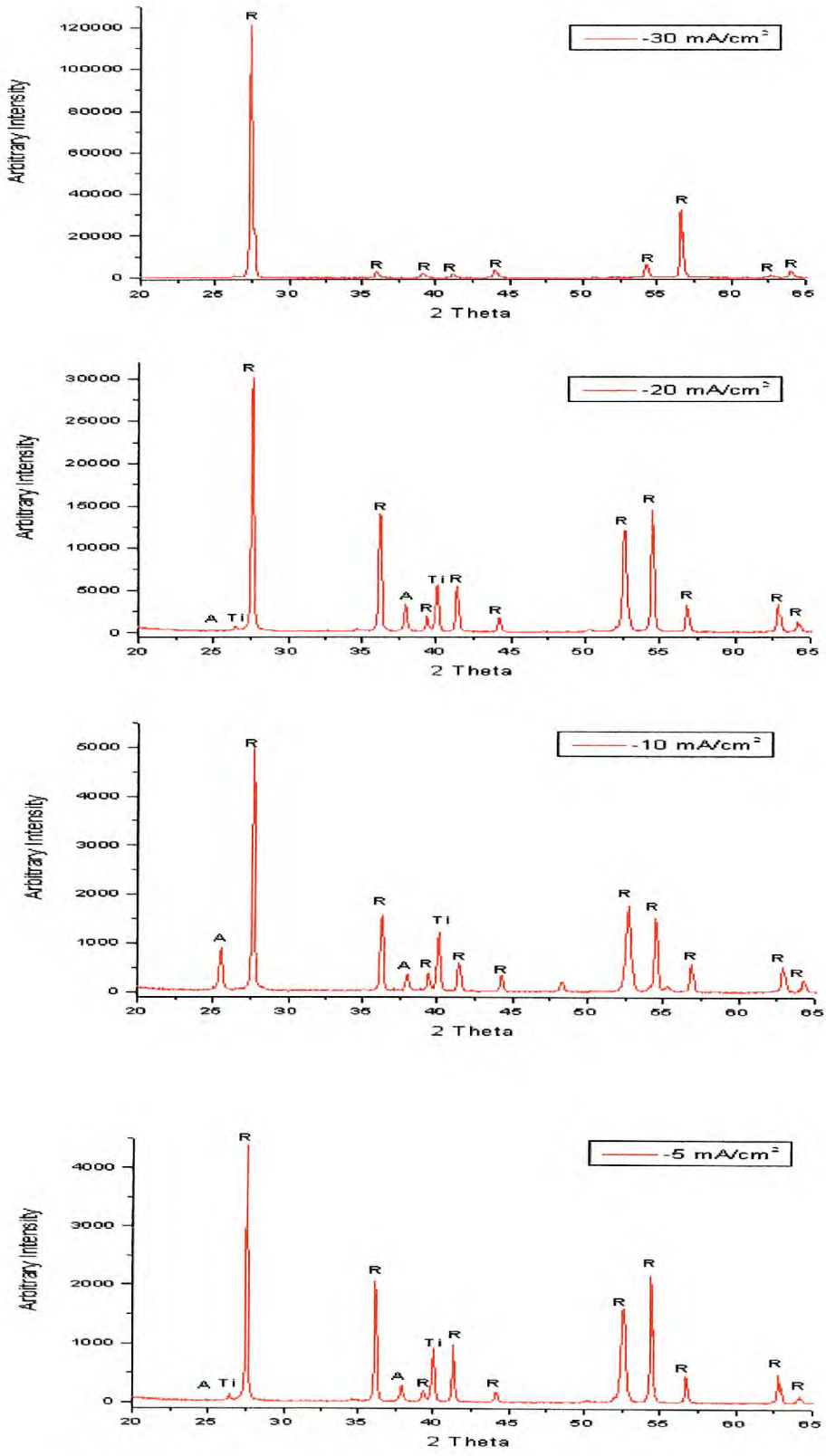


Figure 29 - XRD patterns of TiO_2/Ti samples deposited at different currents, after heat treatment at 800 °C for one hour.

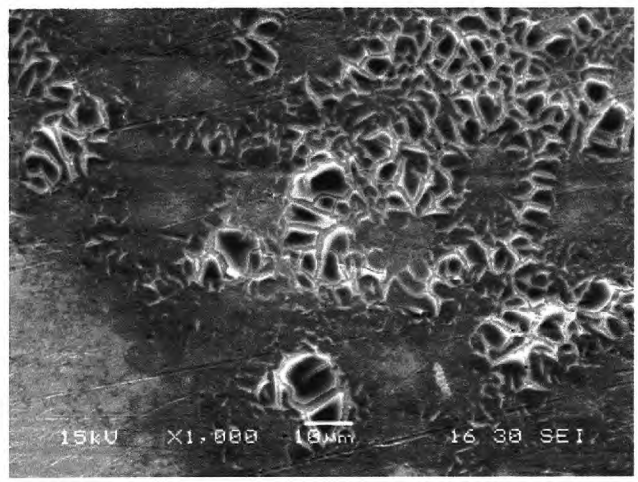
For films deposited at 30 $mA \cdot cm^{-2}$ the XRD pattern is different, first of all the intensity of the film is several times higher than the intensities of other samples, second, only rutile phase, no peaks corresponding to anatase or Ti substrate were observed, and third, the intensities of rutile peak at 2 theta ~ 27.5° (rutile (110) plane) is much higher than the other rutile peaks. One of the possible explanations for these differences maybe that the film deposited at high current has pores on the film surface and therefore, it is much easier for the Ti substrate to react with oxygen in air, and Ti substrate oxidized to form rutile completely. As mentioned in chapter 1, rutile (110) is the most stable orientation, so when Ti metal reacts with oxygen it grows towards rutile (110) plane.

There are some orientation differences were observed for film deposited at 10 $mA \cdot cm^{-2}$. For films deposited at other currents anatase peaks at ~ 38° have relatively high intensity, however, for film deposited at 10 $mA \cdot cm^{-2}$ anatase peaks at 25 have high relative intensity. The reason for this is not clear yet, will be studied in the future work.

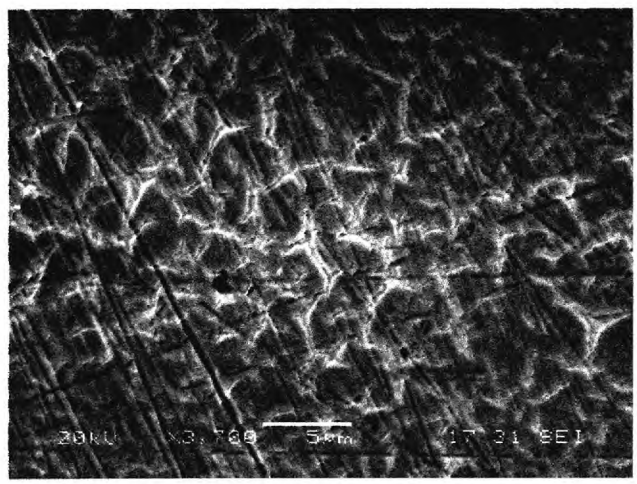
Comparing these four SEM images and XRD patterns; it can be concluded that films deposited at 20 $mA \cdot cm^{-2}$ film have relatively flat surface with lower porosity, and therefore, 20 $mA \cdot cm^{-2}$ is the optimal deposit current density in this research.

4.3.2 Effect of Deposition Time

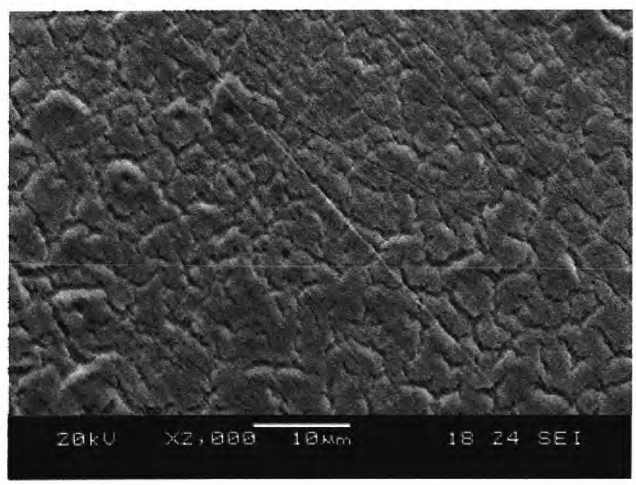
For TiO_2 films deposited on a Pt substrate, various deposition times were used to determine the influence of time on the film characteristics. Figure 30 shows the SEM images of TiO_2/Pt films deposited under various deposition times before heat treatment. The current density employed was 20 $mA \cdot cm^{-2}$ for all samples.



a



b



c

Figure 30 - SEM images of TiO_2/Pt films deposited for (a) 15 mins, (b) 30 minutes, and (c) 45 minutes before heat treatment. The current density was 20mA·cm^{-2} for all samples.

For the sample deposited for 15 mins, Figure 30 (a), the film did not cover the whole substrate and, except for some large fragments, the film was found to be very thin with the scratches of the substrate clearly visible. For the sample deposited for 30 mins, Figure 30 (b), even though the scratches of the substrate can still be seen, the film is relatively uniform, dense and the thickness is even. After a deposition time of 45 mins Figure 30 (c), the situation is even better with the deposit being more uniform with even adhesion and a continuous film. In general, the film is much more homogenous rather than consisting of split fragments. This result indicates that the film quality is improved as deposition time increases. However, if the film thickness reaches a maximum because of the deposit resistivity increasing the deposition time further will have no influence on the film characteristics.

4.3.3 Variation of the Annealing Temperature

As described in section 4.2.1, for samples deposited on a Pt substrate, annealing from room temperature to 1000 °C the film changes from an amorphous phase to the anatase polymorph, mixed anatase and rutile phases and finally the rutile polymorph. For samples deposited on a Ti substrate, since the substrate will oxidise during high temperature annealing, and therefore it may stick on to the in-situ XRD heating platinum strip, so in-situ XRD only shows sample heated from room temperature to 800 °C. As the temperature increased, the evolution of the phases was the same as previously observed with the film deposited on the Pt substrates.

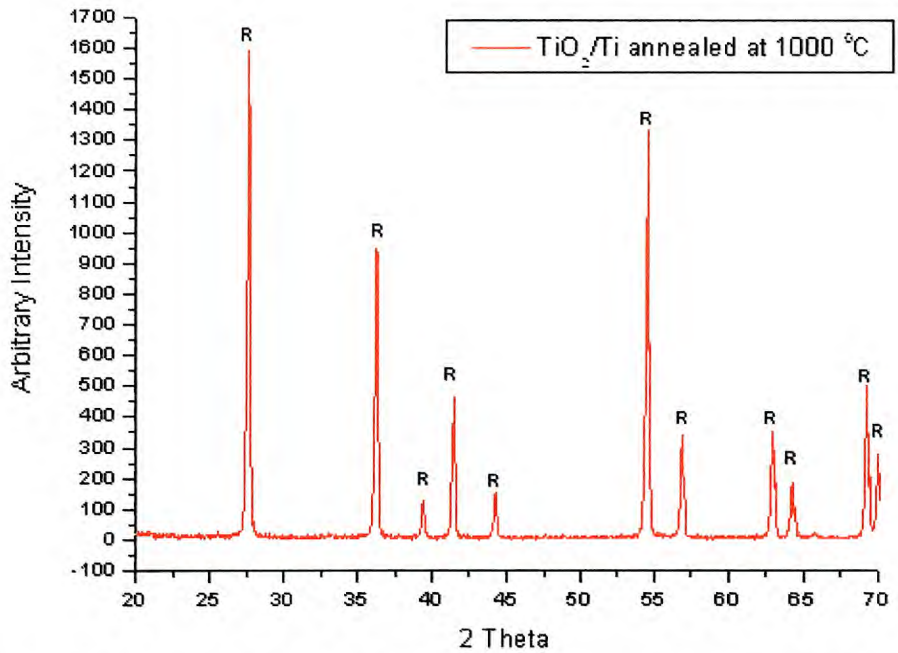


Figure 31 - XRD pattern of a TiO_2 film deposited on a Ti substrate annealed at 1000 °C and held for one hour. "R" indicates the rutile phase

Samples deposited on a Ti substrate and annealed at 1000 °C directly were analyzed by XRD and the result is shown in Figure 31. It is clear that, after annealing at 1000 °C for one hour only peaks corresponding to the rutile phase were observed which means that either the deposited film is too thick to detect the substrate or a certain thickness of the Ti substrate has been oxidized. In order to confirm this point the penetration depth was calculated for both the anatase and rutile phases using equation 3.7 from chapter 3 [121]:

$$I_x = I_0 e^{-(\frac{\mu}{\rho})\rho x} \qquad 3.7$$

Where I_0 is original intensity, I_x is the transmitted intensity, the quantity μ/ρ is a constant of the materials (mass absorption coefficient), and ρ is the theoretical density. For the rutile phase $\rho = 4.25$ g/cm^3. The penetration depth, x, is the distance that x-rays can penetrate through the sample; to obtain the real thickness, t , scan angle $\sin\theta$ has to be included as illustrated in Figure 32. According to equation 3.7, it

is calculated, that 90% intensity is absorbed, for 2θ between 20° and 90° the penetration depth for rutile is between 4μm and 15μm. The deposited film thickness (film annealed at 800 °C) determined from the FIB measurement is ~2.71 μm. Therefore, it is not likely that the deposited film is too thick to detect peaks which are attributable to the Ti substrate. This means that the thickness of several microns of Ti substrate was oxidized.

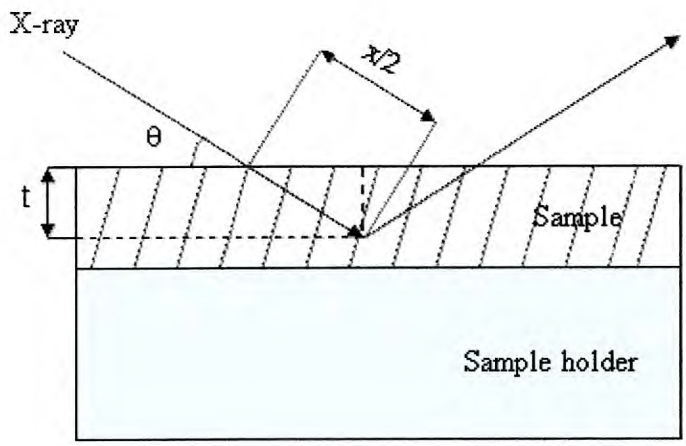


Figure 32 - A schematic diagram for the determination of the X-ray penetration depth of the sample.

Figure 33 is a phase diagram of the titanium – oxygen system; it can be seen that at ~ 885 °C titanium starts to transform from the alpha to the beta polymorph. The structure changes from a hexagonal closed-packed (hcp) structure to a body-centered-cubic (bcc) structure [142]. It is known that the rate of diffusion of oxygen in beta titanium at 1000°C is 2.28 x 10^{-8} cm^2s^{-1}, it is much higher than alpha titanium [137, 143], therefore, for film annealed at 1000 °C for one hour the calculated diffusion length is 90.058 μm. Even though Ti substrate is covered with deposited film, it is reasonable that thickness up to several microns of titanium is oxidized.

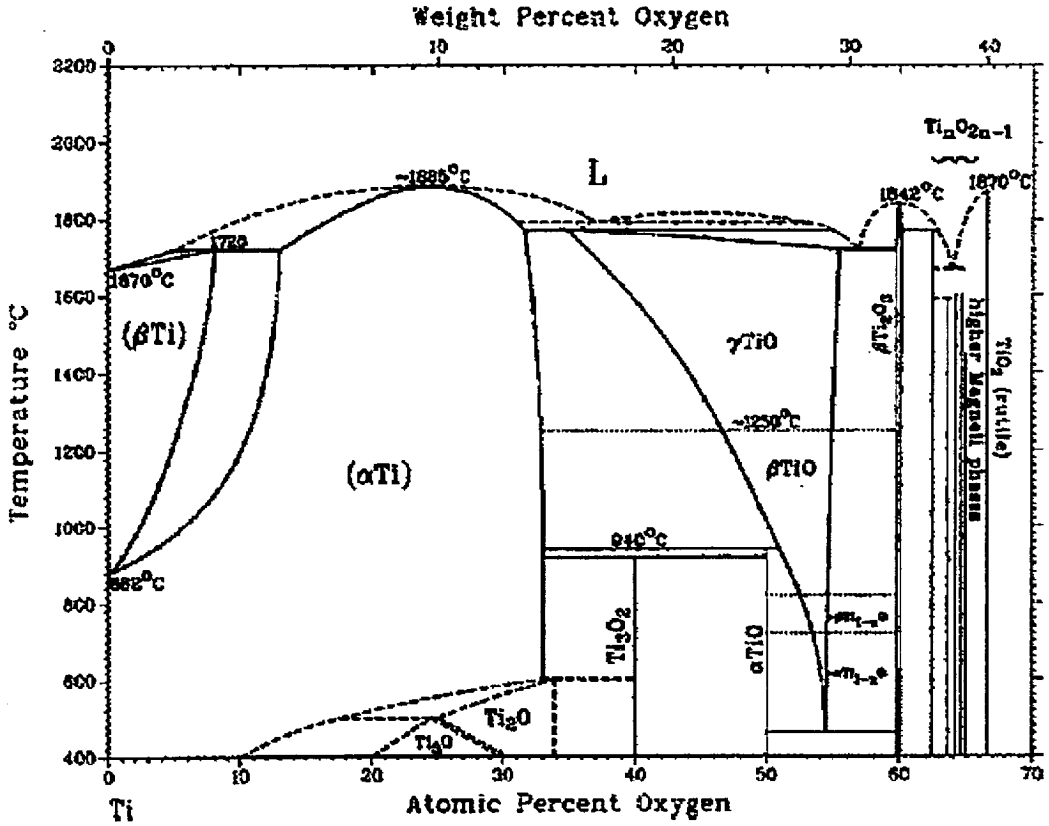


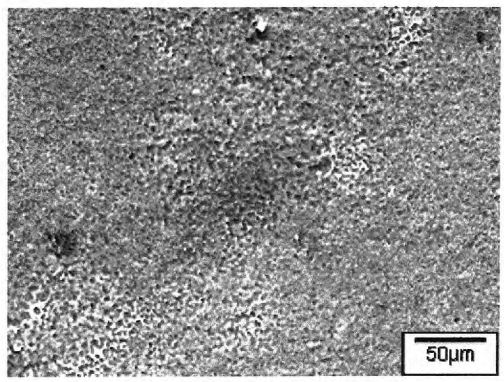
Figure 33 Phase diagram of titanium – oxygen system [144]

4.4 Effect of Annealing Atmosphere on Film Morphology

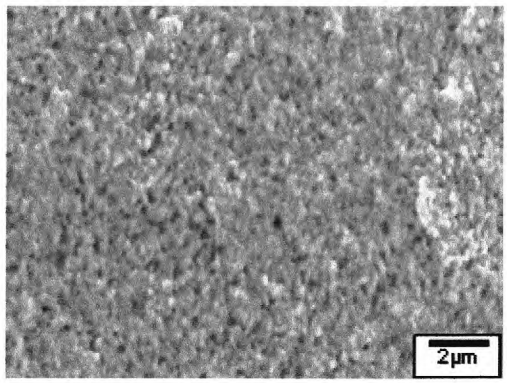
In this section, the as-deposited TiO_2 films which were deposited on a Ti substrate were annealed in different atmospheres: air, argon and mixed argon and hydrogen (10% hydrogen) respectively, in order to investigate the influence of the annealing atmosphere on the film characteristics.

4.4.1 Impact on Film Surface Morphology

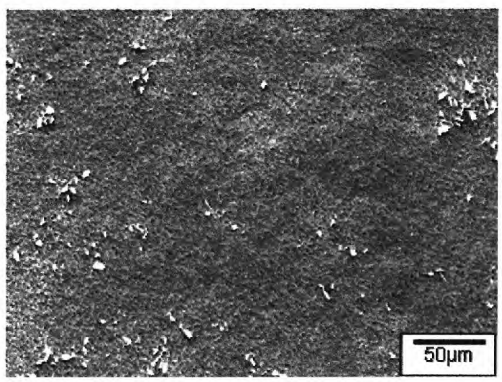
The SEM images of TiO_2 films deposited on Ti substrates thermally treated in air (a, b), argon (c, d) and mixed argon and hydrogen (10% hydrogen, e, f) at 800 °C for one hour respectively are shown in Figure 34. It is noted that, at low magnification (a, c, and e, x 500), there is no obvious difference in the film topography and the film surfaces are dense and uniform. On increasing the magnification (b, d, and f, x 8,000), there are clear differences in the film topographies. For the sample annealed in air, the crystallite size is relatively small (~50 nm); grain size was found to increase from the sample annealed in air to the sample annealed in Ar/H_2. The grain size of samples annealed in Ar (~100 nm) and Ar/H_2 (~120 nm) are several times larger than samples annealed in air. Each film appears homogeneous.



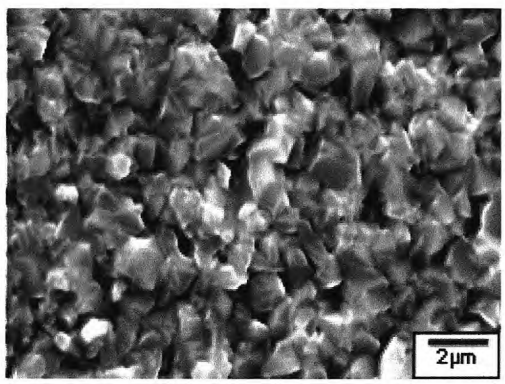
a. Annealed in Air x 500



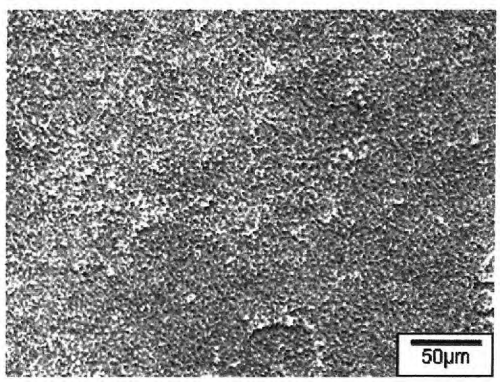
b. Annealed in Air x 8,000



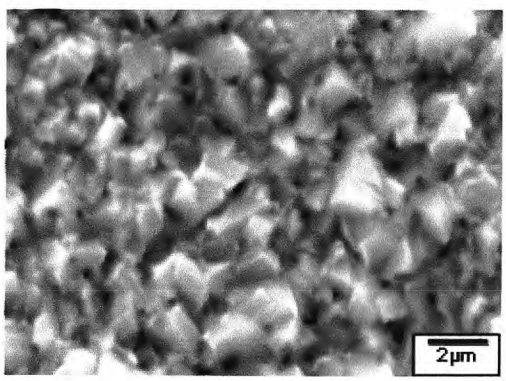
c. Annealed in Ar x 500



d. Annealed in Ar x 8,000

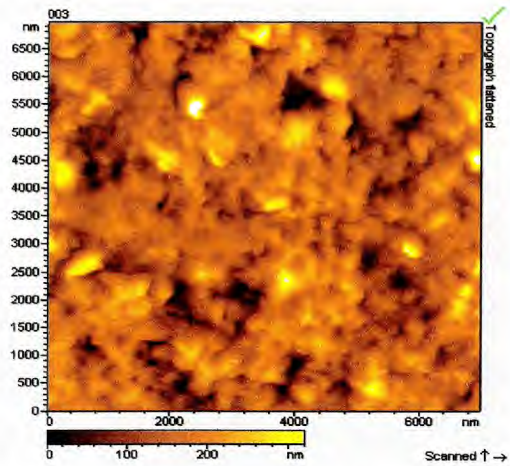


e. Annealed in Ar/H_2 x 500

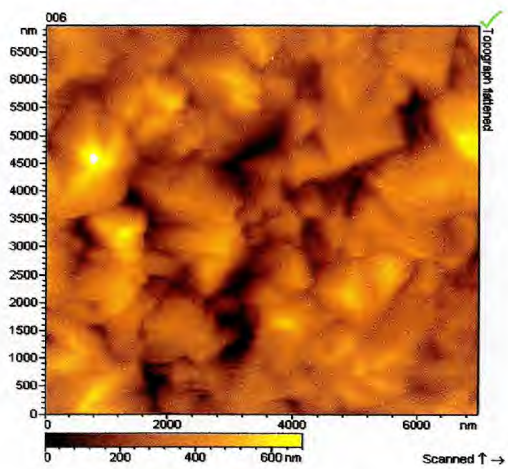


f. Annealed in Ar/H_2 x 8,000

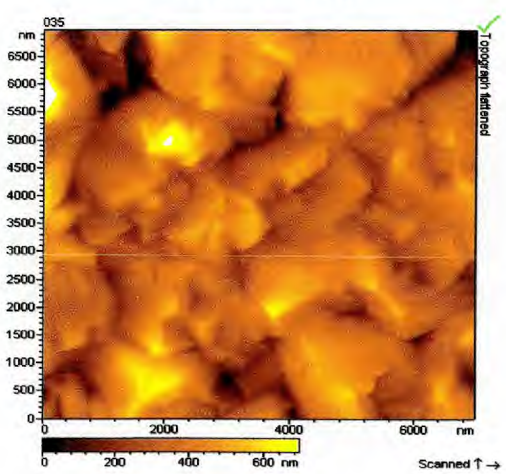
Figure 34 - SEM images of TiO_2/Ti films annealed in different atmospheres at 800 °C for one hour. (a), (b): annealed in air; (c), (d): annealed in Ar; and (e), (f): annealed in mixed Ar/H_2 (10% H_2).



a. annealed in Air



b. annealed in Ar



c. annealed in Ar/H_2

Figure 35 - AFM images of film topography of TiO_2 film deposited on Ti substrate, annealed at 800 °C for one hour in (a), Air, (b), Ar and (c), Ar/H_2

The original motive for annealing samples in argon was to avoid substrate oxidation. However, it was found that after annealing in argon the film topography changed dramatically, and there was still evidence of substrate oxidation. Considering that this may have been due to the oxygen content of the argon remaining relatively high, mixed argon and hydrogen (10% hydrogen) was introduced to further reduce the pO_2 during annealing.

The same topography was observed from the AFM images, Figure 35 (a), (b) and (c). It is clear that the particle size changed significantly in a changing atmosphere. For these films heated in air the particle size is ~70nm, whilst the films annealed in argon had particle sizes of the order of ~100nm and on annealing in argon/hydrogen the particle sizes were ~120nm. Small amounts of microporosity were observed for all samples.

EDS was used to analyse the elemental components in each of the film, in order to investigate the elemental distribution of the film as a function of thickness. FIB was used to create ramps on every films with the ramps milled at 10 degrees. Four points were taken from different areas of each film. They were point 1 for the film surface, point 2 for the upper interface, point 3 for the lower interface, and point 4 for the substrate. FEGSEM was used to observe the topography of the ramp. As can be seen from Figure 36, films annealed in Ar and Ar/H_2 have a porous upper interface, small pores were also observed from the samples annealed in air as shown in Figure 27, however, not to the same extent as in the two alternate atmospheres.

The atomic percentages of Ti and O determined by EDS at the four points of each film are shown in Table 3. It can be seen that, for the sample surface on average the ratio of Ti: O is = 0.50 ± 0.06; this means the film surfaces are of the correct stoichiometry. For the upper interface of the film (the porous area), the atomic percentage for both Ti and O had changed with the ratio of Ti: O = 0.86 ± 0.09, this means that for the porous area, the interface is not of the right stoichiometry for bulk

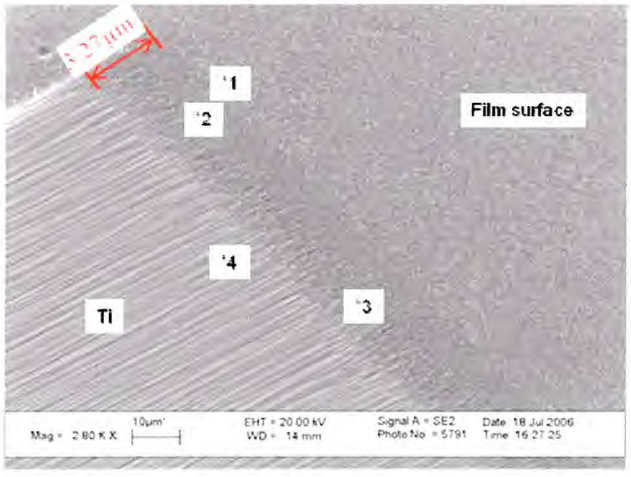
TiO_2 as the Ti content is significantly higher than expected. At point 3, the lower interface, this is also the denser area, the average ratio of Ti: O is again = 0.48 ± 0.02. At point four the atomic percentage for Ti is 100%, which confirmed that the relatively bright area in each film was attributable to the substrate. Of importance here is that no impurities were observed in all four areas of each film, indicating that the film are of high purity.

Table 3 - Atomic percentages of Ti and O at four points of each film (shown in Figure 35) tested by EDS. Films were deposited at current 20mA·cm^{-2} for 45 minutes and annealed at 800 °C for one hour.

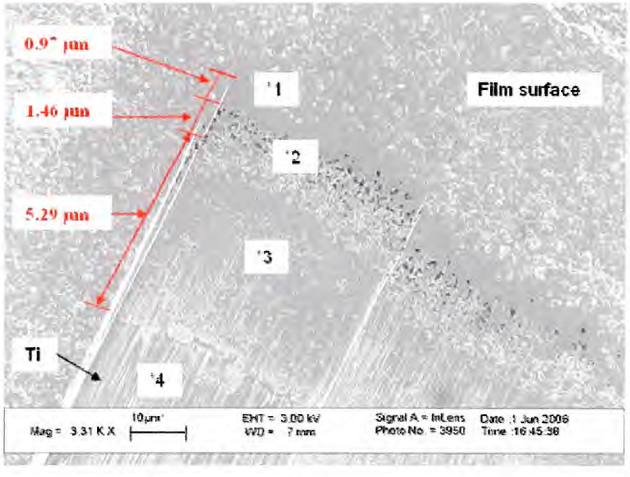
Atomic percentage of Ti and O	Point 1 Film surface	Point 2 Interface (upper)	Point 3 Interface (lower)	Point 4 Substrate
TiO_2 film annealed in Air	Ti:31.11±2.94% O: 68.89±2.94%	Ti:42.77±0.12% O: 57.22±0.12%	Ti:31.87±0.65% O: 68.13±0.65%	Ti: 100.00% O: 0.00%
TiO_2 film annealed in Ar	Ti:37.44±1.86% O: 62.56±1.86%	Ti:49.18±0.21% O: 50.82±0.21%	Ti:33.60±0.34% O: 66.40±0.34%	Ti: 100.00% O: 0.00%
TiO_2 film annealed in Ar/H_2	Ti:32.19±0.28% O: 67.81±0.28%	Ti:46.21±0.05% O: 53.72±0.05%	Ti:31.57±1.53% O: 68.41±1.53%	Ti:100.00% O: 0.00%

Film thicknesses were measured for each sample as well, the way of measuring it is as described in chapter 3.3.4; it should be mentioned that it is difficult to smooth the ramp surface after creating it because the ramp is taken at 10 degrees, and the size is very small (around 120μm x 30μm). After making the ramp the sample has to be taken out for FEGSEM examination and then returned to the FIB, it is difficult to find exactly the same orientation and to smooth it which is why the ramps of the three samples that are shown in Figure 36 are all in different directions. Only the film

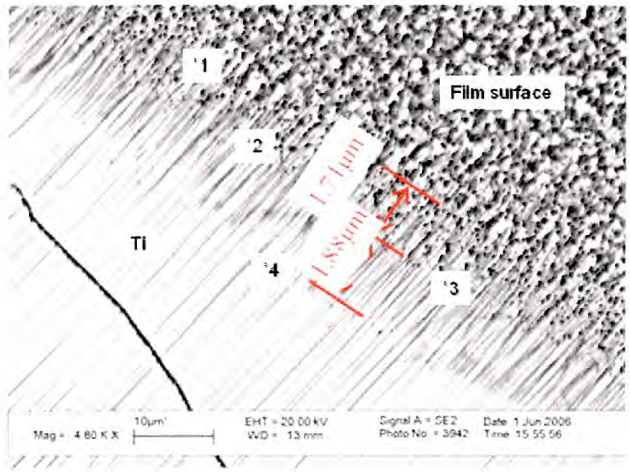
annealed in Ar (Figure 36 (b).) is smoothed after the ramp was made. It can be seen that the surface is clearer after smoothing.



a.



b.



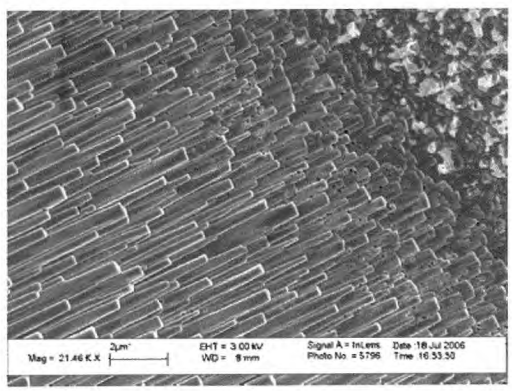
c.

Figure 36 - FEGSEM images of the FIB ramps of TiO_2/Ti films annealed in different atmospheres. a) Film annealed in air; b) film annealed in Ar and c) film annealed in Ar/H_2. Four points on each film were analysed by EDS.

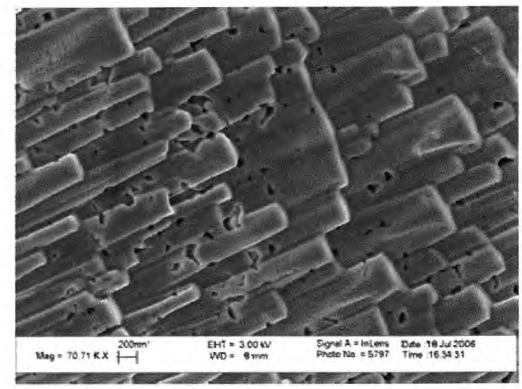
As described in chapter 3.2.3, the thickness of the film annealed in air was 2.71 ± 0.09µm for the film layer and 0.55 ± 0.04µm for the interface layer giving at total thickness of 3.26 ± 0.09µm. The total thickness measured in this sample was 3.27 ± 0.02µm (Figure 36 (a)), in excellent agreement with the earlier sample.

For the film annealed in Ar the situation is more complicated, as shown in Figure 36 (b). As well as the film layer and the dense interface layer the sample also has a very clear porous layer. Even though small pores are also observed at the film layer and the dense interface layer, however, the pores in the porous layer are several times larger. The thickness of the film layer is 0.97±0.03µm, the porous layer is 1.46±0.01µm and the dense interface layer is even thicker than the film itself at about 5.29±0.02µm. Figure 36 (c) shows the TiO_2/Ti sample annealed in Ar/H_2 and it can be seen that no porous layer is present in this sample, however, pores can be found in the film layer. In this case the film thickness is 1.71±0.05µm for the interface layer the thickness is as much as the film layer, around 1.88±0.05µm. The boundary of the interface layer is not very clear and some uncertainty over this thickness is inevitable.

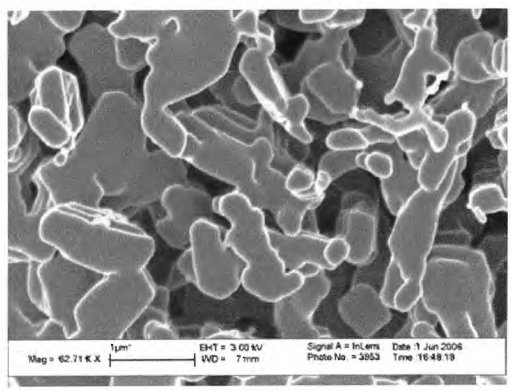
The ramps of the films annealed in different atmospheres were magnified through FEGSEM to investigate the microstructural details of the porous layer (Figure 36). The strip-like shapes (a, b, e, and f) in the ramps is caused by the ion beam; for the smoothed sample (c and d), the surface is flattened by the smoothing beam.



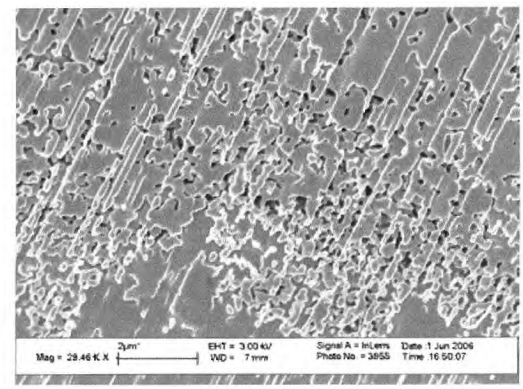
a. film layer



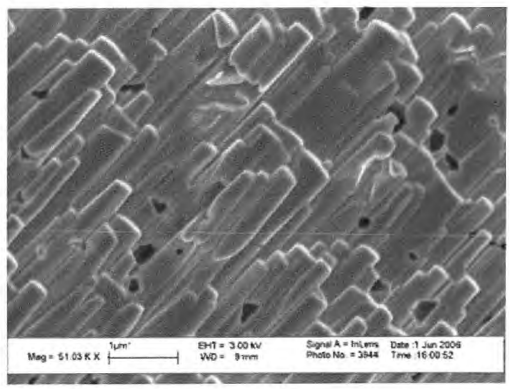
b. magnified porous area



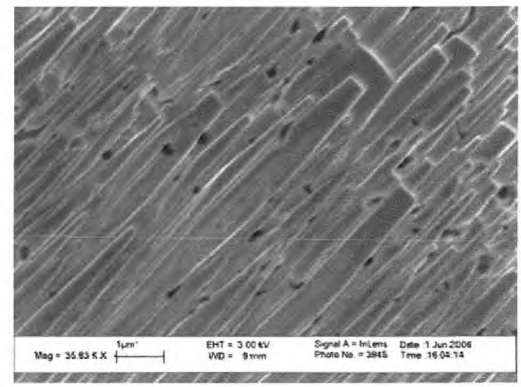
c. porous layer



d. interface area



e. film layer



f. interface layer

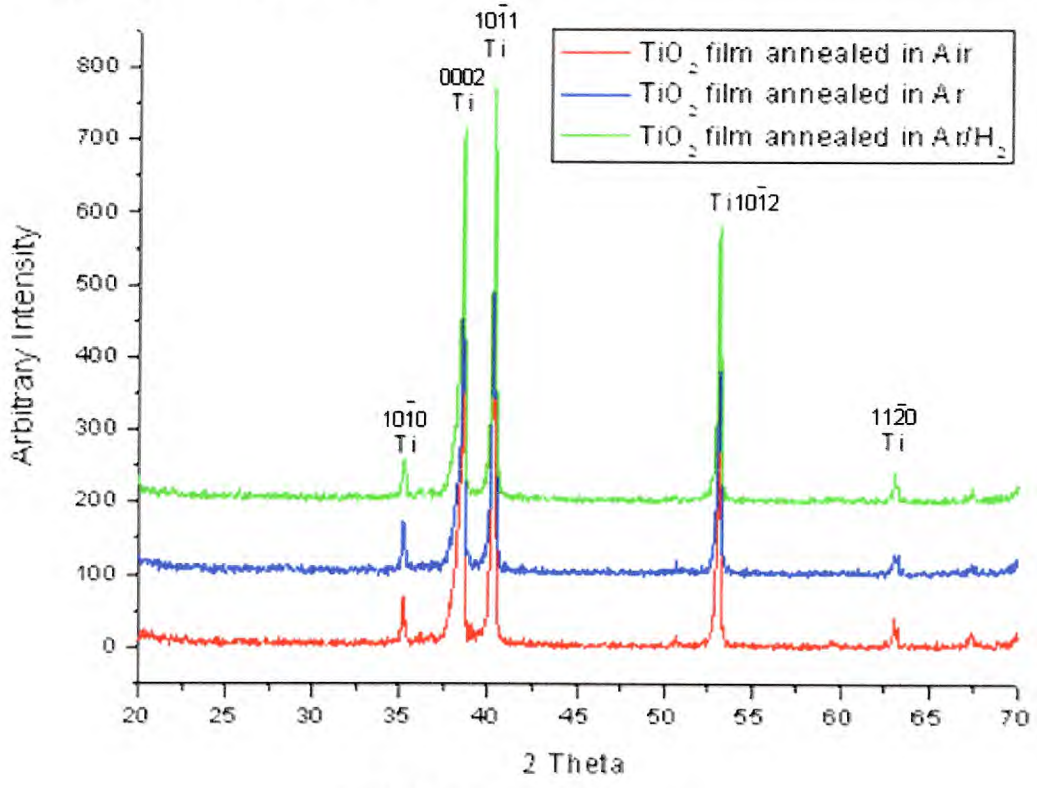
Figure 37 - FEGSEM images of the porous microstructure of TiO_2/Ti films annealed in different atmospheres. (a) and (b), annealed in Air, (c) and (d), annealed in Ar, (e) and (f), annealed in Ar/H_2,

Figure 37 (a) is the film layer of the TiO_2/Ti film annealed in air. It can be seen that the pores were observed close to the surface of the film and on magnifying porous area (Figure 37 (b)) it can seen that the size of the pores was very small, about 100nm. For the sample annealed in Ar, the pores are mainly in the pores layer (Figure 37 (c)) with the size of the pores reaching 0.5μm. The pores size reduced on approaching the interface layer as shown in Figure 37 (d), to around 0.1μm. No porous layer was observed in the films annealed in Ar/H_2, and in the film layer (Figure 37 (e)) few pores were observed. Of the pores that were observed the size was approximately 0.25μm, with no change in the pore size on approaching the interface layer (Figure 37 (f)). The interface of film annealed in Ar/H_2 was of greater density than the interfaces of the films annealed in air and Ar.

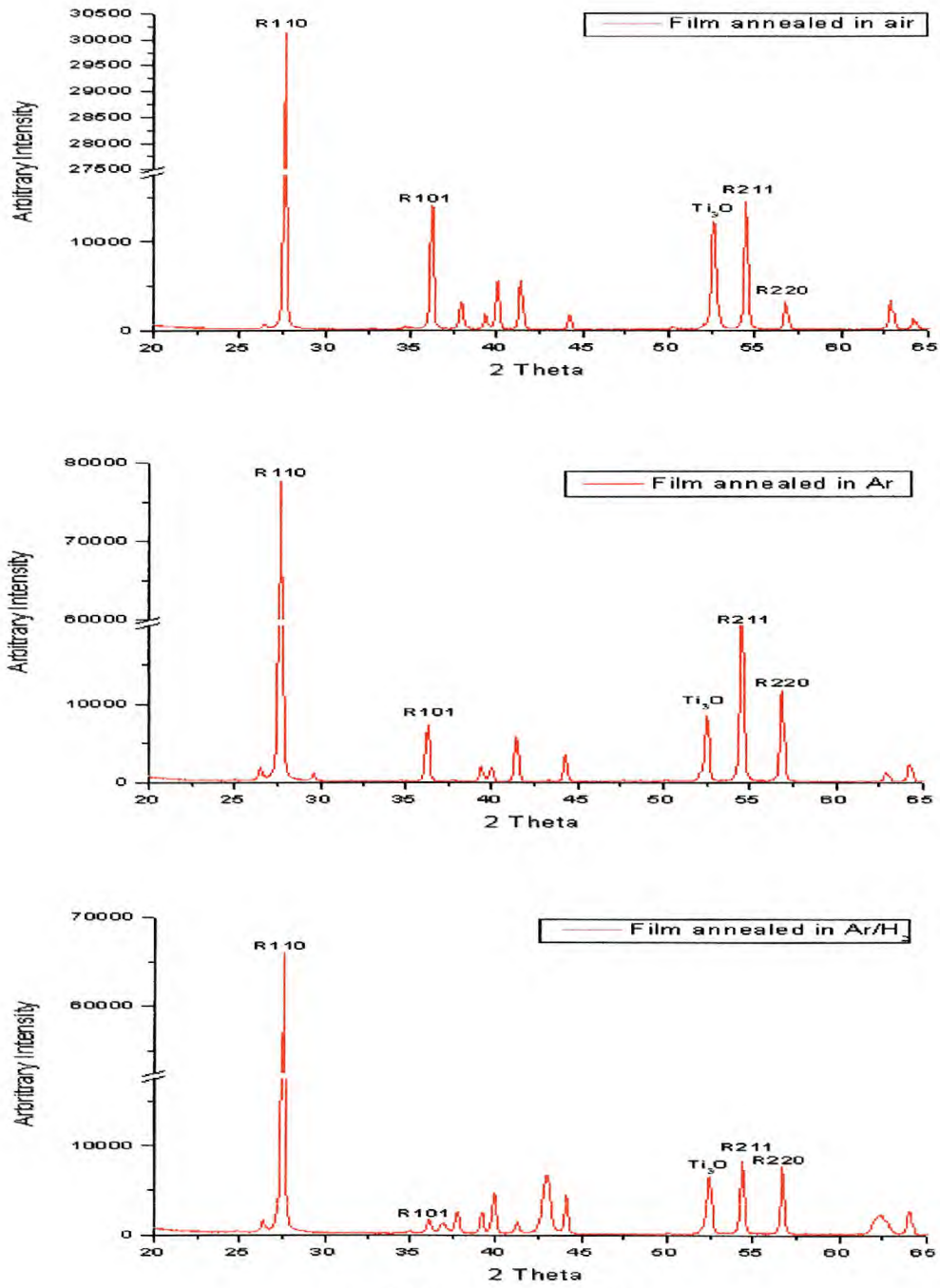
4.4.2 Effect on Film Orientation & Grain Size

4.4.2.1 Film Orientation

After analyzing these samples by XRD it was evident that not only the film particle sizes were changing but also the film orientations were different for the films annealed in different atmospheres. Figure 38 shows the XRD patterns of the as-deposited samples and the samples after annealing in different atmospheres. It is clear that the XRD patterns of the three as-deposited samples are identical, the films are amorphous and no other peaks but those attributed to the Ti substrate were observed (Figure 38, (a)). It should be mentioned that since the Ti metal is rolled, it has (000L) preferred orientation, as (0002) and ($10\bar{1}2$) peaks have much higher intensity than standard X-ray diffraction card of Ti, the results are in good agreement with typically obtained for hot rolled Ti sheets [145].



(a) Before thermal treatment



(b) After thermal treatment

Figure 38 - (a) Comparison of XRD patterns of the three as-deposited samples, and (b), XRD patterns of TiO_2 films annealed in different atmospheres. Films were deposited at current density 20mA·cm^{-2} for 45 minutes and then sintered at 800 °C for one hour. The thicknesses of the films are shown in Table 6.

Differences were found in Figure 38 (b) where patterns of the three samples are shown. For films annealed in Ar and Ar/H_2 the peaks corresponding to the rutile phase have much higher intensity than the peaks that correspond to the rutile phase of the film annealed in air, this means these two films are better crystallized than the film annealed in air. Peaks corresponding to the anatase phase were only found in the film annealed in air.

Some other titanium oxides such as Ti_3O or Ti_6O were also observed indicating that the oxygen is soluble in the metallic Ti substrate [146] (also shown in the phase diagram, Figure 33). As can be seen from the phase diagram Ti_3O appears when the atomic percentage of oxygen is between 20 and 30%, and the anneal temperature is between 400 and 500 °C. Kornilov *et al.* concluded that Ti_3O is stable up to 1400 °C [147]. Kofstad *et al.* [139] reported that Ti_6O appears when the oxygen concentration is between 14 and 15% for anneal temperatures of 650 - 700 °C. Low concentration of the oxide likely to be below the detection limit of the EDS technique.

.

Moreover, films annealed in Ar and Ar/H_2 had narrower peaks when compared with the films annealed in air, which means they have larger crystallite sizes; this result is in agreement with both the FEGSEM and AFM results. The observed results are beyond expectation; it is thought that films annealed in air may have more rutile due to Ti substrate oxidize when annealed in air. For films annealed in Ar and Ar/H_2, since oxygen is evacuated the substrate should not be oxidized.

One interesting observation is that the film annealed in air had grown randomly with no preferred orientation. However, the films annealed in Ar tended to have a (110) orientation and films annealed in Ar/H_2, also have a (110) orientation, other peaks corresponding to the rutile phase such as (101) and (220) are very weak. Figure 39 shows the intensity ratios of rutile (110) and rutile (101) annealed in air, Ar, and

Ar/H_2 respectively. For films annealed in air, the ratio is close to 2, increasing to 11 when annealed in Ar, and then jumps to 40 when the films were annealed in Ar/H_2. The other XRD data for films annealed in different atmospheres are shown in the appendix.

This result is consistent with SEM result shown in Figure 34. Since films annealed in Ar and Ar/H_2 have preferred orientation, Thompson and Wong *et al.* [148, 149] suggested that orientation selective grain growth (also known as secondary grain growth) in thin films can lead to much larger final grain size than normal grain growth. This is because for secondary grain growth, surface energy anisotropy provides a major component of the driving force, which makes large secondary grains grow at faster rates until all normal grains have been annihilated.

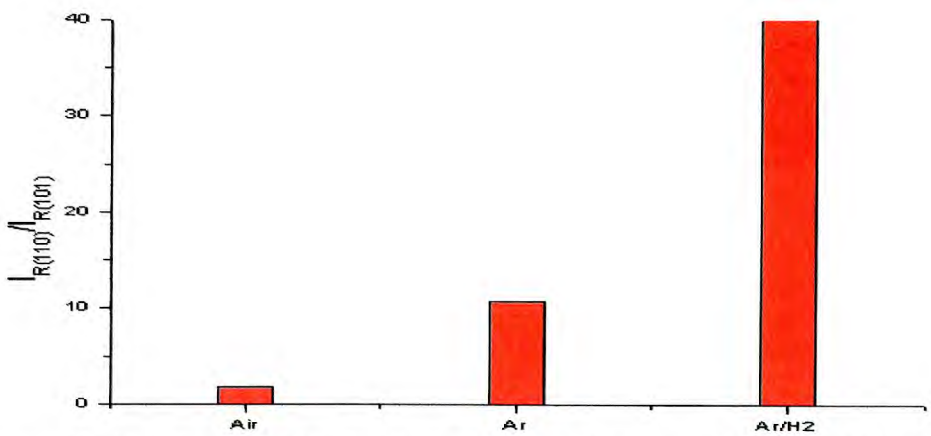
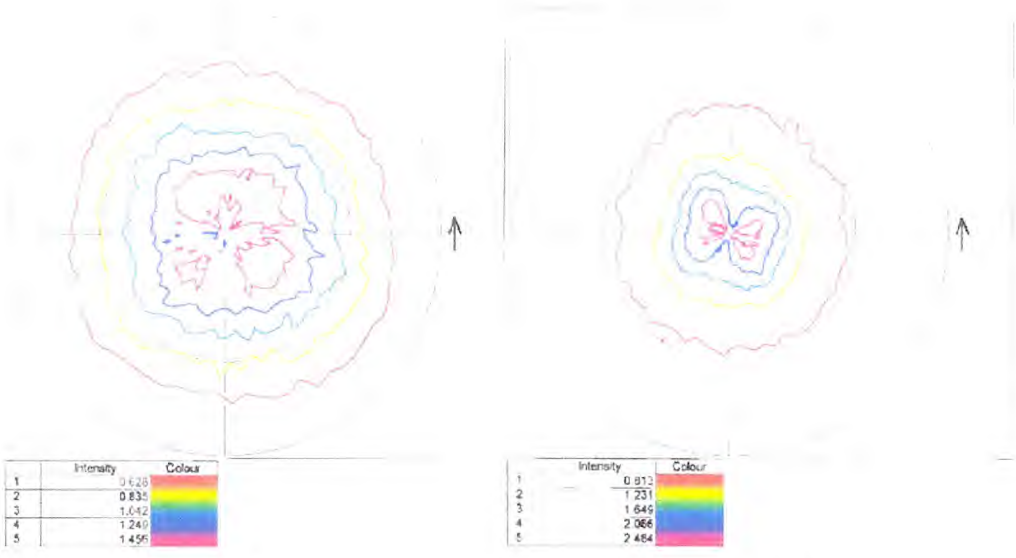


Figure 39 - Intensity ratios of rutile (110) and rutile (101) annealed in air, Ar, and Ar/H_2.

Films annealed in air and Ar/H_2 were analysed by texture measurement to confirm the XRD observation. The texture results (Figure 40) show that indeed the films annealed in air grew randomly as shown by the coloured circles with relatively wide and even distribution and the centre of the circle is separated whereas the films annealed in Ar/H_2 grew with preferred orientation as shown by the coloured circles concentrated in central grid and the centre of the circle is symmetric. Moreover, the intensity of the central circle of films annealed in Ar/H_2 is double that of the film

annealed in air. These results agree with the XRD observation. This confirmed that the films annealed in Ar and Ar/H_2 have preferred orientation in the (110) direction.



(a) (b)

Figure 40 - Pole figures of (a) TiO_2/Ti film annealed in air at 800 °C for one hour; (b) TiO_2/Ti film annealed in Ar/H_2 at 800 °C for one hour.

Considering that no preferred orientation was observed when cobalt doped anatase films were annealed in different atmospheres, the reason for TiO_2 films having preferred orientation may be due to substrate oxidation, as the Ti substrate only oxidizes when the annealing temperature is higher than 750 °C. One possibility is that since the Ti substrate has (000L) orientation, when it oxidizes at high temperature it tends to grow films with low film-substrate interfacial energy, it is known that the energy of the interface will be relativly low when the lattice mismatch is small [150], therefore, films tend to grow with low lattice mismatch. The lattice mismatch of film/substrate can be calculated via equation 4.3 [151]. This equation is also used by other researchers to calculate mismatch [152, 153].

$$f = \frac{d_{film} - d_{sub}}{d_{sub}} \qquad 4.3$$

Where '*f*' is film/substrate misfit parameter, d_{film} and d_{sub} are the plane spacings. Table 4 lists the plane spacing data. It should mention that since rutile has tetragonal structure (lattice parameter: a= 4.5845Å; c= 2.9533 Å) it has different plane spacing for different orientations. The calculated data shows the lattice mismatch '*f*' between R (110) and Ti (0002) is 0.402; the lattice mismatch '*f*' between R (101) and Ti (0002) is 0.074, and the lattice mismatch '*f*' between R (211) and Ti (0002) is -0.272. As can be seen from Figure 37, rutile (110), (101) and (211) were all shown up in every annealing atmosphere. Comparing lattice mismatch among these three orientations, the rutile (101) orientation has smallest lattice mismatch, this means if lattice mismatch is the main reason for film growth towards certain orientation it should be (101) direction. Therefore, lattice mismatch is not the main reason that oxidized Ti substrate grows towards (110) orientation.

Table 4 - Plane spacing of Ti metal and rutile, data observed from [154] and [155].

	Ti (0002)	R (110)	R(101)	R(211)
Plane spacing (Å)	2.316	3.247	2.487	1.685

4.4.2.2 Grain Size

The particle sizes of the TiO_2 films annealed in different atmospheres were calculated, by using the Scherrer equation, and the result is shown in Table 5. These data agree well with the FEGSEM, AFM and XRD results showing that, the particle size of the films increased in the order of the film annealed in Air, Ar and Ar/H_2.

Table 5 - Calculated particle sizes for TiO_2 films annealed in different atmospheres

	TiO_2 film annealed in Air (nm)	TiO_2 film annealed in Ar (nm)	TiO_2 film annealed in Ar/H_2 (nm)
R(110) particle size	72 ± 3	81 ± 9	88 ± 5
R(101) particle size	60 ± 3	55 ± 3	64 ± 5
Average particle size	$57 \sim 75$	$52 \sim 90$	$60 \sim 93$

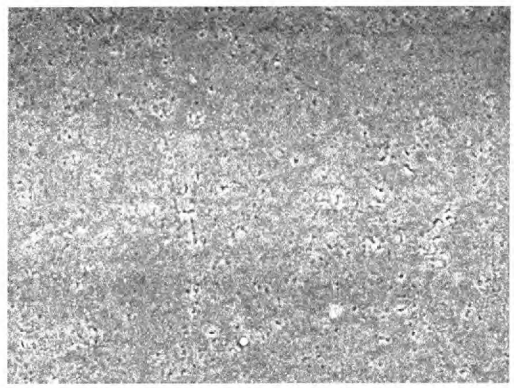
In general, as described above, compared with the TiO_2/Ti film annealed in air, TiO_2/Ti films annealed in Ar have larger particle sizes, preferred orientation (rutile phase (110)) a thicker interface layer and an additional porous layer. TiO_2/Ti films annealed in Ar/H_2 have slightly larger particle sizes, more significant preferred orientation and a less porous interface layer. One explanation of this situation may be that the film itself reacts and changes character when annealed in different atmospheres, however, no characteristic changes occur when the samples are annealed in different atmospheres and heated to 400 °C and held for one and half hours. This means that films annealed in different atmospheres change character only when the temperature is greater than 800 °C.

It is known that the Ti substrate will oxidize when the temperature is higher than 750 °C [136] and when annealing Ti at high temperatures (> 800 °C) and low oxygen pressures (< 10^{-3} torr) titanium dissolves large amounts of oxygen rather than forming an oxide scale [137]. This could explain that the film annealed in argon has a deep interface as the oxygen partial pressure of an Ar atmosphere is 10^{-7} torr. Therefore the differences in oxygen pressure caused by the annealing atmospheres may influence the oxidation of the Ti substrate and subsequently influence the film characteristics.

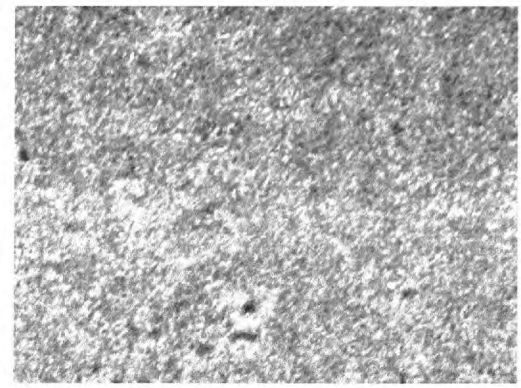
4.4.3 Ti Control Test

In order to clarify this, pure Ti metal substrates were annealed in three different atmospheres directly as a blank test to investigate thermally grown oxide films, and to see if there are any orientation effects.

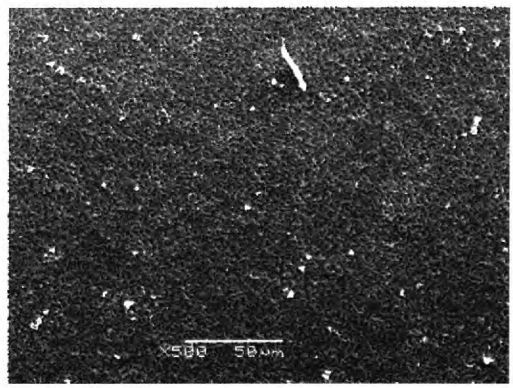
Figure 41 shows SEM images of a Ti substrate annealed in different atmospheres (air (a, b), argon (c, d) and mixed argon and hydrogen (10% hydrogen, e, f) respectively) all held at 800 °C for one hour. As previously observed from the SEM of the TiO_2/Ti films annealed in different atmospheres (Figure 33), at low magnification, all three sample surfaces are identical, dense and uniform (a, c, and e, x 500). Again, film topography changed in Figure 41 b, d and f when the magnification was increased to x 2,000. as observed in Figure 41 b, d, and f, the films annealed in Ar and Ar/H_2 (Figure 41, images d and f respectively) have larger particle sizes than films annealed in air (Figure 41, image b).



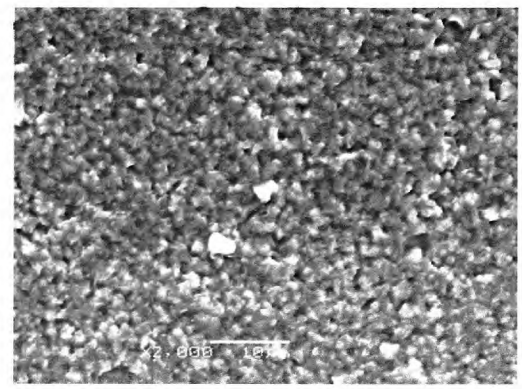
a. Ti annealed in Air x 500



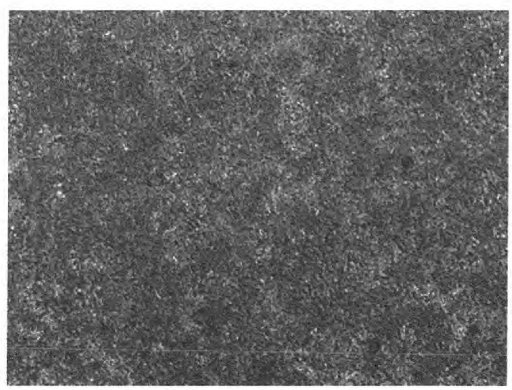
b. Ti annealed in Air x 2,000



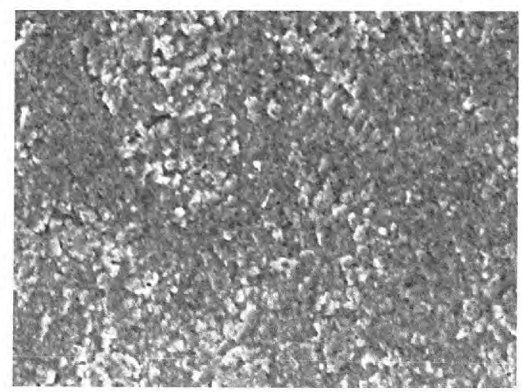
c. Ti annealed in Ar x 500



d. Ti annealed in Ar x 2,000



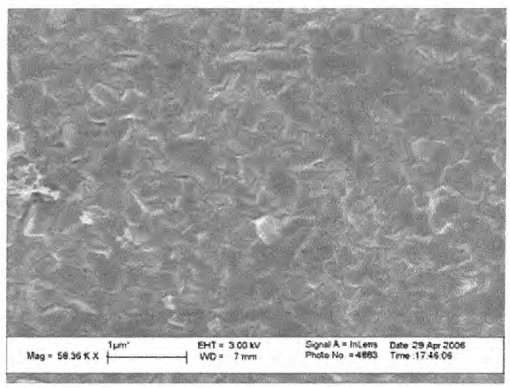
e. Ti annealed in Ar/H_2 x 500



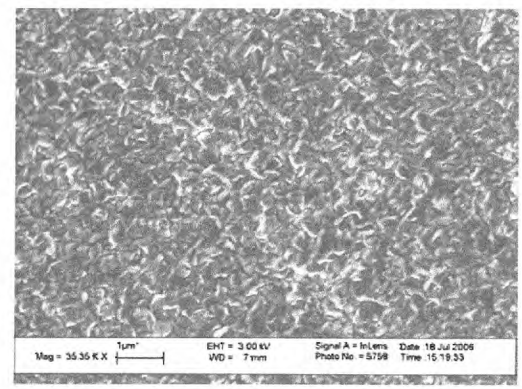
f. Ti annealed in Ar/H_2 x 2,000

Figure 41 - SEM images of a Ti substrate annealed in different atmospheres at 800 °C for one hour. (a, b): annealed in air; (c, d): annealed in Ar; and (e, f): annealed in mixed Ar/H_2 (10% H_2).

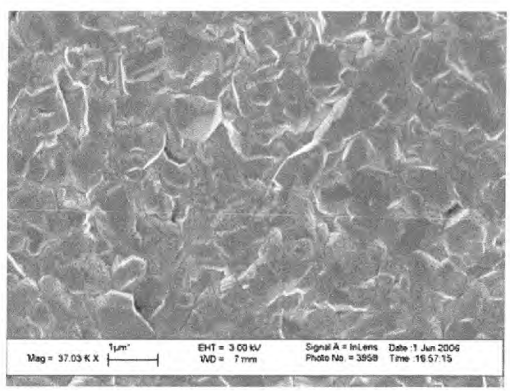
Figure 42 shows FEGSEM images comparing the surface topography between a TiO_2/Ti film and a Ti substrate annealed in different atmospheres. (a) and (b), film and Ti substrate annealed in air, (c) and (d), film and Ti substrate annealed in Ar, and (e) and (f), film and Ti substrate annealed in Ar/H_2. It can be seen that the topographies of TiO_2/Ti film and Ti substrate annealed in different atmospheres are identical. The particles of TiO_2/Ti film and Ti substrate annealed in Ar/H_2 have a more regular shape (Figure 42 (e) and (f)), which means that they are more crystalline, and agree with the XRD data that they have stronger preferred orientation. It should be mentioned that TiO_2/Ti films annealed in air and Ar were gold coated, others were not and that is the reason why the Figure 42 (a) and (c) are not very clear.



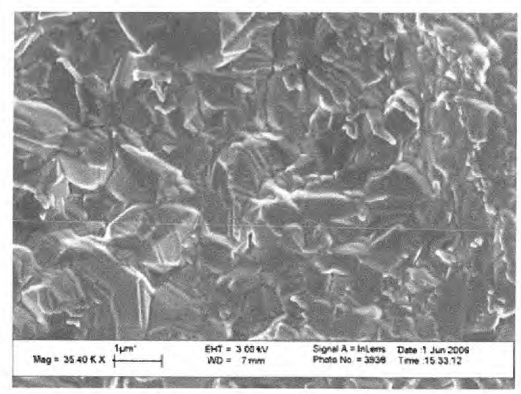
a. TiO_2/Ti film Annealed in Air



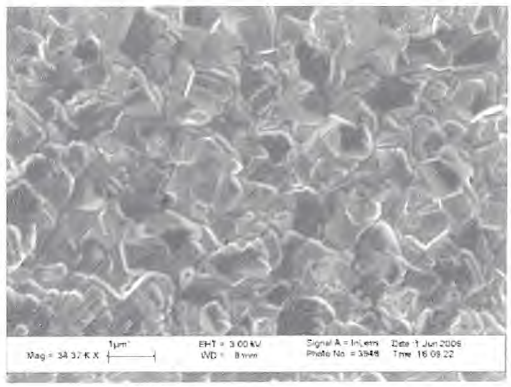
b. Ti Annealed in Air



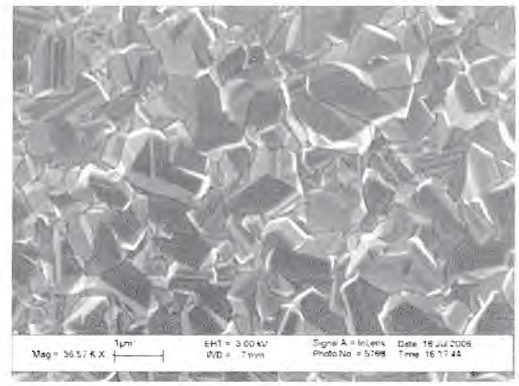
c. TiO_2/Ti film Annealed in Ar



d. Ti Annealed in Ar



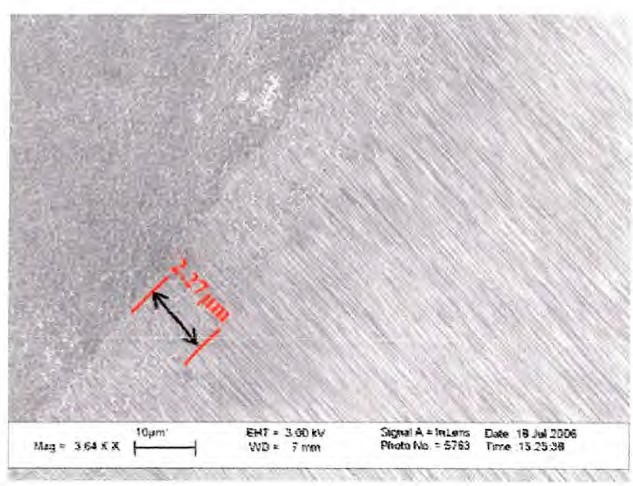
e. TiO_2/Ti film Annealed in Ar/H_2



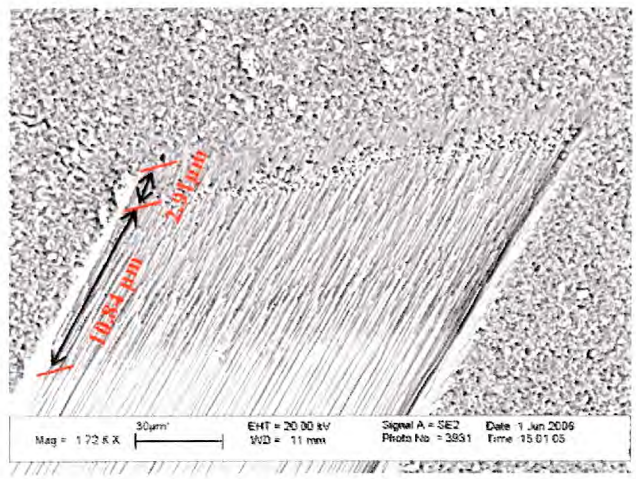
f. Ti Annealed in Ar/H_2

Figure 42 - FEGSEM images comparing the surface topography between TiO_2/Ti film and Ti substrate annealed in different atmospheres at 800 °C for one hour. (a) and (b), film and Ti substrate annealed in air, (c) and (d), film and Ti substrate annealed in Ar, and (e) and (f), film and Ti substrate annealed in Ar/H_2, respectively.

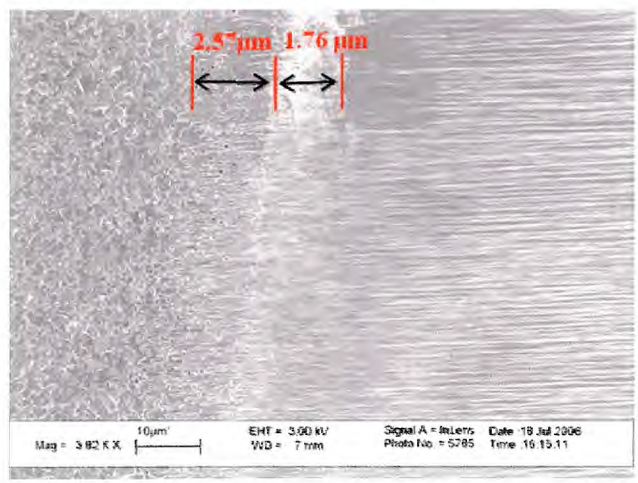
Ramps were also created on each Ti substrate oxidized film using FIB to observe the cross-section topography and measure the thickness of the Ti substrate oxidized film (ramps were taken at 10 degrees). Oxidized films were then analyzed by FEGSEM; the FEGSEM images are shown in Figure 43. Again, the FEGSEM images in Figure 43 are very similar with the images shown in Figure 35.



a



b.



c.

Figure 43 - FEGSEM images of the FIB ramps of Ti substrate oxidized films annealed in different atmospheres. (a) Ti substrate annealed in Air; (b) Ti substrate annealed in Ar and (c) Ti substrate annealed in Ar/H_2. Four points on each film were the EDS tested area.

Table 6 lists thickness differences of Ti oxidized film and deposited film. For the Ti substrate annealed in air, even though the ramp was smoothed the interface can hardly be seen. The total thickness of the oxidized film (Figure 43 (a)) is ~ 1µm thinner than the thickness of TiO_2/Ti film annealed in air. For a Ti substrate annealed in Ar (Figure 43 (b)) the porous layer appears again, moreover, micro pores can be found in both the film layer and the dense interface layer. However, the thickness of the layer is too thin to be measured. Both the film layer and the dense interface layer are thicker than the TiO_2/Ti film annealed in Ar. Figure 43 image (c) shows the Ti substrate annealed in Ar/H_2, the pores were observed at film layer, but there is no

porous layer in this sample. For the interface layer, the same as the TiO_2/Ti film annealed in Ar/H_2, no pores were observed. Compared with the TiO_2/Ti film annealed in Ar/H_2, the interface layer did not change too much; the film layer thickness increased. In general, except for the Ti substrate annealed in air, the oxidized films of the Ti substrate annealed in Ar and Ar/H_2 are thicker than TiO_2/Ti film annealed in Ar and Ar/H_2.

The porous layer on both TiO_2/Ti film and Ti substrate annealed in Ar is attributed to the Kirkendall effect; this is due to during annealing, oxygen diffusion to titanium side is much faster than titanium diffusion to oxide side. Kun *et al.* also made the same observation when zirconia films were annealed on titanium substrates in argon at 1550°C [156]. For samples annealed in air as described in 4.4.2.2, the concentration of oxygen is relatively high, an oxide layer is formed on the film surface, and this will decrease the speed of oxygen diffusion, whereas, for samples annealed in Ar/H_2, the oxygen concentration is even lower than samples annealed in Ar, therefore, the amount of the porous is not enough to form a layer. In general, oxygen pressure is the main reason for porous layer formation.

Table 6 - Thicknesses comparison of Ti oxidized film and deposited film

	Annealed in air (μm)	Annealed in Ar (μm)	Annealed in Ar/H_2 (μm)
Ti oxidized film	Total thickness: 2.27±0.15	Film layer + porous layer:2.91±0.40 Interface layer: 10.84±1.03	Film with porous layer: 2.57±0.14 Interface layer: 1.76±0.16
TiO_2 deposited film	Film layer + porous layer:2.71±0.09 Interface layer: 0.55±0.04	Film layer + porous layer:2.43±0.26 Interface layer: 5.29±0.53	Film with porous layer: 1.71±0.15 Interface layer: 1.88±0.24

The reason that Ti substrates annealed in Ar and Ar/H_2 are thicker than TiO_2/Ti film annealed in Ar and Ar/H_2 is that when Ti is annealed at high temperatures (> 800 °C) and low oxygen pressures (< 10^{-3} torr) titanium dissolves large amounts of oxygen rather than forming an oxide scale during the initial period of reaction[137]. It is the same when titanium with TiO_2 films are annealed at high temperature in high vacuum. Kofstad *et. al* reported that due to the high oxygen solubility and the competition between oxide layer formation and oxygen solution effects, the oxidation of titanium is very complex, therefore, no simple explanation can be given to the various phenomena which are observed at different oxygen pressures and temperatures. For the Ti substrate annealed in air, since the oxygen pressure is relatively high an oxide layer forms and a small amount of oxygen dissolves [157]; for Ti annealed in Ar or Ar/H_2 the oxygen pressure is relatively low, large amounts of oxygen dissolves rather than forming an oxide scale.

Figure 44 shows the XRD comparison pattern of the Ti substrate annealed in different atmospheres. These results are similar with the results of the three XRD patterns shown in section 4.4.2.1 (Figure 37). Both of the thermally oxidized films which were annealed in Ar and Ar/H_2 have preferred orientation (rutile phase (110)) with higher relative intensity compared with Ti substrates annealed in air. Titanium sub-oxide, Ti_3O and Ti_6O were observed in these thermally oxidized films as well. These are the oxides with low oxygen contents [158]. Differences were observed from the TiO_2/Ti film annealed in different atmospheres (Figure 37); no anatase phases were observed in any XRD pattern and for thermally oxidized film in Ar/H_2, (101) rutile peaks can barely be seen, which indicates this film has stronger preferred (110) orientation.

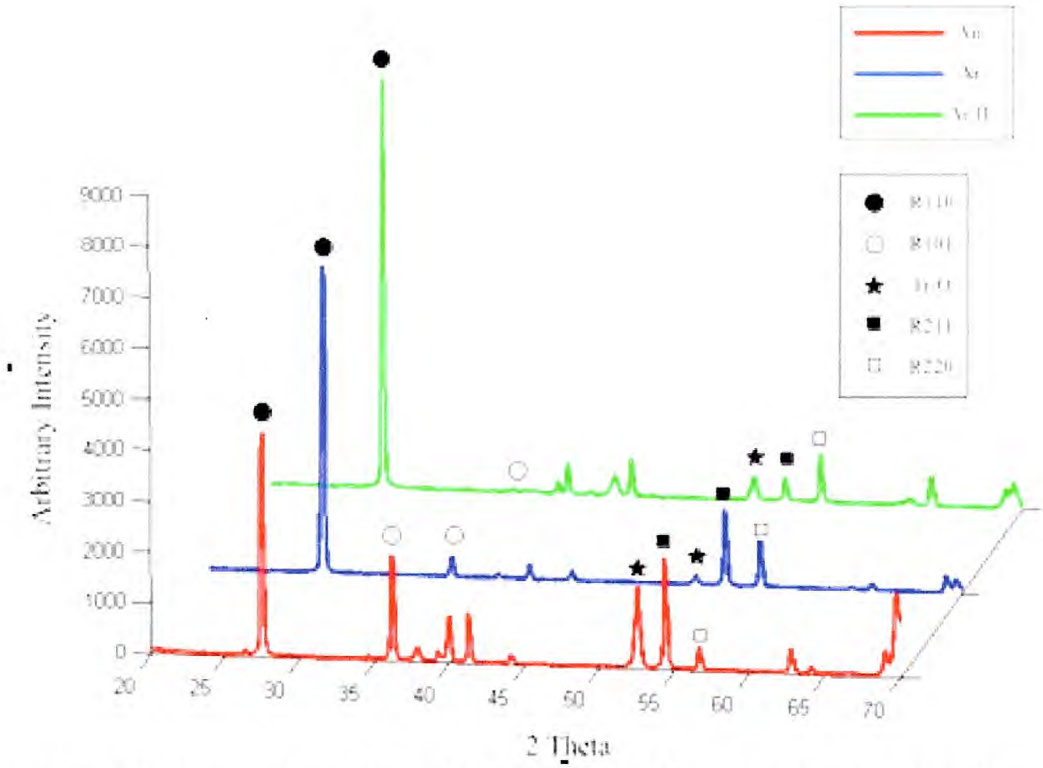


Figure 44 - XRD comparison patterns of the oxidized films of Ti substrate annealed in different atmospheres. Substrates were sintered at 800 °C for one hour

Combining all of the observed results it is not difficult to conclude that the Ti substrate influences TiO_2 film characteristics during thermal treatment in different atmospheres. The reason for the TiO_2 film having preferred orientation after annealing in Ar and Ar/H_2 may be due to much smaller oxygen partial pressure (pO_2 about 10^{-7} torr) than when annealed in air and therefore, the thermodynamic parameters such as surface free energy and strain energy influence the formation of film orientation [159].

As described previously when Ti is annealed in air the concentration of oxygen is relatively high, therefore, a relatively dense oxide layer will form on the substrate surface first. For Ti annealed in Ar and Ar/H_2 the concentration of oxygen is relatively low, therefore, more oxygen dissolves in Ti rather than reacting at the Ti surface to form an oxide layer. This can be observed in Figure 43; Ti annealed in air

has the thinnest oxide layer. Ting *et al.* [157] suggested that strain energy increases with increasing film thickness, therefore, in this study since Ti annealed in Ar and Ar/H_2 is likely to have more oxygen dissolved in the substrate inducing a thicker oxide layer. Strain is therefore higher and in order to reduce this energy the Ti substrate tends to grow towards the orientation which has the lowest surface energy.

It is known that rutile (110) phase exhibits the lowest surface free energy and is the most stable surface [2, 160], therefore, the oxidized Ti substrate forms preferred rutile (110) orientation in order to reduce the overall energy and then induces the deposited film to grow in that orientation. Since Ti substrate acts as a 'getter', it tends to get the oxygen from the TiO_2 deposit. There is an apparent driving force to absorb the oxygen from the TiO_2 deposit. Therefore, rutile TiO_2 crystallites are strongly influenced by the crystallinity and orientation of Ti. This is one of the possible reasons for TiO_2 films deposited on Ti metal having preferred orientation, however, the mechanism of formation/orientation is not clear yet, and will be studied in future work.

Chapter 5.0 Results & Discussion -- Co doped TiO_2 Films

Successfully synthesised Co-doped TiO_2 anatase thin films on Ti and Si substrates were studied in this chapter. X-ray diffraction, high temperature X-ray diffraction, field emission gun scanning electron microscopy equipped with energy dispersive x-ray spectroscopy, focused ion beam, atomic force spectroscopy and x-ray absorption spectroscopy were used to investigate film characteristics. Vibrating sample magnetometry (VSM) was employed to study the ferromagnetic properties of the film. Moreover, films were annealed in different atmospheres to investigate the effect of heat treatment under various atmospheres on the film characteristics.

5.1 As-deposited cobalt doped TiO_2 films

5.1.1 Effect of Variation of Voltage and Time on Film Quality

The preparation of the solution is described in Chapter 3.2.1. During deposition the electrode potential was measured to provide information about the synthesis process according to voltage with time. Figure 45 plots the potential versus time of one of the cobalt doped TiO_2 samples. It is clear that the voltage changed during the electrodeposition. During the first five minutes the potential rapidly increased from 7.49 V to 9.5 V, and subsequently increased relatively slowly from 9.5 V to 10.5 V. It appeared that a plateau was recorded after a time of 45 mins. The reason for the voltage increase during deposition is described in section 4.1.1, and is attributed to the increase of the film thickness.

It should be mentioned that the measured voltage is influenced by the different solution components, solution temperatures, deposition substrates, or the quality of the substrate polishing, therefore, even though the applied current was constantly 20 $mA{\cdot}cm^{-2}$, the measured value of the starting voltage and the final voltage may

slightly vary. The reason for using low temperatures during film deposition (both TiO_2 film and cobalt doped TiO_2 film) is that the titanium peroxocomplex tends to form agglomerates in the solution and before electrodeposition the solution needs to be stirred to allow the titanium peroxocomplex to dissolve in the solution. Therefore, during deposition the low temperature is used to decrease the titanium peroxocomplex agglomeration in order to allow the titanium peroxocomplex to react with OH^-.

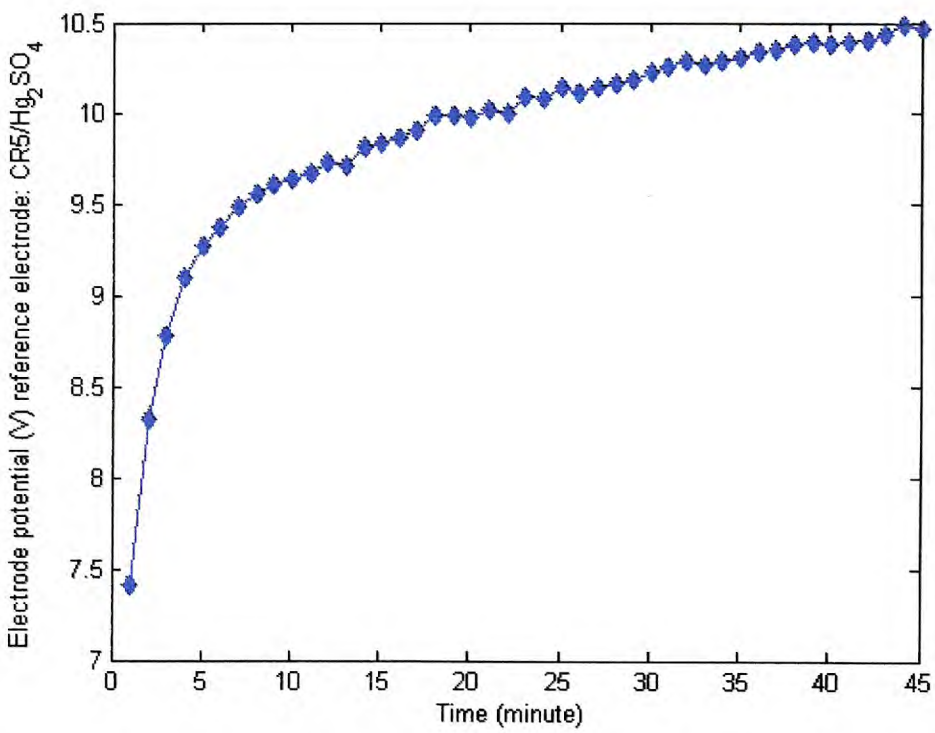


Figure 45 - Variation of electrode potential with deposition time for a cobalt doped TiO_2 film deposited on a Ti substrate; Co^{2+} concentration of 0.05%. Deposition temperature was 0-2 °C, supplied current was 20 $mA \cdot cm^{-2}$.

No significant difference was observed after comparing the potential of electrodeposited TiO_2 films with the potential of electrodeposited cobalt doped TiO_2 films. The resistances of these two films during deposition are virtually identical (7.5 V -11.5 V for electrodeposited TiO_2 films). This means Co^{2+} in the solution does not significantly influence electrodeposition.

5.2 Characterization of Electrodeposited Films

5.2.1 Thermal Treatment

Before annealing the as-deposited film is amorphous and this thermal treatment is used to decompose and dehydrate the titanium peroxocomplex and crystallize the film. Therefore, thermal treatment is a very important step for film formation.

Usually, sample heating is progressed in air with a heating rate of 10 °C/min, at first with a initial duration of one hour. From XRD data (not shown here) obtained it is clear that the peaks corresponding to anatase had no sharp top, this means the film is not fully crystallized, and therefore, indicates that annealing for one hour is not enough and therefore the anneal time was increased to 1.5 hours resulting in sharp anatase peaks observed in the XRD patterns indicating that the film is crystallized.

To investigate the effect of atmosphere on film quality samples were annealed under either Argon or Argon/Hydrogen (10% hydrogen). Prior to the annealing the gas was allowed to purge the alumina furnace tube for at least one hour in order to exclude oxygen.

Initially, the proportion of Ti: Co was set at a molar ratio of 10:1 according to the paper of Matsumoto *et al.*[161]. This is achieved by adding a molar ratio (Ti: Co = 10:1) of $CoCl_2$ in to the stored titanium peroxocomplex solution. The EDS result shown later confirmed that the Co: Ti ratio in the deposited film agreed well with the Co: Ti ratio in the solution. After deposition films were examined using in-situ XRD from room temperature to 600 °C. A scan range of 10° to 60° 2θ, with a heating rate of 60 °C/min was used with the whole scan lasting for 4 hours. It can be seen from the data, Figure 46 that both at room temperature and 300 °C only peaks attributed to the Ti substrate were observed, which means the as-deposited film is amorphous; at 400 °C small peaks corresponding to anatase and $CoTiO_3$ are observed, the film

begins crystallizing; the anatase peaks became sharper when temperature is increased to 500 °C, meanwhile, peaks corresponding to rutile were observed. The intensities of the rutile peaks significantly increased at 600 °C, indicating rutile particle size was increasing, whereas, peaks corresponding to anatase and $CoTiO_3$ nearly stay the same; when the sample is cooled down to room temperature, the intensities of the anatase peaks decreased while the intensities of rutile peaks kept increasing, this means part of TiO_2 continues transforming from the anatase phase to the rutile phase. It should be mentioned that peaks of Pt are due to the heating strip.

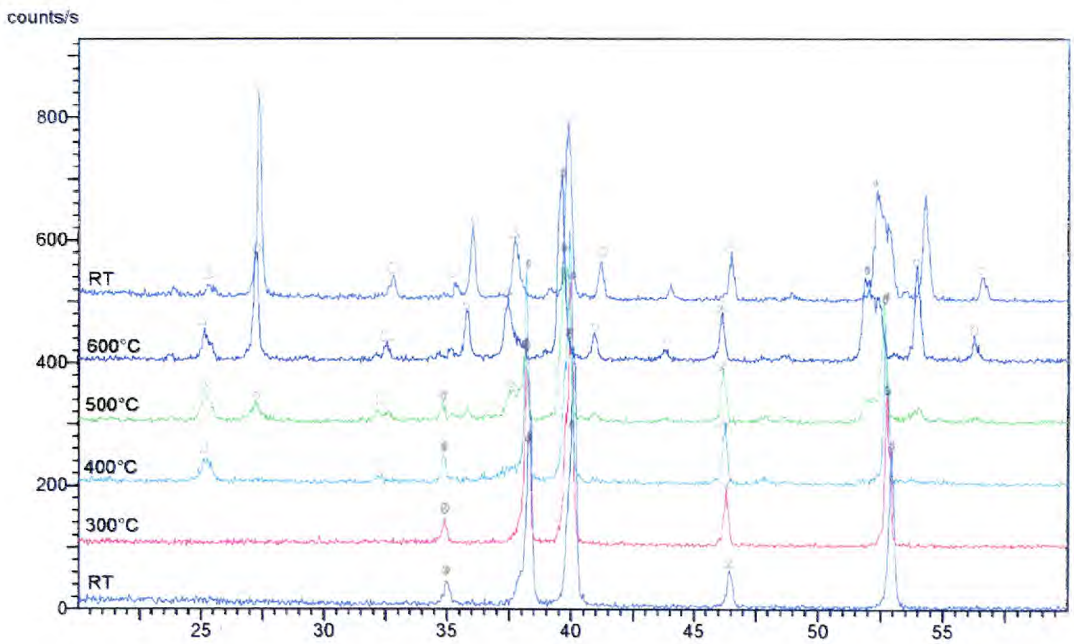


Figure 46 - The In-situ XRD pattern of Co-TiO_2 deposited on Ti substrate (cobalt content 10%). Sample was heated from room temperature to 600 °C and then cooled down to room temperature. Δ-anatase, ○-rutile, □-$CoTiO_3$, ●-Ti substrate, ж-Pt

Comparing with Figure 19 in chapter 4, the anatase to rutile phase transition temperature decreased to 500 °C (the anatase to rutile phase transition temperature is 800 °C in Figure 19); this result is in line with Reidy *et. al*, and the reason could be that defect sites are created and thus provide a low energy mass transport route [162]. Considering that only cobalt doped anatase has been reported to have ferromagnetic

properties [161], therefore, at present neither $CoTiO_3$ or rutile are wanted in the film. And it was observed that no peaks attributable to the rutile phase were observed when the temperature was held at 400 °C, therefore, maintaining the temperature below 400 °C could avoid formation of the rutile phase. Moreover, the reason that $CoTiO_3$ formed could be due to cobalt having a low solubility limit below the 10% used here. One method to avoid $CoTiO_3$ formation is therefore to maintain the Co concentration significantly below 10%. Therefore, the proportion of Ti: Co was changed to a molar ratio of 20:1 giving an expected cobalt content of 5 % to see if stoichiometric deposition occurs.

Figure 47 shows the HTXRD pattern of Co doped anatase film (nominal cobalt content 5%) annealed in Ar at elevated temperature. In order to avoid oxygen effects (such as oxidation of the Ti substrate) during annealing the sample was thermally treated under Ar. Before annealing the chamber was purged with argon for one hour. The scan program was set as: scan at room temperature – heat to 400 °C – hold at 400 °C for one hour – scan at 400 °C , increase this heat in step of 100 °C, hold for one hour and then record data until reaching the maximum temperature of 800 °C and then cool down to room temperature and scan again. As can be seen from Figure 45, the main phase evolution happens in the range between 24° to 37°2θ, so the scan range was therefore reduced to decrease the scan duration and extend the scan time at each point to improve the data quality. This time scan range is changed to 24°- 37° 2θ, with a heating rate of 60 °C/min with the whole data collection lasting for 18 hours.

At room temperature only peaks attributed to the titanium substrate were observed which means the as-deposited film was amorphous. Peaks corresponding to anatase were only observed when the temperature was increased to 400 °C, however, the peak was not sharp, indicating that the film had not crystallized completely; at 500 °C the anatase peak became sharp but now no peaks attributed to $CoTiO_3$ were observed. Once temperature was increased to 600 °C, peaks attributable to the

$CoTiO_3$ phase were observed, coincident with the transformation from anatase to rutile confirming that Co was present in the anatase film. When the temperature reached 800 °C both anatase and rutile phases were observed, meanwhile, the peaks attributed to $CoTiO_3$ became sharp indicating that it had completely crystallized.

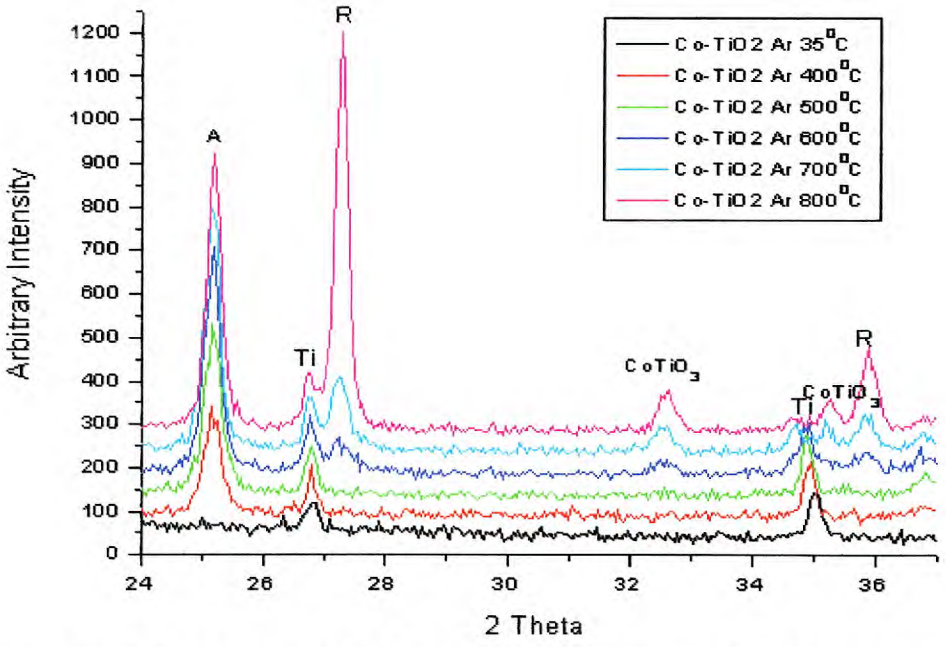


Figure 47 - In-situ XRD pattern of Co doped anatase deposited on titanium substrate annealed in Ar from 0 °C to 800 °C. Molar ratio of Ti: Co in the solution is 20:1, deposited at current density 20mA·cm^{-2} for 45 minutes

Two important points can be obtained from this pattern. First, peaks attributed to $CoTiO_3$ appeared only from 600 °C indicating that Co was in the film. Secondly, it shows that $CoTiO_3$ did not appear until the temperature increased to 600 °C. According to this, in order to avoid the formation of $CoTiO_3$ the anneal temperature should be controlled under 600 °C; moreover, the rutile phase will also be avoided by following that heating regime.

It should be mentioned that there is a peak shift during the in-situ measurements because of the thermal expansion of the film. When the temperature decreased to room temperature the peaks returned to their initial positions. It should also be noted

that the HTXRD experiment under argon results in the intensity of all peaks being approximately 1/10 weaker than when annealed under air, as argon is a better absorber.

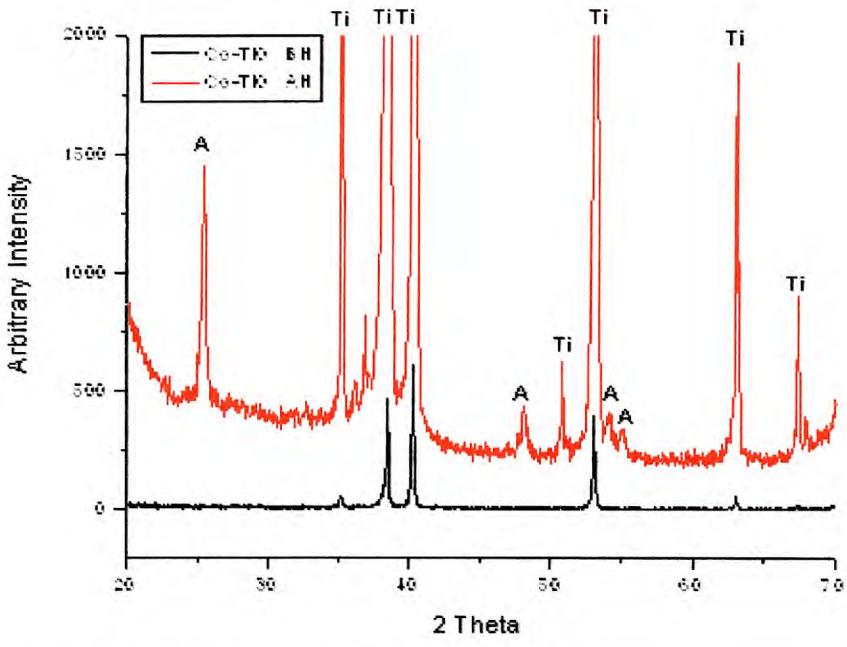


Figure 48 - XRD comparison of Co-TiO_2 deposited on Ti substrate with current density 20mA·cm^{-2} before and after annealing in air (black line: before heat treatment; red line: after heat treatment) the annealed sample was held at 400 °C for 90 minutes

A comparison of the XRD pattern of Co-TiO_2 deposited on Ti before and after annealing is shown in Figure 48. The heating program is: heat sample from room temperature to 400 °C, at a rate of 10 °C/min and hold for 1.5 hours, then cool the sample from 400 °C to room temperature at a rate of 10 °C/min. The XRD pattern post annealing is magnified as the intensity of the Ti substrate is very strong therefore it is difficult to see the anatase peaks clearly. The same result as HTXRD pattern, Figure 46, before thermal treatment the only peaks shown were attributed to the Ti substrate and the film intensity is very low. These observations all confirmed that the as-deposited film is amorphous. After annealing at 400 °C, with increased heating time to 90 minutes to allow the film to be fully annealed and no peaks

attributed to $CoTiO_3$ and rutile were observed. This pattern also shows that the film grows randomly with no preferred orientation.

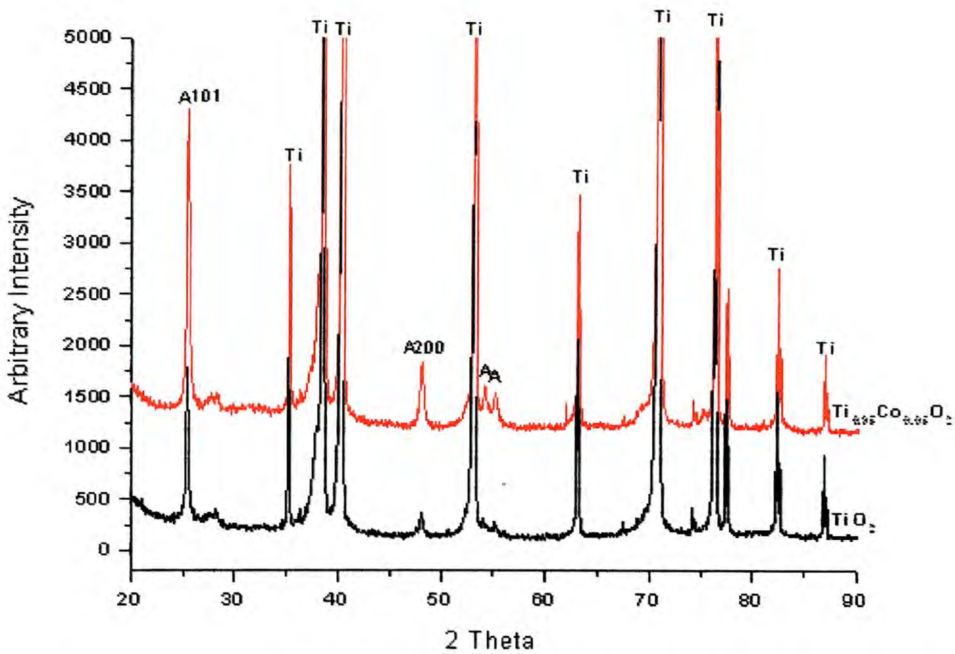


Figure 49 - XRD comparison pattern for doped (x = 0.05) and un-doped anatase film thermally treated at 400°C for 90 minutes. Black line: anatase film deposited on Ti substrate; red line: cobalt doped anatase film deposited on Ti Substrate.

Figure 49 is a comparison of the XRD patterns of doped and un-doped anatase films thermally treated at 400 °C for 90 minutes. Very little difference between the films was observed. However, the shift in angstrom scale can be observed if specifically magnifies those two anatase peaks. The shift of the peaks was measured in order to obtain the change in d spacing and to calculate the lattice parameter. The method used to calculate the lattice parameter is described in section 5.2.2.

Matsumoto *et al.* [6] reported that only peaks corresponding to (004) and (008) anatase phase were observed, but in the present work the (101) and (200) peaks of the anatase phase were observed. Punnoose *et al.* also reported the (101) and (200) peaks [8]. These results are all consistent with this study regarding the random orientation of the film. No peaks attributable to $CoTiO_3$ were observed when the

anneal temperature was maintained at 400 °C or lower. Shinde *et al.* [163] reported that the intensity of doped film peaks should be lower than pure anatase films under the same conditions, however, the situation in the current investigation is entirely opposite, with the peak intensity of the $Ti_{0.95}Co_{0.05}O_2$ film being greater than in pure TiO_2 films prepared under the same condition. The reason for this is still unclear.

5.2.2 Film Surface Morphology & Grain size

Figure 50 shows the surface of the as-deposited Co doped TiO_2 film. The film surface is initially flat and smooth all over the substrate immediately after the deposition; however, as it dries in air for about 10 minutes at room temperature. The film suffers shrinkage and cracking due to dehydration with only small parts remaining as a continuous film. The sizes of the fragments are different; this is because the thickness of the film is not even. It can be seen that, for the thicker areas of the film the size of the fragments are large and the shrinkage gap between the fragments is wide. In the thin areas of the film the size of the fragments is relatively small and the gap is significantly smaller. Moreover, for the very thin areas of the film, no fragments can be seen at all and the whole area looks flat and smooth. This result is consistent with Zhitomirsky et al. [101] who state that because of the non-uniform contraction of the wet coating the film surface will have micro-cracks.

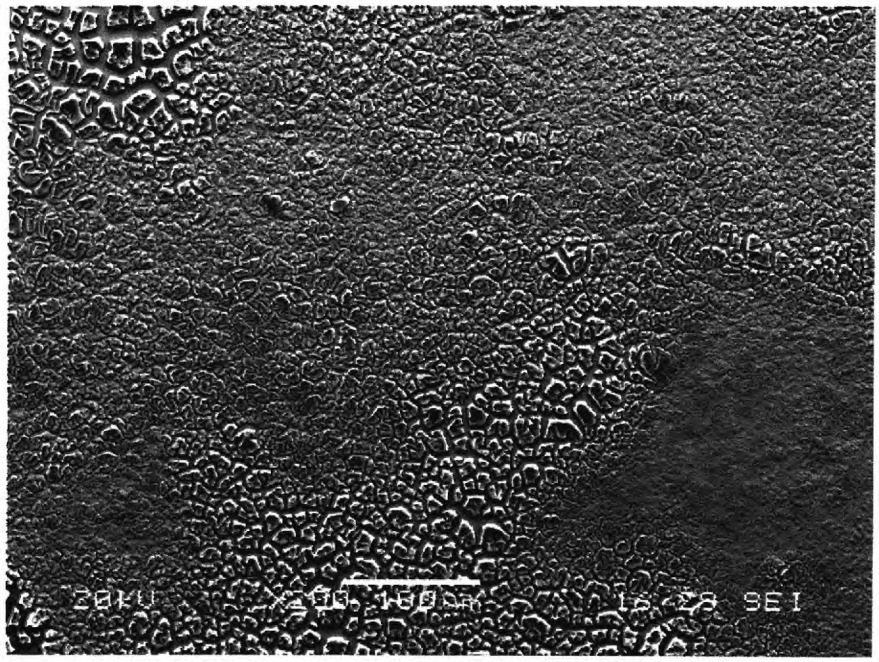


Figure 50 - SEM image of the as-deposited Co doped film on Ti substrate before thermal treatment after air drying at room temperature

Co doped anatase films were also deposited on Si substrates in order to carry out electro/magnetic test for the film. However, it was found that film grown on the Si substrate actually had better quality than films grown on Ti substrates. Figure 51 shows that the film deposited on Si has dehydration effects but did not shrink and fragment, and the whole surface is uniform and even. This indicates that the substrate influences film growth and shrinkage. In preparing Ti substrate, polishing by 3 μm, 1μm and 1/4μm diamond machine was used, however, small scratches were still observed under optical microscopy. Compared with the Ti substrates, the Si substrate was very flat and had no scratches at all, and this improved substrate quality may influence the final film quality.

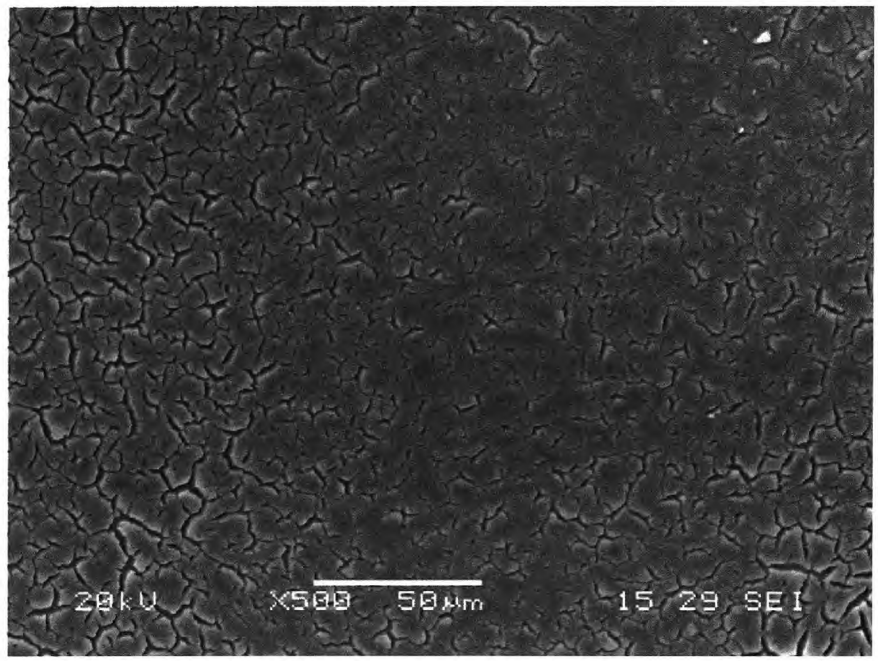


Figure 51 - SEM image of Co doped film on Si substrate before thermal treatment

After annealing at 400 °C for 90 minutes, samples were removed for further analysis. No significant surface morphology change was observed at low magnification after thermal treatment (Figure 52). Some of the fragments peeled off the Si substrate after annealing, indicating that film adhesion was poor. Most of the film was still flat and even. The colour of the film changed from golden brown to blue. This is due to the colour change of the oxidized substrate.

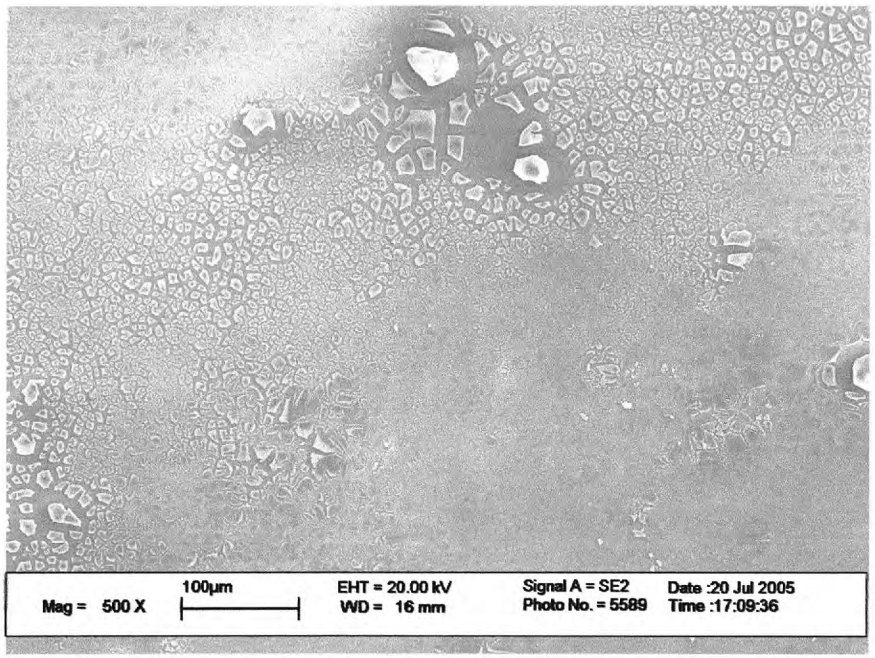


Figure 52 - FEGSEM image of Co doped TiO_2 film after annealing at 400 °C in air

Increasing the magnification of the FEGSEM it is clear that (Figure 53) spherical particles were present, indicating that the film had crystallized. The grain size distribution is relatively homogeneous and about 50 nm in diameter. Energy dispersive x-ray analysis (EDS) was used to analyse the elements present in the film. EDS confirmed that even though the Co content is different in different areas (for example, in some areas Co the content was 1% and in other areas was 5%) Co is detected everywhere in the film. On average, the Co: Ti ratio in the film was 4%, implying near-stoichiometric deposition from the solution. The same grain shape of the doped film is presented in the AFM image, Figure 54. No evidence of Co clusters were observed in either the nano scale FEGSEM or AFM images. This confirms that Co is substituted in to the TiO_2 structure, since cobalt is detected by EDS, but no second phase is apparent in the FEGSEM image indicating no segregation of Co metal. This result disagrees with the report of Kim *et al.* whose Co doped films were prepared by magnetic circular dichroism (MCD) [9].

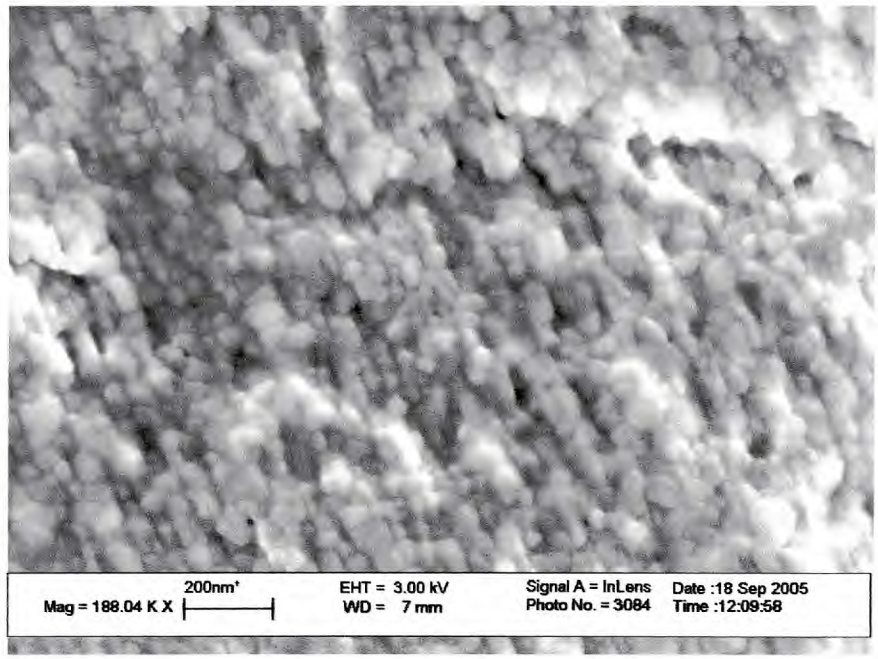


Figure 53 - FEGSEM image of Co-doped TiO_2 film deposition on Ti substrate after annealing at 400 °C in air (magnified image)

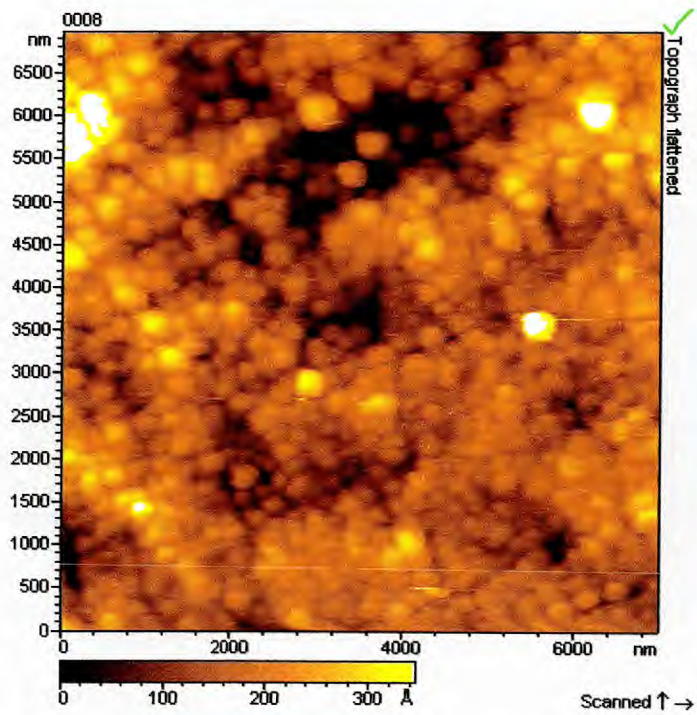


Figure 54 - AFM image of Co-doped TiO_2 film deposition on Ti substrate after annealing at 400 °C in air

By using the XRD measurements the grain size was calculated though the Scherrer equation 4.1, and the result is between 50 nm to 100 nm it is in agreement with the FEGSEM result.

In order to investigate the changes of lattice parameter for doped and un-doped anatase films, lattice parameters were calculated using the listed spacing equation [121]:

$$\text{(Tetragonal)}\quad d_{hkl} = \frac{a}{\sqrt{h^2 + k^2 + l^2(a^2/c^2)}} \qquad 5.1$$

Where d_{hkl} is interplanar spacing, h, k and l are different planes, a and c indicate the lattice parameters. As shown in Table 7, the d-spacing increased for the doped films as expected. The c axis was also found to increase from 9.0080 Å to 9.4780 Å; the results in references [163] and [161] also agree that the value of the c axis increases after doping with cobalt..

From the table below it is clear that the d-spacing of the cobalt doped anatase film has increased and therefore, the lattice parameters of the cobalt doped anatase film were deduced to have increased as well. The possible valence state for Co in the film would be expected to be either Co^{2+} or Co^{3+}. The ionic radii for Co^{2+}, Co^{3+} and Ti^{4+} are listed in Table 8. According to Table 7, lattice parameters of the cobalt doped anatase film increased, it is likely that the Co ionic radii is > Ti^{4+} ionic radii, and considering that the value of the ionic radii should be as close to the original one as possible therefore, it is most likely that, the most likely one is either Co^{2+} in low spin state or Co^{3+} in high spin state that substitutes for Ti^{4+}.

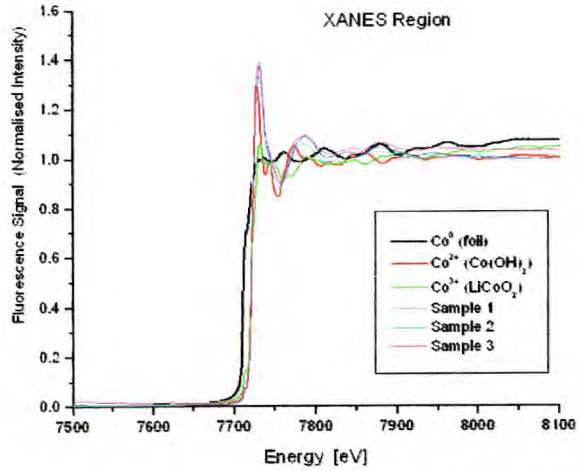
Table 7 - Lattice parameter for doped and un-doped anatase films

Film	Co content at %	Anneal Temperature °C	Anneal Atmosphere	d spacing Å	Lattice parameter Å
TiO_2	0	400	Air	d_{101}=3.501 d_{200}=1.888	a=3.7930(9) c= 9.0080(2)
$Ti_{0.95}Co_{0.05}O_2$	5.0	400	Air	d_{101}=3.505 d_{200}=1.890	a= 3.7853(8) c= 9.4780(3)

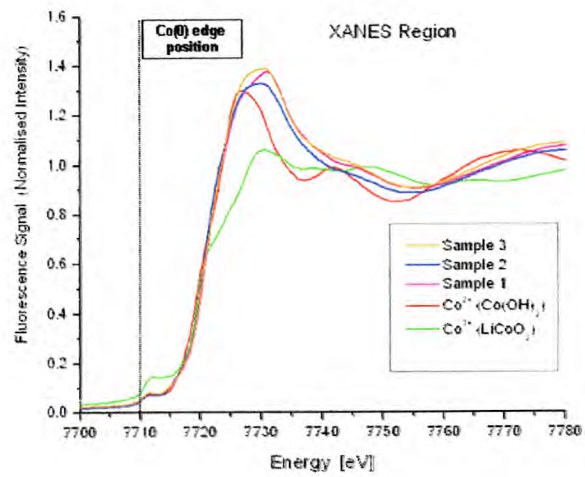
Table 8 - Ionic radii for Co^{2+}, Co^{3+} and Ti^{4+} [164]

Co^{2+}	Low spin	0.065 nm
Co^{2+}	High spin	0.0745 nm
Co^{3+}	Low spin	0.0545 nm
Co^{3+}	High spin	0.061 nm
Ti^{4+}	--	0.0605 nm

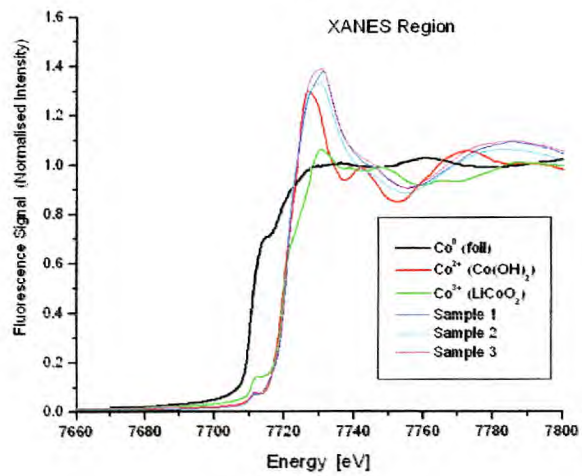
In order to confirm the valence state for Co in the film, X-ray absorption near-edge structure spectroscopy (XANES) was employed. (Synchrotron data were collected by Dr. Bridget Ingham at the Stanford Synchrotron Radiation Laboratory (SSRL) and analysed by the candidate.) Three nominally identical cobalt doped anatase films were measured along with cobalt foil, $LiCoO_2$ (Co^{3+}) and $Co(OH)_2$ (Co^{2+}) as references. Each sample was scanned at least 4 times to improve data quality, and one scan each for the references. Figure 56 is shown the normalized XANES spectra of cobalt doped anatase films in different energy ranges. From Figure 55 (a), it can be seen that at energy ~ 7700 eV edge position (determined at the maximum of the first derivatives of the XANES spectra) samples are very close to Co^{2+} and Co^{3+} (red line and green line respectively) but far away from Co foil (black line). If show close up of the edge region (Figure 55 (b)) it is clear that the shape of the spectra and the absence of a distinct pre-edge feature is close to Co^{2+} (red line). The final normalized XANES spectra is shown in Figure 55 (c), it is concluded that Co in the film is in +2 state. This result is in agreement with Chambers *et al.* [64].



a



b



c

Figure 55 - Normalized XANES spectra of cobalt doped anatase films, (a), energy range between 7500-8100 eV, (b), energy range between 7700-7780 eV, and (c), energy range between 7660-7800 eV.

5.2.3 Film Thickness

The film thickness of electrodeposited cobalt doped anatase was measured by a combination of FIB and FEGSEM. Figure 56 is a FIB image of a Co doped TiO_2 film deposited on a Ti substrate and was taken at a tilt angle of 35°. It can be seen that because of the dehydration the fragments of the films have delaminated from the substrate and curled. It is difficult to make a ramp to measure the thickness under these conditions. Therefore, the thickness of the film was obtained by measuring several edges of the fragments (as shown in Figure 56, the distance between the red lines) and then averaging the results. After careful calculation, the average thickness of Co doped anatase was found to be 0.54 ± 0.09 μm. This image shows that the thickness of the fragments is quite uniform which indicates that in general the film has grown evenly.

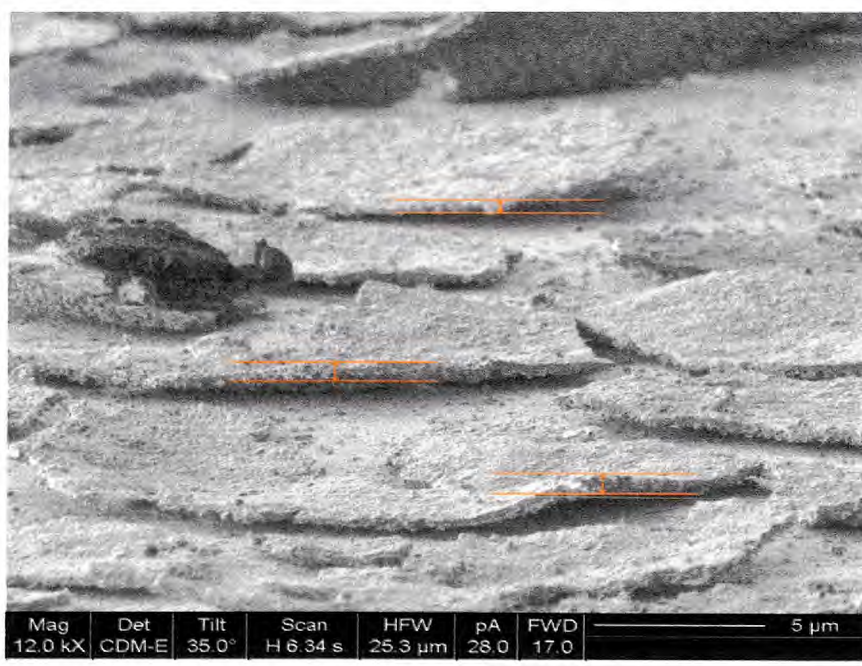


Figure 56 - FIB image of Co doped TiO_2 deposited on Ti substrate. Image was taken at 35°.

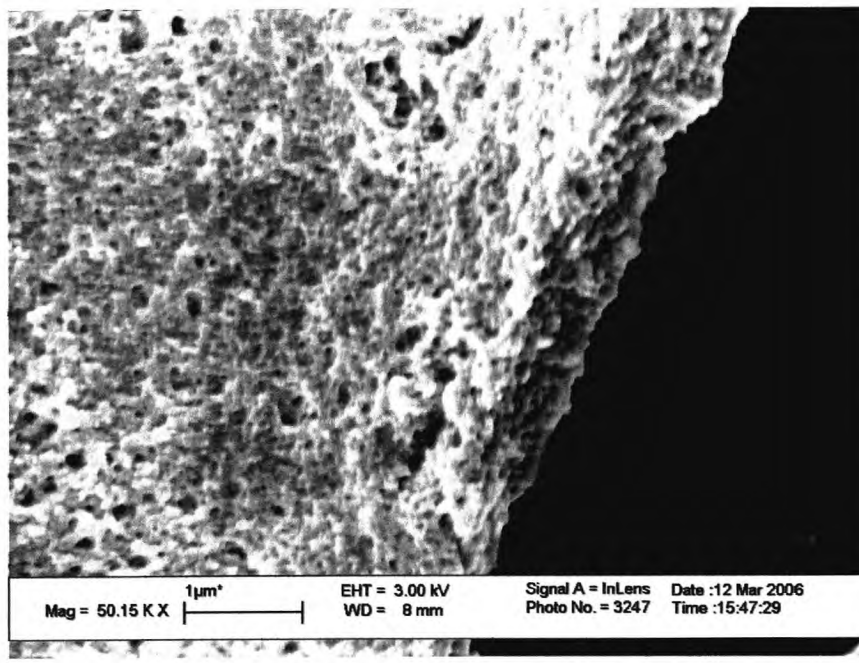


Figure 57 - FEGSEM image of Co doped TiO_2 deposited on Si substrate, cross section.

Figure 57 shows the FEGSEM cross section image of Co doped TiO_2 deposited on a Si substrate. Even though the substrate was changed, the thickness of the film does not change. Uniformly fragment edge is clearly observed from the image. The thickness is again around 0.5µm. As mentioned in section 5.1.1, films deposited on Ti and Si substrates have similar deposition voltage, and here it is confirmed that the film thicknesses are similar as well, therefore, the as-deposited cobalt doped TiO_2 films have similar conductivity to the as-deposited TiO_2 films. A small 'ramp' (100µm x 120µm) is created on a cobalt doped anatase film, In order to investigate microstructural information from beneath the sample surface.

Figure 58 shows the different magnifications of the ramp made by FIB. Image (a) shows the surface topography near the ramp. Some fragments were observed, other place are flat and looks dense. Image (b) is the shape of the ramp, the size of the ramp is 70 X 120 µm. The beam was rastered from the top right of the ramp, the bottom of the ramp is not flat, due to the hardness of the Ti substrate.

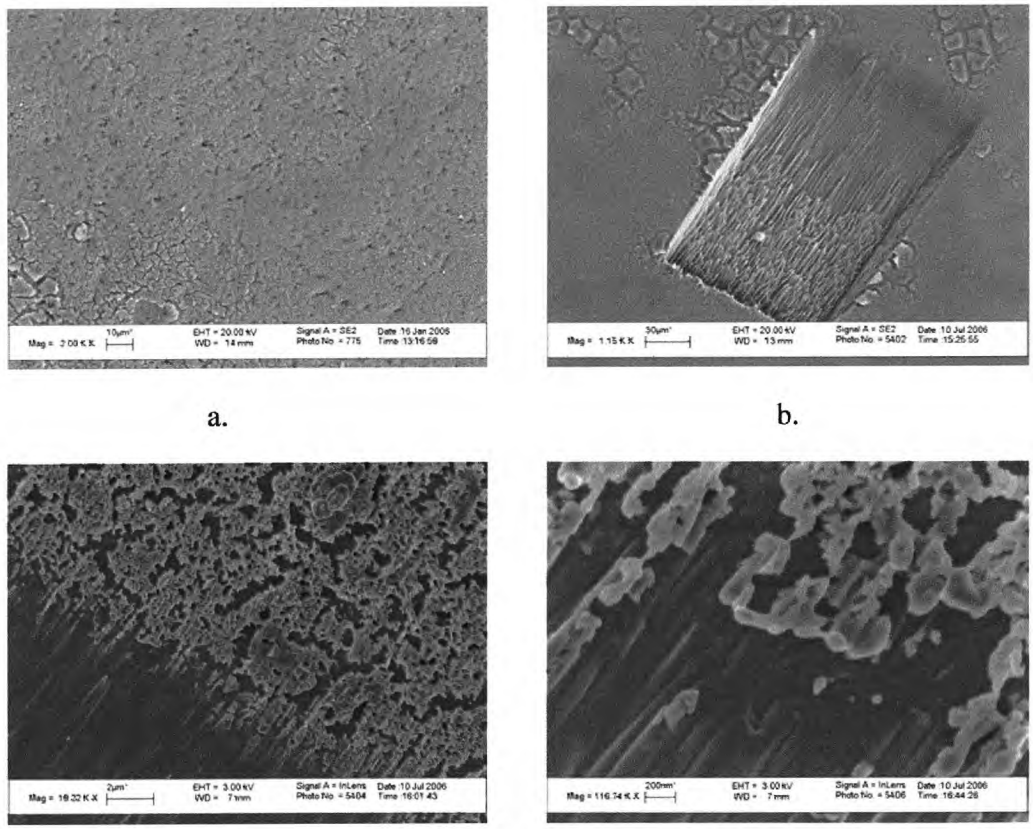


Figure 58 - FEGSEM images of Co-TiO_2 film deposited on Ti (a) film surface topography at low magnification; (b) the ramp made by FIB, the ramp is taken at 30 degree from surface; (c) the magnification of the ramp, white area: film, dark area: Ti substrate; (d) very high magnification, white area: film, dark area: Ti substrate.

At higher magnification there is evidence for a large concentration of pores, and the difference between substrate and film is very clear with the substrate being dense and uniform. Increasing the magnification to image (d), it can be seen that the shape of the film crystals is no longer spherical, and the substrate changes to strips, this is because of the beam damage to the film and the substrate during the creation of the ramp. However, it can still be seen that the film growth is homogeneous from the bottom to the top.

5.3 Film Magnetic Properties

Vibrating sample magnetometry is used to measure the film magnetic properties. (Magnetic measurements were performed by Dr. Will Branford, Department of Physics, Imperial College London.) The film magnetization was measured as a function of magnetic field as shown in Figure 59. There are three samples (denoted A, B and C) produced under normally identical experimental conditions (the same samples used for XANES measurement). In order to observe relatively precise data, the magnetic result was observed by averaging the results of these three samples. The differences between the three samples are most likely attributable to errors in the estimate of film volume; the XANES and XRD data for the three samples are identical. The magnetic field was applied parallel to the film surface and the hysteresis loop was taken at room temperature.

After comparing the shape of these hysteresis loops with a reference standard ferroelectric hysteresis loops [165], it is clear that ferromagnetic material is present in the films and this suggests that the cobalt doped anatase film has ferromagnetic properties at room temperature, which agrees with Matsumoto *et al.* and other researchers [6, 7, 58]. By measuring the magnetization of the film surface and the volume of the deposit, the magnetization per unit volume was deduced. For A, B and C there are $0.4\mu_B$/Co, $0.6\mu_B$/Co and $0.2\mu_B$/Co respectively, therefore, $0.3\mu_B$/Co on average. The signal is of the right order of magnitude for dilute ferromagnetic oxide thin films [48].

Matsumoto *et al.* reported that cobalt ions in the film should either exist as Co^{2+} in the low spin state (LS $t_{2g}^6e_g^1$ S=1/2) [166] or high spin state (HS $t_{2g}^5e_g^2$ S=3/2) [167], or as Co^{3+} in low spin state (LS $t_{2g}^6e_g^0$ S=0) or high spin state (HS $t_{2g}^4e_g^2$ S=0) [168]. As discussed in section 4.2.2, due to the relatively adjacent ionic radii either Co^{2+} at low spin state or Co^{3+} at high spin state may substitute Ti^{4+}. Considering that the magnetization per unit volume measured in our research is $0.3\mu_B$/Co, it is too low for

high-spin Co^{3+} [168, 169], therefore, cobalt ions in the film exist as Co^{2+} low spin configuration, which is consistent with the XRD and XANES data. This suggestion fully agrees with some of the researchers [6, 7], but not with others [9, 10, 65] who suggested that it is the Co metal clusters generated the observed RTF properties. It is clear from the literature that the processing conditions deeply affect the magnetic behavior.

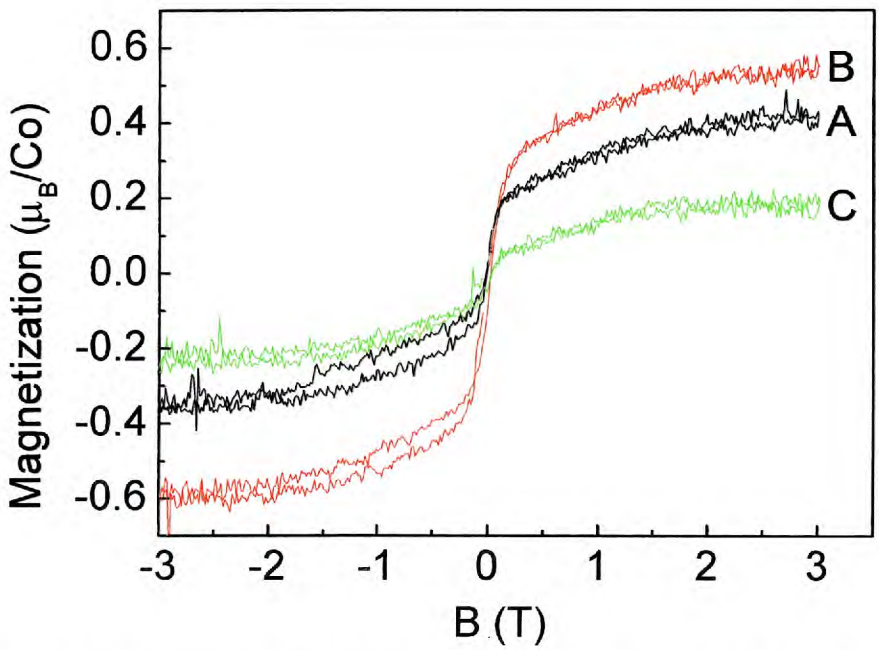


Figure 59 - Room temperature in-plane magnetization vs. magnetic field for three $Co_{0.05}Ti_{0.95}O_2$ samples (denoted A, B and C) produced under nominally identical experimental conditions.

5.4 Effect of Atmosphere on Annealing

In order to investigate the effect of annealing atmosphere on the characteristics (film surface topography, film orientation, and crystal size *etc.*) of cobalt doped anatase films, cobalt doped TiO_2 films were annealed under Air, Ar and Ar/H_2 (10% H_2) respectively at temperature of 400 °C for 90 minutes.

The 3D XRD comparison pattern is shown in Figure 60. It can be seen that even though samples were heat treated in different atmospheres, the XRD patterns are very similar. In contrast to the TiO_2 films annealed in these atmospheres (chapter 4) the (101) and (200) anatase peaks were observed but with no preferred orientation. Moreover, the Ti substrate is detected instead of some Ti_3O or Ti_6O peaks; indicating that the substrate was not oxidized.

Figure 61 shows the AFM images of samples annealed in air, Ar and Ar/H_2 (H_2 10%) respectively. Unlike AFM images of rutile annealed air, Ar, and Ar/H_2 atmospheres, the particle diameters in these images are nearly the same; the range of the particle size is between 30 nm to 65 nm. It is also calculated using equation 3.7; the result is listed in table 9.

Table 9 - The scale of the particle size for cobalt doped anatase and TiO_2 films annealed in different atmospheres.

	Annealed in air	Annealed in Ar	Annealed in Ar/H_2
Co doped anatase (A101)	36 ± 18 nm	37 ± 12 nm	43 ± 19 nm
TiO_2 (R110)	72 ± 3 nm	81 ± 9 nm	88 ± 5 nm

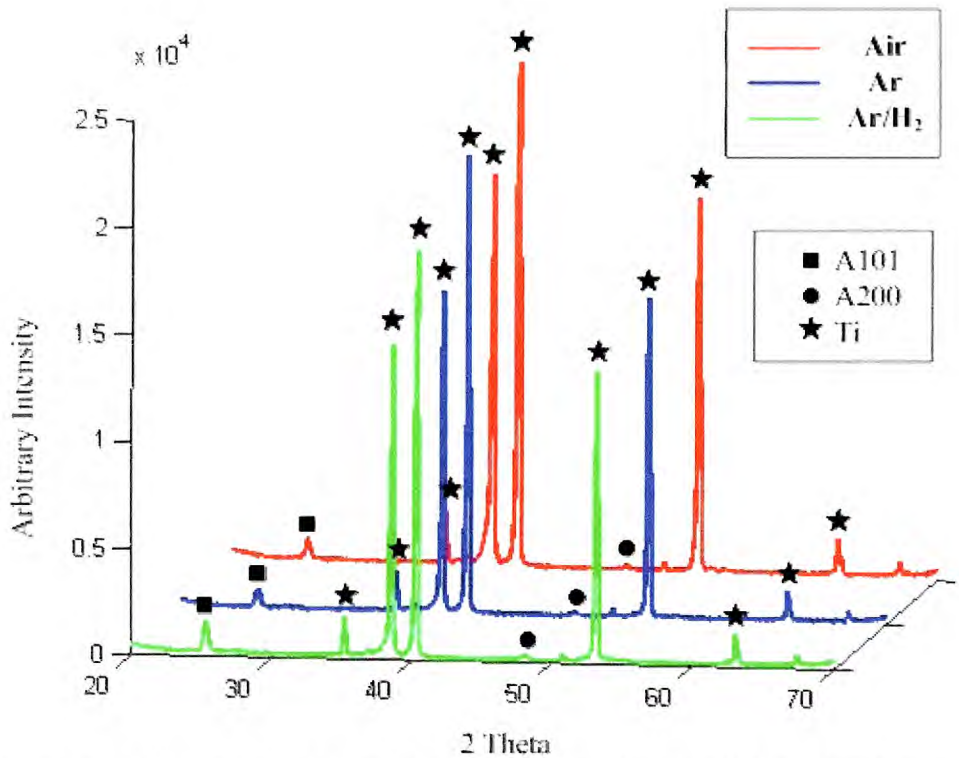
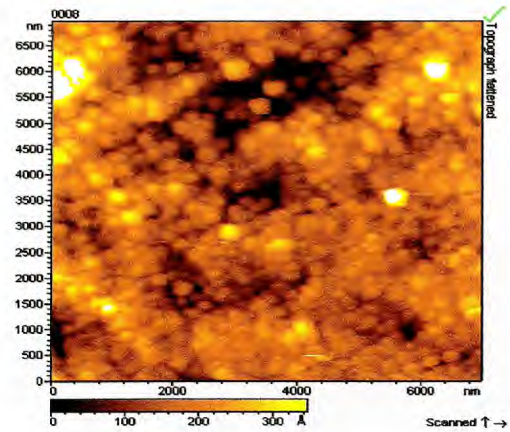
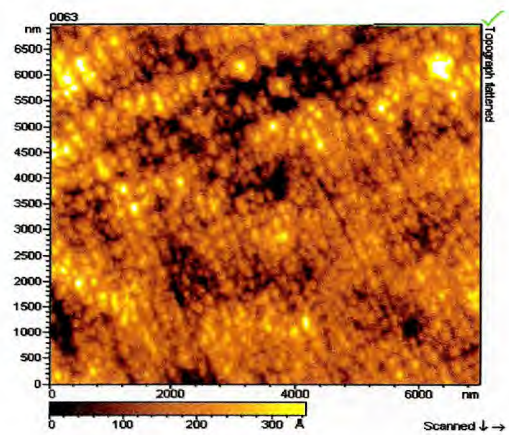


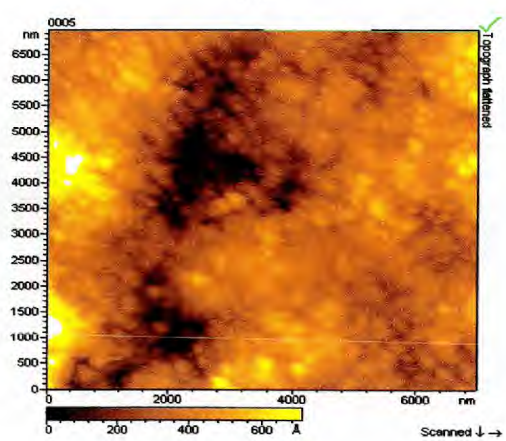
Figure 60 - XRD comparison pattern of cobalt doped anatase annealed in different atmospheres. Red line is film annealed in air; blue line is film annealed in Air and green line is film annealed in mixed argon hydrogen (10% hydrogen). '■' indicates (101) anatase phase; '●' indicates (200) anatase phase, and '★' indicates Ti substrate.



(a)



(b)



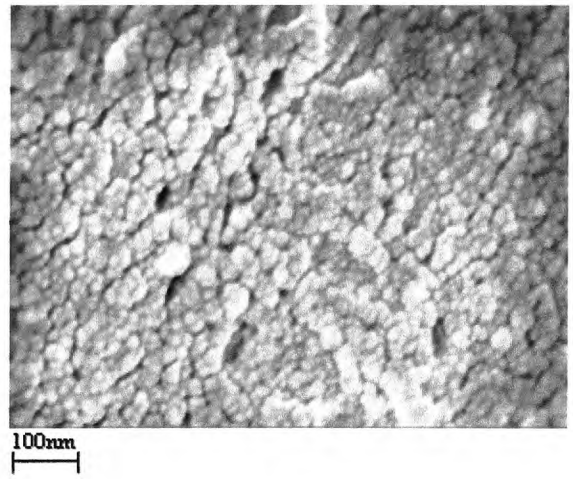
(c)

Figure 61 - AFM images of cobalt doped anatase films deposited on Ti substrate.(a) film annealed in air; (b) film annealed in Ar; (c) film annealed in Ar/H_2 (10% hydrogen).

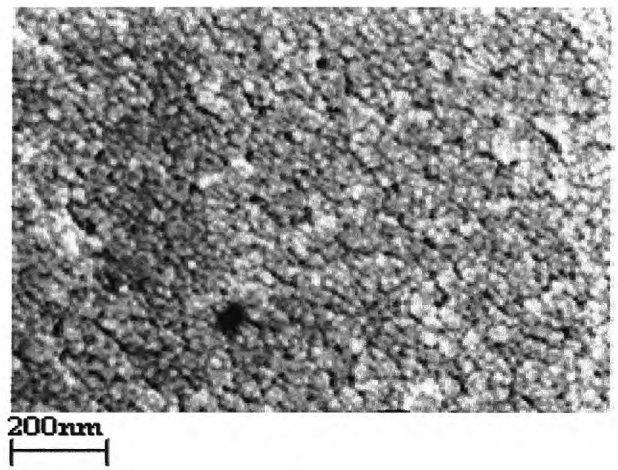
It should be mentioned that it is very difficult to observe the cobalt doped anatase image from the AFM we use and it is difficult to get high resolution FEGSEM images as well.

The reason that it is difficult to get good AFM images of cobalt doped anatase is because from the low resolution FEGSEM images it can be seen that the film has some fragments, however, it is impossible to observe these fragments by eyes. The AFM tip has to be put in touch of the sample surface manually, therefore, it is relatively easy to place the tip either at the edge of the film fragment or at the gap between the two fragments. With the TiO_2 films the situation improves because of the relatively good quality of the TiO_2 films. As mentioned in chapter 2, FEGSEM samples should be conductive and if insulating or partly conductive it should be gold coated. For high resolution images the conductivity should be even higher since the applied voltage is relative low (about 3Kv). The cobalt doped anatase films have very poor conductivity, even though they have been gold coated twice before the experiment, and it was only possible to take images at low magnification. And there is no point to increase the thickness of the gold coat, because the image we demand is in nano-scale, if the gold coat is too thick the particles of the gold can actually been observed.

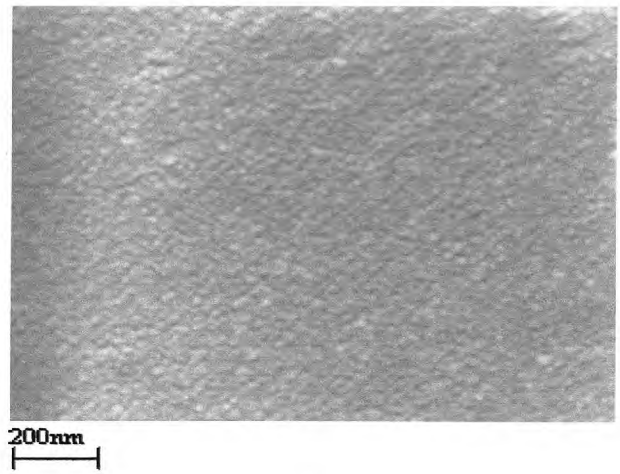
Figure 62 shows the FEGSEM images obtained at high resolution. Due to the difficulty of taking images at high magnification the images were taken not in the same scale. However, the influence of the gold coat can still be recognized by comparing with other FEGSEM images. The result is the same as observed from the AFM images, the grain size of the three samples has very little difference.



a



b



c

Figure 62 - FEGSEM images of cobalt doped anatase deposited on Ti substrate annealed in a) Air; b) Ar and c) Ar/H_2 (10% hydrogen). Samples are all annealed at 400 °C held for 90 minutes.

Combining the results of XRD, AFM and FEGSEM it is possible to determine that the annealing atmosphere did not change the characteristics of the cobalt doped anatase films. The explanation of this is as discussed in chapter 3 that the Ti substrate oxidation influences the film characteristics, Ti metal oxidizes when the anneal temperature is above 750 °C [170] and since cobalt doped anatase films were annealed at 400 °C, the Ti substrate does not oxidize at this temperature and therefore it has no influence on the film and thus the characteristics of cobalt doped anatase films stay the same.

5.4 Summary

In order to broaden the applications of TiO_2 films, such as to increase the photocatalytic or ferromagnetic properties of the TiO_2 films, Co doped anatase films were successfully prepared on Ti and Si substrates by cathodic electrolytic deposition. The film deposited on a Si substrate is of better quality than the film deposited on Ti substrates due to the substrate roughness, but the adhesion may be worse.

When amorphous as-deposited samples were annealed at temperatures above 600 °C $CoTiO_3$ phase was detected in the film, while after controlling the anneal temperature below 600 °C only anatase peaks ((101) and (200)) were observed. After the films were annealed at 400 °C and held for 90 minutes spherical particles were observed in the range of between 50 nm and 100 nm. VSM data confirmed the room-temperature ferromagnetism of the film, and the signal was of the right order of magnitude (0.2-0.6μ_B/Co) for dilute ferromagnetic oxide thin films. Cobalt ions in the film exist as Co^{2+} low spin configuration.

Combining all of the information above suggests that there were no Co metal clusters in the film; Co was substituted for Ti in the lattice and the origin of the

ferromagnetism in the film might be due to the ordered low spin Co^{2+}. Moreover, the film characteristics did not change after annealing in different atmospheres indicating that substrate is the reason for changing film characteristics during heat treatment of TiO_2 above 750°C.

Chapter 6 Conclusions & Future Work

6.1 Conclusions

The cathodic electrodepositions of TiO_2 films and cobalt doped anatase films on Pt, Ti and Si substrates have been successfully performed. A peroxo precursor method was used in order to produce films in aqueous solution. All as-deposited films were found to be amorphous, but can be crystallized by thermal treatment.

During thermal treatment at a temperature above 400 °C the anatase phase starts to form, at 800 °C the film transforms from the anatase phase to the rutile phase, and finally at 1000 °C only the rutile phase can be observed. After thermal treatment at 800 °C for one hour the surface morphology of the film was analyzed by FEGSEM and AFM. It can be seen that the film actually has two morphologies, the spherical particles which indicates anatase phase, with the grain size of approximately between 36±18 nm, and the terrace-like structure which indicates rutile phase, with the grain size of approximately 80±31 nm. In order to confirm these particle sizes the Scherrer equation was used to calculate the grain size from the XRD data, the result of this calculation agreed with the FEGSEM and AFM data. The thickness for films deposited on the Pt substrate is in the range of 0.33±0.16 μm, whereas, for films deposited on a Ti substrate the film thickness is 2.71±0.09 μm. Electrodeposition parameters such as current density, deposition time and annealing temperature influence film quality such as thickness and surface topography.

It is found that compared with films annealed in air, films annealed in Ar and Ar/H_2 (10% hydrogen) have larger grain size (72±3, 81±9, and 88±5 nm respectively) and the films annealed in Ar and Ar/H_2 also are thicker than film annealed in air. Moreover, films have preferred rutile (110) orientation when annealed in Ar and Ar/H_2. This is due to the influence of the oxidation of the Ti substrate on the

deposited film during thermal treatment in different atmospheres. For films annealed in Ar and Ar/H_2 the oxygen partial pressure (pO_2 about 10^{-7} torr) is much lower than when annealed in air and therefore, the thermodynamic parameters such as surface free energy and strain energy influence the formation of film orientation, it is known that the rutile (110) orientation exhibits the lowest surface free energy and is the most stable surface, so the oxidized Ti substrate forms preferred rutile (110) orientation and then induces deposited film to grow in that orientation as well.

Cobalt doped anatase films, $Ti_{1-x}Co_xO_{2-\delta}$, were successfully prepared on Ti and Si substrates by the cathodic electrolytic deposition method as well. When the annealing temperature is greater than 600 °C a $CoTiO_3$ impurity phase is formed along with the rutile polymorph. However, when controlling the annealing temperature below 600 °C only single phase anatase is observed and the lattice parameter is consistent with site-substitution by Co cations.

The films annealed at 400 °C show room-temperature ferromagnetism, and the magnetic moment is on the order of (0.35-0.6μ_B/Co) as expected for such dilute ferromagnetic oxide thin films. No cobalt clusters were observed from the films. The Co oxidation state was detected by XANES and it confirmed that Co in the film exists as +2 state.

Cobalt doped anatase films were also annealed in different atmospheres (Ar and Ar/H_2), however, no grain size change or preferred orientation were observed, since Co-doped anatase films were normally thermally treated at 400 °C and the Ti substrate is not oxidized at that temperature. This point confirms that the oxidation of the Ti substrate influences the film growth orientation.

6.2 Future Work

Even though TiO_2 and cobalt doped anatase films were successfully obtained the films still have cracks. One way to reduce the crack is to control the dehydration process, this means to separate the dehydration and crystallization procedure during thermal treatment. Another way is electrochemical cycling or pulsing, the first one is stop provide current several times during deposition the second is multi-deposit. Both of them try to reduce the coating resistivity. Moreover, some polymer additives such as Poly(diallyldimethylammonium chloride) (PDDA), acting as a binder can also help reduce cracks [171]. Substrate effects such as lattice matching should also be considered. Since Pt, Ti and Si were all employed as substrates, the qualities of the films were increased in this order. Mass spectrum and depth profile of the film needs be studied under SIMS. This equipment provides more precise information of sample component and film thickness.

In order to control the deposit homogeneity, to understand initially formed chemistry and structures and to know the deposition kinetics in-situ XAS such as XANES (X-ray Absorption Near Edge Structure) needs to be employed. The rate of the deposition, valency and coordination of Ti in the deposit shall also be studied under XANES. This equipment can determine the correlation between electrochemical parameters, cell composition and film chemistry, specifically Ti speciation during deposition. Subsequently, film transformation processes during annealing from amorphous to nanocrystalline anatase will be studied.

The reason for TiO_2 films annealed in Ar and Ar/H_2 (10% hydrogen) having larger grain size and the thicker films as well as having preferred rutile (110) orientation is due to the Ti substrate oxidation influencing TiO_2 film characteristics during thermal treatment in these atmospheres at low oxygen pressure. The pO_2 influence during thermal treatment needs to be further studied. And the mechanism of Ti substrate

influences TiO_2 film characteristics at low oxygen pressure also needs to be researched.

Pb and Zr will also be added to the solutions to make PZT films. As mentioned previously, PZT film can be used in different areas, therefore, it is worthwhile to obtain PZT film from electrochemical deposition.

Even though cobalt doped anatase were successfully prepared on Ti and Si substrates by the cathodic electrolytic deposition method, films show room-temperature ferromagnetism, and the magnetic moment is on the order of (0.35-0.6μ_B/Co), the reason that Co-doped anatase has RTFM is still not clear. The extended X-ray absorption fine structure (EXAFS) of the film needs to be employed to investigate the local structure of the cobalt atoms in the film and detect the distance, amount and the variety of the atoms to understand the reason that cobalt doped anatase has RTFM. Co-doped anatase films will be annealed in different atmospheres and temperatures to see if the RTFM change or not, as mentioned in literature review that processing conditions affect the magnetic behavior.

7.0 Appendix

7.1 Master Table for Sample Preparation Conditions

Sample	Figure	Current Density ($mA \cdot cm^{-2}$)	Deposition Time (minutes)	Substrate	Anneal Temperature (°C)	Anneal Time (Minutes)	Anneal Atmosphere
1	14, 20	20	45	Pt			
1	16, 21	20	45	Pt	800	60	Air
2	17	20	45	Pt	From 100 to 1000	Up to 480	Air
3	18, 22, 23, 24, 25, 26, 27	20	45	Ti	800	60	Air
4	19	20	45	Ti	From Room temperature to 800	Up to 360	Air
5	28a, 29	30	45	Ti	800	60	Air
6	28b, 29	20	45	Ti	800	60	Air
7	28c, 29	10	45	Ti	800	60	Air
8	28d, 29	5	45	Ti	800	60	Air
9	30a	20	15	Pt			
10	30b	20	30	Pt			
11	30c	20	45	Pt			
12	31	20	45	Ti	1000	60	Air
13	34a,b, 35a, 36a, 37a,b, 38, 39, 40a, 42a,	20	45	Ti	800	60	Air
14	34c,d, 35b,	20	45	Ti	800	60	Ar

	36b, 37c, d, 38, 39,42c						
15	34e,f, 35c, 36c, 37e,f, 38, 39, 40b, 42e	20	45	Ti	800	60	Ar/H_2 (H_2 10%)
16	41a,b, 42b, 43a, 44			Ti	800	60	Air
17	41c, d, 42d, 43b, 44			Ti	800	60	Ar
18	41e, f, 42f, 43c, 44			Ti	800	60	Ar/H_2 (H_2 10%)
19	45,48,49, 50, 52, 53, 54, 56, 58	20	45	Ti	400	90	air
20	46	20	45	Ti	From room temperature to 600	Up to 240	Air
21	47	20	45	Ti	From room temperature to 800	Up to 1,080	Ar
22	49	20	45	Ti	400	90	Air
23	51, 55, 57, 59	20	45	Si	400	90	Air
24, 25, 26	60	20	45	Ti	400	90	Air, Ar and Ar/H_2 (H_2 10%)
24	61a, 62a	20	45	Ti	400	90	Air
25	61b, 62b	20	45	Ti	400	90	Ar
26	61c, 62c	20	45	Ti	400	90	Ar/H_2 (H_2 10%)

Sample	Table	Current Density ($mA \cdot cm^{-2}$)	Deposition Time (minutes)	Substrate	Anneal Temperature (°C)	Anneal Time (Minutes)	Anneal Atmosphere
3	1	20	45	Ti	800	60	Air
5,6,7, 8	2	30, 20, 10, and 5,	45	Ti			
13,14, 15	3,5,6	20	45	Ti	800	60	Air, Ar and Ar/H_2 (H_2 10%)
16,17, 18	6			Ti	800	60	Air, Ar and Ar/H_2 (H_2 10%)
19,22	7	20	45	Ti	400	90	Air,
24,25, 26	9	20	45	Ti	400	90	Air, Ar and Ar/H_2 (H_2 10%)

7.2 Published Paper

Preparation of Ferromagnetic Cobalt Substituted TiO_2 (Anatase) Thin Films by Electrochemical Deposition

Hao Wang,[†] William R. Branford,[‡,§] Lesley F. Cohen,[‡,||] Stephen J. Skinner,[†,||] and Mary P. Ryan*[,†,||]

Department of Materials, Department of Physics, and London Centre for Nanotechnology, Imperial College London, Exhibition Road, London SW7 2AZ, United Kingdom, and Department of Chemistry, University College London, Gordon Street, London WC1H0AJ, United Kingdom

Received April 3, 2007
Revised Manuscript Received May 22, 2007

Dilute magnetic semiconductors (DMS), also known as semi-magnetic semiconductors,[1] have stimulated considerable interest in recent years.[2,3] Their combined ferromagnetic and semiconducting character is of particular interest for spintronics.[2] However, most DMS cannot be used as room-temperature ferromagnets in practical spintronics applications because they possess low Curie temperatures.[4,5]

Recently, Matsumoto et al.[6] reported that Co-doped anatase thin films, produced by laser ablation in high vacuum, display room-temperature ferromagnetism (RTF). According to this report, when the concentration of Co in the film is between 0 and 8 atom %, the film shows ferromagnetic long-range ordering. The magnetic moment of saturated Co was reported to be 0.32 μ_B, and the film exhibited a positive magnetoresistance (MR) up to 60% at 2 K in an 8 T field. The reason that Co-doped anatase films have RTF characteristics, however, is still unclear. Some researchers[7,8] have suggested that the observed ferromagnetic behavior is caused by Co cations substituted into the anatase lattice, which is similar to the local structure environment of Co in $CoTiO_3$. Others believed that clusters of Co *metal* in these films generated the observed RTF properties.[9,10] More recently, a model based on oxygen vacancies was reported by Liu et al.[11]

Synthesis of Co-doped thin films has been achieved by a variety of methods including spray pyrolysis,[12] oxygen-plasma-assisted molecular-beam epitaxy (OPA-MBE),[7] and reactive co-sputtering[10] and the RTF properties of these films were confirmed. In this study we demonstrate the formation of ferromagnetic Co-doped anatase TiO_2 films by a solution-based process. Cathodic electrolytic deposition (CELD)[13] has been defined as a process in which film deposition is achieved via the hydrolysis of a metal salt solution using an electrogenerated base such as OH^- to form oxides, hydroxides, or peroxides on a cathodic electrode. Hydroxides and peroxides are then converted to oxides by thermal treatment. This method has previously been used successfully to deposit ceramic oxide films such as TiO_2, ZrO_2, and $ZrTiO_4$.[14] In comparison with the other methods electrochemical routes offer several advantages: they are a low-temperature synthesis technique, the procedure is simple and relatively inexpensive, and the film can be controlled through varying the cell parameters (potential or current) or by the composition of the bath. Considering the benefits of the CELD method, we report here on the successful growth of Co-doped anatase films on Ti and Si substrates using electrolytic deposition. The postannealed films are transparent and nanocrystalline and show ferromagnetic behavior at room temperature with no evidence for the formation of Co metal clusters.

The preparation of TiO_2-based films from aqueous solution requires the stabilization of the Ti^{4+} cation in solution; here a peroxo-complex was used (eq 1). On application of a cathodic current to the substrate material, locally generated OH^- reacts with this complex resulting in the precipitation of a Ti–hydroxy film (eq 2).

$$Ti^{4+} + H_2O_2 + (n-2)H_2O \rightarrow [Ti(O_2)(OH)_{(n-2)}]^{(4-n)+} + nH^+ \quad (1)$$

$$[Ti(O_2)(OH)_{(n-2)}]^{(4-n)+} + nOH^- + kH_2O \rightarrow TiO_3\cdot(H_2O)x \quad (2)$$

With the addition of Co^{2+} to the electrolyte this becomes

$$(1-y)[Ti(O_2)(OH)_{(n-2)}]^{(4-n)+} + nOH^- + kH_2O + yCo^{2+} \rightarrow Ti_{(1-y)}Co_yO_3\cdot(H_2O)x \quad (3)$$

The as-deposited material is gel-like (amorphous and hydrated). The Co cation is incorporated into this gel as it deposits onto the surface (eq 3) in approximately equivalent concentrations as the molar fraction in solution, as confirmed by energy dispersive X-ray spectroscopy (EDS). The total film thickness after 45 min deposition is ~500 nm (measured in cross section in the scanning electron microscope) indicating an average deposition rate of around 0.2 nm·s^{-1}.

* Corresponding author. E-mail: m.p.ryan@imperial.ac.uk.
† Department of Materials, Imperial College London.
‡ Department of Physics, Imperial College London.
§ University College London.
|| London Centre for Nanotechnology, Imperial College London.

(1) Furdyna, J. K. *J. Appl. Phys.* **1988**, *64*, R29–R64.
(2) Ohno, H. *Science* **1988**, *281*, 951–956.
(3) Fukumura, T.; Jin, Z.; Ohtomo, A.; Koinuma, H.; Kawasaki, M. *Appl. Phys. Lett.* **1999**, *75*, 3366–3368.
(4) Ohno, H. *Science* **2001**, *291*, 840–841.
(5) Yang, Z. X.; Liu, G.; Wu, R. Q. *Phys. Rev. B* **2003**, *67*, 060402-1–060402-4.
(6) Matsumoto, Y. J.; Murakami, M.; Shono, T. J.; Hasegawa, T.; Fukumura, T.; Kawasaki, M.; Ahmet, P.; Chikyow, T.; Koshihara, S. Y.; Koinuma, H.; Koinuma, H. *Science* **2001**, *291*, 854–856.
(7) Chambers, S. A.; Thevuthasan, S.; Farrow, R. F. C.; Marks, R. F.; Thiele, J. U.; Folks, L.; Samant, M. G.; Kellock, A. J.; Ruzycki, N.; Ederer, D. L.; Diebol, U. *Appl. Phys. Lett.* **2001**, *79*, 3467–3469.
(8) Punnoose, A.; Seehra, M. S.; Park, W. K.; Moodera, J. S. *J. Appl. Phys.* **2003**, *93*, 7867–7869.
(9) Kim, J. Y.; Park, J. H.; Park, B. G.; Noh, H. J.; Oh, S. J.; Yang, J. S.; Kim, D. H.; Bu, S. D.; Noh, T. W.; Lin, H. J.; Hsieh, H. H.; Chen, C. T. *Phys. Rev. Lett.* **2003**, *90*, 017401-1–017401-4.
(10) Wan, K. Y.; Ricardo, P.; Ortega-Hertogs, J.; Jagadeesh, S.; Punnoose, A. M.; Seehra, M. S. *J. Appl. Phys.* **2002**, *91*, 8093–8095.
(11) Liu, L. F.; Kang, J. F.; Wang, Y.; Tang, H.; Kong, L. G.; Zhang, X.; Han, R. Q. *Solid State Commun.* **2006**, *139*, 263–267.
(12) Manivannan, A.; Seehra, M. S.; Majumder, S. B.; Katiyar, R. S. *Appl. Phys. Lett.* **2003**, *83*, 111–113.
(13) Zhitomirsky, I. *J. Eur. Ceram. Soc.* **1999**, *19*, 2581–2587.
(14) Zhitomirsky, I.; Gal-Or, L. *J. Eur. Ceram. Soc.* **1996**, *16*, 819–824.

10.1021/cm070928r CCC: $37.00 © 2007 American Chemical Society
Published on Web 06/05/2007

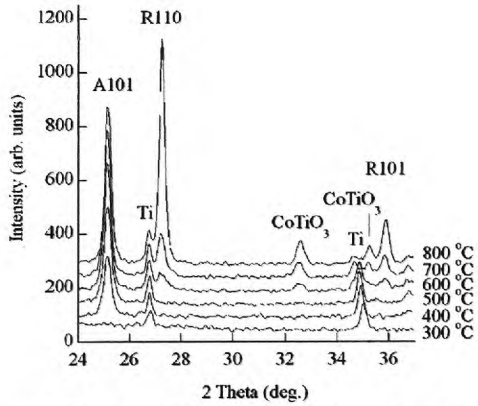


Figure 1. HTXRD pattern of $Ti_{0.95}Co_{0.05}O_2$ film deposited on a Ti substrate, annealed in situ from room temperature to 800 °C. "A" denotes anatase peak positions, and "R" denotes rutile.

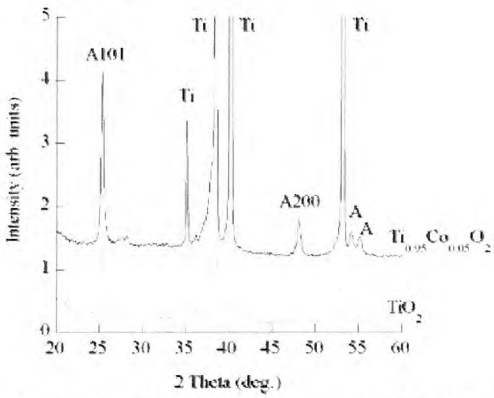


Figure 2. Comparison of the XRD patterns for un-doped and doped (x = 0.05) anatase films thermally treated at 400 °C for 1.5 h.

Figure 1 shows the high-temperature X-ray diffraction (HTXRD) pattern of a $Ti_{0.95}Co_{0.05}O_2$ film annealed from room temperature to 800 °C (under an Ar atmosphere to minimize substrate oxidation).

Only peaks attributed to the substrate (Ti) were observed at room temperature which confirms that the as-deposited film was amorphous. When the anneal temperature was increased to 400 °C, peaks corresponding to the anatase phase were observed indicating the crystallization and dehydration of the as-deposited structure (eq 4).

$$2Ti_{(1-y)}Co_yO_3{\cdot}(H_2O)x \rightarrow 2Ti_{(1-y)}Co_yO_2 + 2xH_2O + O_2 \quad (4)$$

Upon further increasing the temperature to 600 °C a transition to the rutile polymorph is observed with simultaneous ejection of $CoTiO_3$ from the lattice. Thus, careful control of the annealing temperature below 600 °C is required for maintained solubility of the Co in the host TiO_2 lattice; below 600 °C the formation of $CoTiO_3$ is completely suppressed. A comparison of the XRD patterns for both the doped and the un-doped anatase films are shown in Figure 2.

From these data the lattice parameters were calculated from a Le Bail extraction of the diffraction data using the GSAS suite of programs[15] (Table 1). The d-spacing increased for the doped films in agreement with predictions for a Co-doped anatase matrix. In particular the c-axis was found to increase markedly from 9.008(2) Å to 9.478(3) Å; these results are consistent with those in the literature for films formed using vacuum techniques.[6,16] In addition there is a clear shift of the diffraction peaks with temperature corresponding to the thermal expansion of the film.

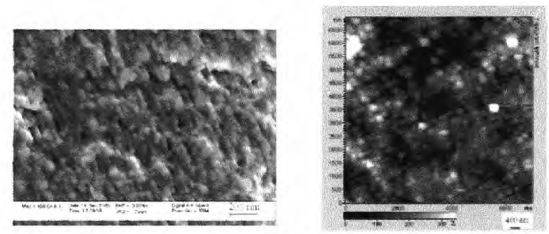


Figure 3. Film morphology for anatase $Ti_{0.95}Co_{0.05}O_2$. (left) FESEM image, (right) AFM image.

Table 1. Lattice Parameters from XRD Data for Un-Doped and Co-Doped Anatase Films Annealed at 400 °C

film	d spacing (Å)	lattice parameter (Å)
TiO_2	$d_{101} = 3.501$	$a = 3.7930(9)$
	$d_{200} = 1.888$	$c = 9.008(2)$
$Ti_{0.95}Co_{0.05}O_2$	$d_{101} = 3.505$	$a = 3.7853(8)$
	$d_{200} = 1.890$	$c = 9.468(3)$

Matsumoto et al.[6] reported that only the (004) and (008) peaks corresponding to anatase were observed, indicating a high degree of texture in their films. However, in the current work it is clear that the (101) and (200) peaks of the anatase phase are predominant, indicative of randomly oriented material, as was reported by Punnoose et al.[8] The reason for these differences may be due to different deposition methods, Co contents, or substrate effects.

The morphology of the annealed doped film is shown in Figure 3. Before thermal treatment, the film is amorphous and no crystallites were observed. After annealing at 400 °C for 1.5 h in air, spherical particles can be seen in the field emmision scanning electron microscopy (FESEM) image, Figure 3. The particle size distribution is relatively homogeneous and about 50 nm in diameter.

EDS analysis confirmed that Co is distributed throughout the film with only slight variations in the composition. On average, the Co:Ti ratio is 4%, and this agrees well with the nominal stoichiometry of 5% Co in the solution. According to Matsumoto et al.[6] the maximum solid solubility of Co in TiO_2 is 8%, and above this value $CoTiO_3$ forms. From the current work it is clear that at elevated temperatures (greater than 600 °C) the solubility of Co in TiO_2 is significantly decreased, as evidenced by the ex-solution of $CoTiO_3$. The absence of $CoTiO_3$ at low temperature is consistent with the level of Co suggested in this study and in previous literature reports.

The same grain shape of the doped film is shown more clearly in the atomic force microscopy (AFM) image, Figure 3. Using the XRD measurements the grain size was also calculated using the Scherrer equation (eq 5):

$$t = \frac{0.9\lambda}{B\cos\theta} \quad (5)$$

where t is particle size, λ is the wavelength of Cu Kα, and B is fwhm (full width at half-maximum) of the broadened diffraction line on the 2θ scale (radians). This calculation

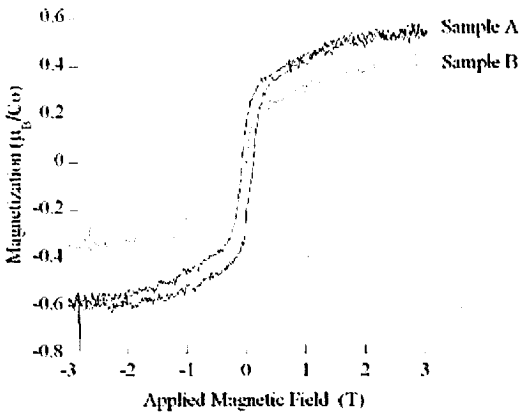


Figure 4. Room temperature in-plane magnetization vs magnetic field for two $Co_{0.05}Ti_{0.95}O_2$ samples (denoted A, B) produced under nominally identical experimental conditions.

gives a value of 50−100 nm, consistent with the FESEM and AFM data.

Finally, the magnetic character of the electrodeposited material is confirmed. Figure 4 shows room temperature in-plane magnetization versus magnetic field for two samples produced with nominally identical experimental conditions (denoted A and B). The difference of the two hysteresis loops may be due to the variation of the Co concentration in the films or due to variation in the volume of the deposited materials. The behavior is clearly ferromagnetic, and the signal is appropriate for a dilute ferromagnetic oxide thin film (0.35−0.6 μ_B/Co) and in agreement with Matsumoto et al.[6] Coupled with the XRD results, we suggest that in these films the magnetic behavior observed is related to Co cations substituted in the TiO_2 structure.

In summary, $Ti_{1-x}Co_xO_{2-\delta}$ films have been successfully prepared using a simple solution-based approach. The composition of the films is directly related to the solution concentration. When the annealing temperature is greater than 600 °C a $CoTiO_3$ impurity phase is formed along with the rutile polymorph. However, when controlling the annealing temperature below 600 °C only single phase anatase is observed, and the lattice parameter is consistent with site-substitution by Co cations. The films annealed at 400 °C show room-temperature ferromagnetic behavior as observed for films grown under vacuum conditions. This approach is an attractive method of producing ferromagnetic material with well-controlled stoichiometry and crystallization behavior.

Acknowledgment. The authors acknowledge the award of an ORS scholarship (H.W.). The assistance of Richard Sweeney in collecting the XRD data is gratefully acknowledged.

Supporting Information Available: Details of deposition conditions and film analyses (PDF). This material is available free of charge via the Internet at http://pubs.acs.org.

CM070928R

(15) Von Dreele, R. B.; Larson, A. C. *General Structural and Analytical System*; Los Alamos National Laboratory: Los Alamos, NM, U.S.A., 2006.

(16) Shinde, S. R.; Ogale, S. B.; Das Sarma, S.; Simpson, J. R.; Drew, H. D.; Lofland, S. E.; Lanci, C.; Buban, J. P.; Browning, N. D.; Kulkami, V. N.; Higgins, J.; Sharma, R. P.; Greene, R. L.; Venkatesan, T. *Phys. Rev. B* **2003**, *67* (11), 115211-1−115211-6.

8.0 Reference

1. Wiggins, M.D., Nelson M. C., Aita C. R. *Phase Development in Sputter Deposited Titanium Dioxide.* in *The 42nd national symposium of the American Vacuum Society.* 1996: AVS.

2. Diebold, U., *The surface science of titanium dioxide.* Surface Science Reports, 2003. **48**(5-8): p. 53-229.

3. Burns, G.P., Baldwin, I. S. , Hastings. M. P , Wilkes.J. G, *The Plasma Oxidation of Titanium Thin Films to Form Dielectric Layers.* Journal of Applied Physics, 1989. **66**(6): p. 2320-2324.

4. Shih, C.M., *Deposition and Application of Titanium Oxide by Liquid Phase Deposition*, in *Department of Electrical Engineering.* 2005, National Sun Yat-sen University: Taiwan. p. 162.

5. Dietl, T., Ohno, H., Matsukura, F., Cibert, J., Ferrand, D., *Zener Model Description of Ferromagnetism in Zinc-Blende Magnetic Semiconductors.* Science, 2000. **287**(5455): p. 1019-1022.

6. Matsumoto, Y.J., Murakami, M , Shono. T.J. , Hasegawa. T. , Fukumura. T. , Kawasaki. M. , Ahmet. P. , Chikyow. T. , Koshihara. S.Y. , Koinuma. H. , Koinuma. H, *Room-Temperature Ferromagnetism in Transparent Transition Metal-Doped Titanium Dioxide.* Science, 2001. **291**(5505): p. 854-856.

7. Chambers, S.A., Thevuthasan, S, R. Farrow. F. C. ,Marks. R. F. , Thiele.J.U. , Folks.L. , Samant. M. G. ,Kellock. A. J. , Ruzycki.N. , Ederer. D. L. ,Diebol. U., *Epitaxial Growth and Properties of Ferromagnetic Co-Doped TiO_2 Anatase.* Applied Physics Letters, 2001. **79**(21): p. 3467-3469.

8. Punnoose, A., Seehra, M. S, Park. W. K , Moodera. J. S. , *On the Room Temperature Ferromagnetism in Co-doped TiO_2 Films.* Journal of Applied Physics, 2003. **93**(10): p. 7867-7869.

9. Kim, J.Y., Park, J H, , Park. B. G. , Noh. H. J., Oh. S. J. , Yang. J. S. , Kim. D. H. , Bu. S. D. , Noh. T. W. , Lin. H. J., Hsien, H. H. , Chen, C. T., *Ferromagnetism Induced by Clustered Co in Co-Doped Anatase TiO_2 Thin Films.* Physical Review Letters, 2003. **90**(1): p. 017401-1.

10. Wan, K.Y., Ricardo, P., Ortega-Hertogs. J , Jagadeesh, S. , Punnoose, A. M. , Seehra, M.S. *Semiconducting and Ferromagnetic Behavior of Sputtered Co-doped TiO_2 Thin Films Above Room Temperature.* 2002: AIP.

11. Liu, L.F., Kang, J. F, Wang. Y , Tang. H. , Kong. L.G. , Zhang. X., Han. R.Q. , *The Role of Oxygen Vacancies in Magnetism of $Co_xTi_{1-x}O_{2-\alpha}$ Films on Si(001) Prepared by Sol-gel Method.* Solid State Communications, 2006. **139**(6): p. 263-267.

12. Manivannan, A., Seehra, M. S., Majumder. S.B. , Katiyar. R. S, *Magnetism of Co-doped Titania Thin Films Prepared by Spray Pyrolysis.* Applied Physics Letters, 2003. **83**(1): p. 111-113.

13. Zhitomirsky, I., Gal-Or, L., *Cathodic Electrosynthesis of Ceramic Deposits.* Journal of the European Ceramic Society, 1996. **16**(8): p. 819-824.

14. Zhou, Y.C., Phillips, R. J., Switzer, J. A., *Electrochemical Synthesis and Sintering of Nanocrystalline Cerium(IV) Oxide Powders.* 1995. p. 981-985.

15. Kondrachova, L., Hahn, B. P, Vijayaraghavan. G, Williams. R. D, Stevenson. K. J., *Cathodic Electrodeposition of Mixed Molybdenum Tungsten Oxides from Peroxo-polymolybdotungstate Solutions.* 2006. p. 10490-10498.

16. Liu, Y.L., Harrington, S, Yates. K. A, Wei. M, Blamire. M. G, MacManus-Driscoll. J. L, Liu. Y. C, *Epitaxial, Ferromagnetic $Cu_{2-x}Mn_xO$ Films on (001) Si by Near-Room-Temperature Electrodeposition.* 2005, AIP. p. 222108.

17. Zhitomirsky, I., *Cathodic Electrosynthesis of Titania Films and Powders.* Nanostructured Materials, 1997. **8**(4): p. 521-528.

18. Hench, L.L., West, J.k, *Principles of Electronic Ceramics.* 1989.

19. Buchana., R.C., *Ceramic Materials for Electronics Processing, Properties and Applications.* 1991. p. 131-137.

20. Taeyun, K., *Lead Zirconate Titanate (PZT) Based Thin Film Capacitors for Embedded Passive Applications*, in *Materials Science and Engineering.* 2003, North Carolina State University: Carolina. p. 231.

21. Callister, W.D.J., *Material Science and Engineering an Introduction.* Fifth Edition ed. 1999, New York: John Wiley & Sons, Inc. 871.

22. Brook, R.J., *Concise Encyclopedia of Advanced Materials.* 1991, Oxford: Pergamon.

23. http://www.azom.com/Details.asp?ArticleID=3593. Accessed 10/2006

24. Moulson, A.J., Herbert. J M,, *Electroceramics, Materials, Properties, Applications.* second ed. 2005, Sueesex: John Wiley & Sons Ltd. 557.

25. West , A.R., *Basic Solid State Chemistry*, ed. J.W.S. Ltd. 1996, England.

26. Lobl , P., Huppertz, M. , Mergel. D, Thin Solid Films, 1994. **251**: p. 72-79.

27. Miao, L., Ping, J. Kenji, K; Sakae, T. *Sputter Deposition of Polycrystalline and Epitaxial TiO_2 Films with Anatase and Rutile Structures.* in *Internation Conference on Electronic Materials*. 2002. Xi'an China.

28. Farrell, K.A., *Synthesis Effects on Grain Size and Phase Content in the Anatase-Rutile TiO_2 System*, in *Materials Science and Engineering*. 2001.

29. Ramamoorthy, M., . Vanderbilt, D; King-Smith, R. D.;, *First-principles Calculations of the Energetics of Stoichiometric TiO_2 Surfaces.* Physical Review B, 1994. **49**: p. 16721-16727.

30. http://ruby.colorado.edu/~smyth/min/tio2.html. Accessed 10/2006

31. Fujishima, A., Honda. K, *Electrochemical Photolysis of Water at a Semiconductor Electrode.* 1972. **238**(5358): p. 37-38.

32. Mills, A.A., *Water Purification by Semiconductor Photocatalysis.* Chemical Society Reviews, 1993. **22**(6): p. 417-425.

33. Pin-Ching, M., Sharon, S ,Daniel. B, M.,Huang, Z, Wolfrum, E J.,Jacoby, W. A., *Bactericidal Activity of Photocatalytic TiO_2 Reaction: toward an Understanding of Its Killing Mechanism.* Appl. Environ. Microbiol., 1999. **65**(9): p. 4094-4098.

34. Ferroni, M., Carotta, M. C., Guidi, V., Martinelli, G., Ronconi, F., Sacerdoti, M., Traversa, E., *Preparation and Aharacterization of Nanosized Titania Sensing Film.* Sensors and Actuators B: Chemical, 2001. 77(1-2): p. 163-166.

35. Dutta, P.K., Ginwalla, A., Hogg, B., Patton, B.R., Chwieroth, B., Liang, Z., Gouma, P., Mills, M., Akbar, S., *Interaction of Carbon Monoxide with Anatase Surfaces at High Temperatures: Optimization of a Carbon Monoxide Sensor.* J. Phys. Chem. B, 1999. **103**(21): p. 4412-4422.

36. Chen, J.C., *Removal of Acid Dye by TiO_2-Immobilized Granular Activated Carbon in a Liquid-Solid Fluidized Bed*, in *Department of Chemical Engineering*. 2004, Tatung University: Taiwan. p. 111.

37. Kertesz, Z., Szikszai, Z., Gontier, E., Moretto, P., Surleve-Bazeille, J.-E., Kiss, B., Juhasz, I., Hunyadi, J., Kiss, A.Z., *Nuclear microprobe Study of TiO_2-penetration in the Epidermis of Human Skin Xenografts.* Nuclear Microprobe Technology and Applications, 2005. **231**(1-4): p. 280-285.

38. Phillips, L.G., Barbano, D. M., *The Influence of Fat Substitutes Based on Protein and Titanium Dioxide on the Sensory Properties of Lowfat Milks.* J. Dairy Sci., 1997. **80**(11): p. 2726-2733.

39. Garfunkel, E., Gusev, A. V, *Fundamental Aspects of Ultrathin Dielectrics on Si-based Devices.* NANTO Science Series. 1998, Dordrecht: Kluwer Academic Publishers.

40. Bonhote, P., Gogniat, E, Gratzel, M, Ashrit, P. V., *Novel Electrochromic Devices Based on Complementary Nanocrystalline TiO_2 and WO_3 Thin Films.* Thin Solid Films, 1999. **350**(1-2): p. 269-275.

41. O'Regan, B., Gratzel, M, *A Low-Cost, High-Efficiency Solar Cell Based on Dye-Sensitized Colloidal TiO_2 Films.* Nature, 1991. **353**(6346): p. 737-740.

42. Dai, S.Y., Wang, K. J, *Optimum Nanoporous TiO_2 Film and Its Application to Dye-sensitized Solar Cells.* Chinese Physics Letters, 2003. **20**(6): p. 953-955.

43. Dumitriu, D., Bally, A.R, Balif.C, *Photocatalytic Degradation of Phenol by TiO_2 Thin Films Prepared by Sputtering.* Applied Catalysis. B, 2000. **25**: p. 83-92.

44. Meng, L., Andritschky, M, Dos Santos, M. P., *The Effect of Substrate Temperature on The Properties of Sputtered Titanium Oxide Films.* Applied Surface Science, 1993. **65-66**: p. 235-239.

45. Leprince-Wang, Y., Yu-Zhang, K, Nguyen Van, V, Souche, D, Rivory, J., *Correlation Between Microstructure and The Optical Properties of TiO_2 Thin Films Prepared on Different Substrates.* Thin Solid Films, 1997. **307**(1-2): p. 38-42.

46. Wohlfarth, E.P., *Ferro-Magnetic Materials.* Vol. 3. 1982, Amsterdam: North-Holland. 852.

47. Wolf, S.A., Awschalom, D. D., Buhrman, R. A., Daughton, J. M., von Molnar, S., Roukes, M. L., Chtchelkanova, A. Y., Treger, D. M., *Spintronics: A Spin-Based Electronics Vision for the Future.* Science, 2001. **294**(5546): p. 1488-1495.

48. Furdyna, J.K., *Diluted Magnetic Semiconductors.* Journal of Applied Physics, 1988. **64**(4): p. R29-R64.

49. Ohno, H., *Making Nonmagnetic Semiconductors Ferromagnetic.* Science, 1998. **281**(5379): p. 951-956.

50. Fukumura, T., Jin, Z. A , Ohtomo. A , Koinuma .H. , Kawasaki. M, *An Axide-diluted Magnetic Semiconductor: Mn-doped ZnO.* Applied Physics Letters, 1999. **75**(21): p. 3366-3368.

51. Fiederling, R., Keim, M., Reuscher, G., Ossau, W., Schmidt, G., Waag, A. ,Molenkamp, L. W., *Injection and Detection of a Spin-polarized Current in a Light-emitting Diode.* 1999. **402**(6763): p. 787-790.

52. Ohno, Y., Young, D. K., Beschoten, B., Matsukura, F., Ohno, H., Awschalom, D. D., *Electrical Spin Injection in a Ferromagnetic Semiconductor Heterostructure.* 1999. **402**(6763): p. 790-792.

53. Ohno, H., Chiba, D., Matsukura, F., Omiya, T., Abe, E., Dietl, T. Ohno, Y., Ohtani, K., *Electric-field Control of Ferromagnetism.* 2000. **408**(6815): p. 944-946.

54. Ohno, H., *Semiconductors: Enhanced: Toward Functional Spintronics.* Science, 2001. **291**(5505): p. 840-841.

55. Yang, Z.X., Liu, G, Wu. R.Q., *Distribution and Magnetization of Co Impurities in Anatase TiO_2.* Physical Review B (Condensed Matter and Materials Physics), 2003. **67**(6): p. 060402.

56. Ge, S.H., Wang, X. W , Kou. X . M , Zhou. X. Y , Xi. L , Zuo. Y. L , Yang. X. L, *Room-temperature Ferromagnetism in $Co_xTi_{(1-x)}O_2$ Powders Made by sol-gel Method: a NMR study.* Magnetics, IEEE Transactions on, 2005. **41**(10): p. 2721-2723.

57. Wang, Y., Y, *Hydrogenation Induced Transformation of Paramagnetism to Room-temperature Ferromagnetism in Co-doped TiO_2 Ceramics.* Journal of Electroceramics, 2006. **16**(Volume 16, Number 4 / July): p. 389-391.

58. Suryanaryanan, R., Naik,V.M, Kharel. P ,Talagala. P, Naik. R, *Ferromagnetism at 300 K in Spin-Coated Films of Co Doped Anatase and Tutile-TiO_2.* Solid State Communications, 2005. **133**: p. 439-443.

59. Stampe, P.A., Kennedy, R. J., Xin. Y, Parker. J. S., *Investigation of the Cobalt Distribution in TiO_2:Co Thin Films.* Journal of Applied Physics, 2002. **92**(12): p. 7114-7121.

60. Bryan, J.D., Heald, S.M., Chambers, S.A., Gamelin, D.R., *Strong Room-Temperature Ferromagnetism in Co^{2+}-Doped TiO_2 Made from Colloidal Nanocrystals.* J. Am. Chem. Soc., 2004. **126**(37): p. 11640-11647.

61. Chambers, S.A., Droubay, T., Wang. C. M., Lea. A. S. , Farrow. R. F. C., Folks. L. , Deline, V. ,Anders, S., *Clusters and Magnetism in Epitaxial Co-doped TiO_2 Anatase.* Applied Physics Letters, 2003. **82**(8): p. 1257-1259.

62. Errico, L.A., Renteria, M., Weissmann. M., *Theoretical Study of Magnetism in Transition-metal-doped TiO_2 and $TiO_{2-\beta}$.* Physical Review B (Condensed Matter and Materials Physics), 2005. **72**(18): p. 184425.

63. Chambers, S.A., Farrow, R. F. C., Maat, S., Toney, M. F., Folks, L., Catalano, J. G., Trainor, T. P., Brown, G. E., *Molecular Beam Epitaxial Growth and Properties of $CoFe_2O_4$ on MgO(0 0 1).* Journal of Magnetism and Magnetic Materials, 2002. **246**(1-2): p. 124-139.

64. Chambers, S.A., Heald, S. M., Droubay. T., *Local Co Structure in Epitaxial $Co_xTi_{1-x}O_{2-x}$ Anatase.* Physical Review B, 2003. **67**(10): p. 100401.

65. Han, G.C., Luo, P., Guo, Z.B., Nahar, Fiaz Un, Tay, M., Wu, Y.H., Wang, S.J., *Co-doped TiO_2 Epitaxial Thin Films Grown by Sputtering.* Thin Solid Films: Proceedings of The International Conference on Materials for Advanced Technologies (ICMAT 2005) Symposium D: Magnetic Nanomaterials and Devices - ICMAT 2005 Symposium H, 2006. **505**(1-2): p. 137-140.

66. Kong, L.G., Kang, J. F, Wang. Y , Sun. L, Liu, L. F, Liu. X. Y, Zhang. X, Han. R. Q, *Oxygen-Vacancies-Related Room-Temperature Ferromagnetism in Polycrystalline Bulk Co-Doped TiO_2.* 2006, ECS. p. G1-G3.

67. Janisch, R., Spaldin,N. A. , *Understanding Ferromagnetism in Co-doped TiO_2 Anatase from First Principles.* 2006, APS. p. 035201.

68. Ando, K., Saito, H. , Jin. Z W , Fukumura. T. , Kawasaki, M. , Matsumoto, Y. , Koinuma, H. *Magneto-optical Properties of ZnO-based Diluted Magnetic Semiconductors.* 2001: AIP.

69. Chambers, S.A., Droubay, T.C., Wang, C.M., Rosso, K.M., Heald, S.M., Schwartz, D.A., Kittilstved, K.R., Gamelin, D.R., *Ferromagnetism in Oxide Semiconductors.* Materials Today, 2006. **9**(11): p. 28-35.

70. Kimura, H., Fukumura, T. , Kawasaki. M. , Inaba. K., Hasegawa. T. , Koinuma. H., *Rutile-type Oxide-diluted Magnetic Semiconductor: Mn-doped SnO_2.* Applied Physics Letters, 2002. **80**(1): p. 94-96.

71. Prellier, W., Fouchet,A., Mercey,B., *Oxide-diluted Magnetic Semiconductors: a Review of the Experimental Status.* Journal of Physics: Condensed Matter, 2003. **15**(37): p. R1583-R1601.

72. Wyckoff, R.W.G., *Crystal Structures.* 2nd ed. 1986, New York: Wiley.

73. Kenji, U., Hitoshi, T., Tomoji. K, *Magnetic and Electric Properties of Transition-metal-doped ZnO Films.* Applied Physics Letters, 2001. **79**(7): p. 988-990.

74. Prellier, W., Fouchet, A. , Mercey, B. , Simon. C. , Raveau. B., *Laser Ablation of Co:ZnO Films Deposited From Zn and Co Metal Targets on*

(0001) Al_2O_3 Substrates. Applied Physics Letters, 2003. **82**(20): p. 3490-3492.

75. Kim, J.H., Kim, H., Kim, D, Ihm, Y. E, Choo, W. K, *Magnetoresistance in Laser-deposited $Zn_{1-x}Co_xO$ Thin Films.* Physica B: Condensed Matter, 2003. **327**(2-4): p. 304-306.

76. Kim, D.J., Hahn, S. H, Oh, S. H , Kim, E.J, *Influence of Calcination Temperature on Structural and Optical Properties of TiO_2 Thin Films Prepared by Sol-gel Dip Coating.* Materials Letters, 2002. **57**(2): p. 355-360.

77. Ahn, Y.U., Kim, E. J, Kim, H. T, Hahn, S. H, *Variation of Structural and Optical Properties of Sol-gel TiO_2 Thin Films with Catalyst Concentration and Calcination Temperature.* Materials Letters, 2003. **57**(30): p. 4660-4666.

78. Aarik, J., Aidla, A, Kiisler, A. A, Uustare, T, Sammelselg, V, *Effect of Crystal Structure on Optical Properties of TiO_2 Films Grown by Atomic Layer Deposition.* Thin Solid Films, 1997. **305**(1-2): p. 270-273.

79. Takeda, S., Suzuki, S, Odaka, H, Hosono, H, *Photocatalytic TiO_2 Thin Film Deposited onto Glass by DC Magnetron Sputtering.* Thin Solid Films, 2001. **392**(2): p. 338-344.

80. Li, S.D., Lu, L, Huang. Z. G, *Ferromagnetic CrSb Film Fabricated by Pulse-laser Deposition and Rapidly Annealing.* Journal of Magnetism and Magnetic Materials, 2007. **312**(2): p. 305-309.

81. Natarajan, C., Nogami, G., *Cathodic Electrodeposition of Nanocrystalline Titanium Dioxide Thin Films.* Journal of The Electrochemical Society, 1996. **143**(5): p. 1547-1550.

82. Aita, C.R., *Sputter Deposition of Ceramic Oxide and Nitride Films*, in *Intermetallic and Ceramic Coatings*, B.D. Narendra, Sudarshan, T.S., Editor. 1999, Marcel Dekker, INC: New York.

83. Thornton, J.A., Greene, J. E., *Sputter Deposition Processes*, in *Handbook of Deposition Technologies for Films and Coatings : Science, Technology, and Applications*, R.F. Bunshah, Editor. 1994, Noyes Publications. p. 835.

84. Kiyotaka, W., Shigeru, H, *Handbook of Sputter Deposition Technology: Principles, Technology and Applicatons.* 1992, NewYork: Noyes Publications.

85. Coburn, J.W., *Mass spectrometric studies of positive ions in r.f. glow discharges.* Thin Solid Films, 1989. **171**(1): p. 65-80.

86. Kohler, K., Coburn, J. W. , Horne, D. E. ,Kay, E , Keller, J. H., *Plasma Potentials of 13.56-MHz rf Argon Glow Discharges in a Planar System.* Journal of Applied Physics, 1985. **57**(1): p. 59-66.

87. Coburn, J.W., Eric, K., *Positive-ion Bombardment of Substrates in rf Diode Glow Discharge Sputtering.* Journal of Applied Physics, 1972. **43**(12): p. 4965-4971.

88. Tachibana, Y., Ohsaki, H, Hayashi. A, Mitsui. A, Hayashi. Y, *TiO_{2-X} Sputter for High Rate Deposition of TiO_2.* Vacuum, 2000. **59**(2-3): p. 836-843.

89. Francis, L.F., *Sol-Gel Methods for Oxide Coatings*, in *Intermetallic and Cearmic Coatings*, N.B.D.T.S. Sudarshan, Editor. 1999, Marcel Dekker, Inc: New York.

90. Livage, J., *Synthesis, Strucutre and Applications of TiO_2 Gels.* Materials Resources Society Symposium Procedings, 1986. **73**: p. 717-724.

91. Matsuda, A., A., *Preparation of B_2O_3-P_2O_5-SiO_2 Coating Films by The Sol-Gel Method.* Journal of Materials Science, 1992 August. **27**(15): p. 4189-4194.

92. Aegerter, M.A., *Ferroelectric thin coatings.* Journal of Non-Crystalline Solids, 1992. **151**(3): p. 195-202.

93. Zhitomirsky, I., *Electrolytic Deposition of Oxide Films in the Presence of Hydrogen Peroxide.* Journal of the European Ceramic Society, 1999. **19**(15): p. 2581-2587.

94. Zhitomirsky, I., Gal-Or, L. , Kohn, A., *Electrolytic PZT films.* Journal of Materials Science, 1997. **32**: p. 803-807.

95. Switzer, J.A., *Electrochemical Synthesis of Ceramic Films and Powders.* American Ceramic Society Bulletin, 1987. **66**: p. 1521-1524.

96. Breyfogle, B.E., et al., *Electrodeposition of Silver(II) Oxide Films.* Journal of The Electrochemical Society, 1996. **143**(9): p. 2741-2746.

97. Matsumoto, Y., Hombo, J, Qiong. C, *A New Ectrochemical Synthesis of Iron Spinel Oxide in LiOH.* Journal of Electroanalytical Chemistry, 1990. **279**(1-2): p. 331-336.

98. Switzer, J.A., Shane, M. J, Phillips. R. J., *Electrodeposited Ceramic Superlattices.* Science, 1990. **247**(4941): p. 444-446.

99. Zhou, Y.C.S., J. A., *Growth of Cerium(IV) Oxide Films by the Electrochemical Generation of Base Method.* Journal of Alloys and Compounds, 1996. **237**(1-2): p. 1-5.

100. Peulon, S., Lincot, D, *Mechanistic Study of Cathodic Electrodeposition of Zinc Oxide and Zinc Hydroxychloride Films from Oxygenated Aqueous Zinc Chloride Solutions.* 1998, ECS. p. 864-874.

101. Zhitomirsky, I., *Electrochemical Coatings*, in *Intermetallic and Ceramic Coatings*, N.B. Dahotre, Editor. 1999, Marcel Dekker,: New York. p. 100.

102. Breyfogle, B.E., Phillips, R. J, Switzer. J. A., *Epitaxial Electrodeposition of Silver Oxide Nitrate ($Ag(Ag_3O_4)_2NO_3$) onto Highly-Oriented Conducting Metal Oxides in the Lead-Thallium-Oxygen System.* 1992. p. 1356-1360.

103. Switzer, J.A., Shumsky, M. G, Bohannan. E. W., *Electrodeposited Ceramic Single Crystals.* Science, 1999. **284**(5412): p. 293-296.

104. Switzer, J.A., Kothari, H. M, ohannan.E. W., *Thermodynamic to Kinetic Transition in Epitaxial Electrodeposition.* 2002. p. 4027-4031.

105. Amblard, J., Epelboin, I., Froment. M, Maurin. G., *Inhibition and Nickel Electrocrystallization.* Journal of Applied Electrochemistry, 1979. **9**(2): p. 233-242.

106. Zhitomirsky, I., *Electrophoretic and Electrolytic Deposition of Ceramic Coatings on Carbon Fibers.* Journal of the European Ceramic Society, 1998. **18**(7): p. 849-856.

107. Zhitomirsky, I., *Ceramic films using cathodic electrodeposition.* JOM, 2000. **52(1)**: p. 1-11.

108. Pauporte, T., Goux, A., Kahn-Harari. A. , Tacconi. N. , Chenthanmarakshan. C.R., Rajeshwar. K., Lincot. D., *Cathodic Electrodeposition of Mixed Thin Films.* Journal of Physics and Chemistry of Solids, 2003. **64**: p. 1737-1742.

109. Helen, G.A.T., Kamath, P. V, *Electrochemical Synthesis of Metal Oxides and Hydroxides.* Chemistry Materials, 2000. **12**: p. 1195-1204.

110. Zhitomirsky, I., *Cathodic Electrodeposition of Ceramic and Organoceramic Materials. Fundamental Aspects.* Advances in Colloid and Interface Science, 2002. **97**(1-3): p. 277-315.

111. Zhitomirsky, I., Kohn, A., Gal-Or, L., *Cathodic Electrosynthesis of PZT Films.* Materials Letters, 1995. **25**(5-6): p. 223-227.

112. Verwey, E.J.W., Overbeek, J.T.G, *Theory of the Stability of Lyophobic Colloids*. 1948, New York: Elsevier.

113. Zhitomirsky, I., *New developments in electrolytic deposition of ceramic films.* Bull. Am. Ceram. Soc, 2000. **79**: p. 57.

114. Zhitomirsky, I., Gal-Or, L., Kohn, A., *Electrodeposition of Ceramic Films from Non-aqueous and Mixed Solutions.* Journal of Materials Science, 1995. **30**: p. 5307-5312.

115. Xiong, J., Chen, Y, Qiu. Y, Tao. B. W, Qin. W. F , Cui. X. M, Tang. J. L, Li. Y. R, *A Novel Process for CeO_2 Single Buffer Layer on Biaxially Textured Metal Substrates in YBCO Coated Conductors.* Superconductor Science and Technology, 2006. **19**(10): p. 1068-1072.

116. Boccaccini, A.R., Zhitomirsky, I., *Application of Electrophoretic and Electrolytic Deposition Techniques in Ceramics Processing.* Current Opinion in Solid State & Materials Science, 2002. **6**: p. 251-260.

117. Zhitomirsky, I., Gal-Or, L., *Ruthenium Oxide Deposites Prepared by Cathodic Electrosynthesis.* Materials Letters, 1997. **31**: p. 155-159.

118. Derjaguin, B.V., Landau, L.D., Acta Physicochim., 1941. **14**: p. 633.

119. www.teach.ustc.edu.cn/jpkc/xiaoji/wjhx/skja/chapter18.doc. Accessed 12/2006

120. Dann, S.E., *Reactions and Characterization of Solids*, ed. E.W. Abel. 2000, Cambridge UK: Polestar Wheatons Ltd.

121. Cullity, B.D., Stock, S. R., *Element of X-Ray Diffraction*, ed. J. M, Horton. 2001, London: Prentice Hall Upper Saddle River.

122. www.chm.bris.ac.uk/pt/diamond/stuthesis/Chapter2.htm, Accessed 11/2006.

123. Tanaka, K., *High Resolution Scanning Electron Microscopy of the Cell.* Biology of the Cell, 1989. **65**: p. 89-98.

124. Ebnesajjad, S., Khaladkar, P. R. , *Fluoropolymers Applications in Chemical Processing Industries*. 2005, New York, USA: William Andrew Inc. 665.

125. Russ, J.C., *Fundamentals of Energy Dispersive X-Ray Analysis*. 1987, Raleigh, USA: Butterworths& Co Ltd. 308.

126. Bonnell, D.A., *Scanning Probe Microscopy and Spectroscopy*. 2nd ed. 2001, Canada: Wiley-VCH. 493.

127. Gobel, O.F., *The Growth of Patterned Ceramic Thin Films From Ploymer Precursor Solutions.* 2004, University of Groningen, the Netherlands. p. 138.

128. Lucille.A. G; Fred, A.S., *Introduction to Focused Ion Beams-Instrumentation, Theory, Techniques and Practice.* 2004, New York USA: Springer. 357.

129. Maniguet, S., Mathew, J. R, Russell. E. A, *EXAFS of Carbon Monoxide Oxidation on Supported Pt Fuel Cell Electrocatalysts.* Journal of Physics and Chemistry B, 2000. **104**: p. 1998-2004.

130. http://www.srs.dl.ac.uk/xrs/, Accessed 10/2006.

131. Schwarzenbach, G., Muehlebach, J, Mueller. K, *Peroxo Complexes of Titanium.* 1970. p. 2381-2390.

132. Pourbaix, M., *Titanium*, in *Altas of Electrochemical Equilibria in Aqueous Solutions.* 1966, Pergamon Press: Oxford.

133. Shannon, R.D., Pask, J. A, *Kinetics of the Anatase-Rutile Transformation.* Journal of the American Ceramic Society, 1965. **48**(8): p. 391-398.

134. Hassan, A.K., Chaure, N B, Ray. A K, Nabok. A. V, Habesch. S, *Structural and Electrical Studies on Sol-gel Drived Spun TiO_2 Thin Films.* Journal of Physics D: Applied Physics, 2003. **36**: p. 1120-1125.

135. Kholmanov, I.N., Barborini, E., Vinati. S., Piseri. P.A Ducati. C., Lenardi. C., Milani. P., *The Influence of the Precursor Clusters on the Structural and Morphological Evolution of Nanostructured TiO_2 Under Thermal Annealing.* Nanotechnology, 2003. **14**(11): p. 1168-1173.

136. Christoph, L., Manfred, Peters, *Titanium and Titanium Alloys.* 2003, Germany: WILEY-VCH GmbH & Co.KGaA. 513.

137. Kofstad, P., Hauffe, K, Kjollesdal, *Investigation on the Oxidation Mechanism of Titanium.* Acta Chemica Scandinavica, 1958. **12**: p. 239-266.

138. Lopes-Gomes, J.E., Huntz, A. M, *Correlation Between the Oxidation Mechanism of Titanium Under a Pure Oxygen Atmosphere, Morphology of the Oxide Scale, and Diffusional Phenomena.* Oxidation of Metals, 1980. **14**(3): p. 249-261.

139. Kofstad, P., *High Temperature Corrosion.* 1988, London: Elsevier Applied Science. 558.

140. Othmer, K., *Encyclopedia of Chemical Technology.* Vol. 23. 1983, New York: Wiley. 108.

141. Park, S.H., Choi, C. H, Kim. K. B, Kim. S. H, *Influences of ZnO Buffer Layers on the Quality of ZnO Films Synthesized by the Metal-Organic Chemical Vapor Deposition Process.* Journal of Electronic Materials, 2003. **32**(11): p. 1148-1154.

142. Sung, S.L., Merrill, E. W., ***Effect of Heating Titanium Above the α, β -Transition Temperature on Surface Morphology.*** Journal of Materials Science Letters, 1990. **9**(12): p. 1367-1370.

143. Rosa, C.J., *Oxygen Diffusion in Alpha and Beta Titanium in the Temperature Range of 932^0 to 1142^0C.* Metallurgical Transactions, 1970. **1**: p. 2517.

144. Dring, K., Dashwood, R, Inman. D. , *Predominance Diagrams for Electrochemical Reduction of Titanium Oxides in Molten $CaCl_2$.* 2005, ECS. p. D184-D190.

145. Gueneau de Mussy, J.P., Langelaan, G, Decer. J, Delplancke. J. L., *TEM and X-ray Diffraction Investigation of the Structural Characteristics of the Microporous Oxide Film Formed on Polycrystalline Ti.* Scripta Materialia, 2003. **48**(1): p. 23-29.

146. Greenwood, N.N., Earnshaw, A, *Chemistry of the Element.* 1986, Oxford: Pergamon Press Ltd. 1542.

147. Kornilov, I.I., Glazova, V.V, Proc.Acad. Sci. USSR, Chem. Scand, 1963. **150**: p. 1-6.

148. Thompson, C.V., *Secondary Grain Growth in Thin Films of Semiconductors: Theoretical Aspects.* 1985, AIP. p. 763-772.

149. Wong, C.C., Smith. H. I , Thompson. C. V *Surface-Energy-Driven Secondary Grain Growth in Thin Au Films.* 1986, AIP. p. 335-337.

150. Grovenor, C.R.M., *Microelectronic Materials* 1989, Bristol: Hilger.

151. Ning, X.J., Chien, F. R. , Pirouz. P. , Yang. J. W. , Asif Khan. M., *Growth Defects in GaN Films on Sapphire: The Probable Origin of Threading Dislocations.* Journal of Materials Research, 1996. **11**(3): p. 580.

152. Lee, J.B., Lee, M. H, Park. C. K, Park. J. S, *Effects of Lattice Mismatches in ZnO/Substrate Structures on the Orientations of ZnO Films and Characteristics of SAW Devices.* Thin Solid Films, 2004. **447-448**: p. 296-301.

153. Cheng, Y.T., Meng, W. J, *Epitaxial Growth of Omega-Titanium on the (111) Surface of Alpha-Iron.* Physical Review Letters, 1996. **76**(21): p. 3999.

154. Guo, W.L., Wang , X. K, *Formation of the Rutile TiO_2 Under Ultrasonic Irradiation.* Journal of Materials Science, 2004. **39**(9): p. 3265-3266.

155. Banerjee, R., Ahuja, R, Fraser. H. L., *Dimensionally Induced Structural transformations in Titanium-Aluminum Multilayers.* Physical Review Letters, 1996. **76**(20): p. 3778.

156. Kun, L.L., Lin, C.C, *Microstructural Evolution and Formation Mechanism of the Interface Between Titanium and Zirconia Annealed at 1550°C.* Journal of the American Ceramic Society, 2006. **89**(4): p. 1400.

157. Ting, C.C., Chen, S.Y, Liu, D. M, *Preferential Growth of Thin Rutile TiO_2 Films Upon Thermal Oxidation of Sputtered Ti Films.* Thin Solid Films, 2002. **402**(1-2): p. 290-295.

158. Malinov, S., Sha,W., Voon,C. S., *In situ High Temperature Microscopy Study of the Surface Oxidation and Phase Transformations in Titanium Alloys.* Journal of Microscopy, 2002. **207**(3): p. 163-168.

159. Zhang, F., Liu, X. H., *Effect of O_2 Pressure on The Preferred Orientation of TiO_2 Films Prepared by Filtered Arc Deposition.* Thin Solid Films, 1998. **326**(1-2): p. 171-174.

160. Zhang, F., Zheng, Z. H, Chen. Y, Liu. D, Liu. X. H, *Study on the Effect of Ion Beam Bombardment During Deposition on Preferred Orientation in Rutile-type Titanium Dioxide Films.* Journal of Applied Physics, 1998. **83**(8): p. 4101-4105.

161. Y.J. Matsumoto, M., Murakami, T.J. Shono, T. Hasegawa, T. Fukumura, M. Kawasaki, P. Ahmet, T. Chikyow, S.Y. Koshihara, H. Koinuma, H. Koinuma,, *Room-Temperature Ferromagnetism in Transparent Transition Metal-Doped Titanium Dioxide.* Science, 2001. **291**(5505): p. 854-856.

162. Reidy, D.J., Holmes, J.D, Morris. M.A. , *The Critical Size Mechanism for the Anatase to Rutile Transformation in TiO_2 and Doped-TiO_2.* Journal of the European Ceramic Society, 2006. **26**(9): p. 1527-1534.

163. Shinde, S.R., Ogale, S. B, Das Sarma.S , Simpson. J. R , Drew. H. D, Lofland. S. E , Lanci. C, Buban. J. P , Browning. N. D , Kulkarni. V. N., Higgins. J, Sharma. R. P, Greene. R. L. , Venkatesan. T, *Ferromagnetism in Laser Deposited Anatase $Ti_{1-x}Co_xO_{2-\alpha}$ Films.* Physical Review B (Condensed Matter and Materials Physics), 2003. **67**(11): p. 115211.

164. http://abulafia.mt.ic.ac.uk/shannon/ptable.php. accessed 10/2006

165. Bolton, W., *Electrical and Magnetic Properties of Materials.* 1992, London: Longman Scientific & Technical. 238.

166. Vogt, T., Woodward, P. M, Karen. P, Hunter. B. A, Henning. P, Moodenbaugh. A. R, *Low to High Spin-State Transition Induced by Charge Ordering in Antiferromagnetic $YBaCo_2O_5$.* Physical Review Letters, 2000. **84**(13): p. 2969 LP - 2972.

167. Kwon, S.K., Park, J. H, Min. B. I, *Charge and Orbital Ordering and Spin-state Transition Driven by Structural Distortion in $YBaCo_2O_5$.* Physical Review B, 2000. **62**(22): p. R14637 LP - R14640.

168. Respaud, M., Carlos, F,Luis. G.A ,Miguel Angel G. A , Bertrand. R,Jean Marc. B ,Harison. R ,Michel. G , Anna. L ,Juan. R.C. , *Magnetic and Magnetotransport Properties of $GdBaCo_2O_{(5+\delta)}$: A High Magnetic-field Study.* Physical Review B, 2001. **64**(21): p. 214401.

169. Khalyavin, D.D., Barilo, S. N , Shiryaev. S. V , Bychkov. G. L ,Troyanchuk. I. O , Furrer. A, Allenspach. P, Szymczak S. R, *Anisotropic Magnetic, Magnetoresistance, and Electrotransport Properties of $GdBaCo_2O_{5.5}$ Single Crystals.* Physical Review B Condensed Matter and Materials Physics, 2003. **67**(21): p. 214421.

170. Gouma, P.I., Michael, J. M, ,Sandhage. K. H, *Fabrication of Free-Standing Titania-based Gas Sensors by the Oxidation of Metal Titanium Foils.* Journal of the American Ceramic Society, 2000. **83**(4): p. 1007-1009.

171. Pang, X., Zhitomirsky, I, Niewczas. M, *Cathodic Electrolytic Deposition of Zirconia Films.* Surface and Coatings Technology, 2005. **195**(2-3): p. 138-146.